CHARLES UNIVERSITY

Faculty of Science

Department of Physiology of Animals

Mitochondrial uncoupling and mitochondrial morphology in relation to type-2 diabetes

DOCTORAL THESIS

Prague 2010   Ing. **Tomáš Špaček**

This thesis was elaborated in laboratory of the Membrane Transport Biophysics, Institute of Physiology, Academy of Sciences of the Czech Republic v.v.i.

PhD studies proceeded since September 2002 in PhD study program Physiology of Animals at Faculty of Sciences at Charles University in Prague.

Author: Ing. Tomáš Špaček

Supervisor: RNDr. Petr Ježek, DrSc.

Institute of Physiology ASCR

Prague, May 2010   ....

                                             Tomáš Špaček

ACKNOWLEDGMENTS

LIST OF AUTHOR'S PUBLICATIONS

Dlaskova A, Spacek T, Santorova J, Plecita-Hlavata L, Berkova Z, Saudek F, Lessard M, Bewersdorf J, Jezek P: 4Pi microscopy reveals an impaired three-dimensional mitochondrial network of pancreatic islet beta-cells, an experimental model of type-2 diabetes. *Biochim Biophys Acta.* (2010) *in press* **IF = 3.835** (2007)

Spacek T, Santorova J, Zacharovova K, Berkova Z, Hlavata L, Saudek F, Jezek P: Glucose-stimulated insulin secretion of insulinoma INS-1E cells is associated with elevation of both respiration and mitochondrial membrane potential. *Int J Biochem Cell Biol.* 40(8):1522-35 (2008) **IF = 4.009** (2007)

Raju N, Spacek T, Jezek J, Caminiti IM, Leinisch F, Hideg K, Jezek P, Trommer WE: Fatty acid binding site of mitochondrial uncoupling protein UCP2 as probed by EPR spectroscopy of spin-labeled fatty acids. *Appl. Magn. Reson.* 30, 373–83 (2006) **IF = 0.692** (2006)

Jezek P, Spacek T, Garlid K, Jaburek M: Undecanesulfonate does not allosterically activate H+ uniport mediated by uncoupling protein-1 in brown adipose tissue mitochondria. *Int J Biochem Cell Biol.* 38(11):1965-74 (2006) IF = **4.804** (2006)

Dlaskova A, Spacek T, Skobisova E, Santorova J, Jezek P: Certain aspects of uncoupling due to mitochondrial uncoupling proteins in vitro and in vivo. *Biochim Biophys Acta.* 1757(5-6):467-73 (2006) **IF = 4.237** (2006)

Zacharovova K, Berkova Z, Spacek T, Kriz J, Dovolilova E, Girman P, Koblas T, Jezek P, Saudek F: In vitro assessment of pancreatic islet vitality by oxymetry. *Transplant Proc.* 37(8):3454-6 (2005) **IF = 0.511** (2005)

Ruzicka M, Skobisova E, Dlaskova A, Santorova J, Smolkova K, Spacek T, Zackova M, Modriansky M, Jezek P: Recruitment of mitochondrial uncoupling protein UCP2 after lipopolysaccharide induction. *Int J Biochem Cell Biol.* 37(4):809-21 (2005) **IF = 3.578** (2005)

LIST OF ABBREVIATIONS

4-PSL-FA	4-PROXYL-palmitic acid
5-DSL-FA	5-DOXYL-stearic acid
AA	arachidonic acid
ADP	adenosine-5'-diphosphate
AMP	adenosine-5'-monophosphate
ATP	adenosine-5'-triphosphate
BAT	brown adipose tissue
BLM	black lipid membrane
BSA	bovine serum albumin
$C_{11}SO_3^-$	undecanesulfonate
$C_{12}E_9$	nonaethylene glycol monodecyl ether
cAMP	3'-5'-cyclic adenosine monophosphate
CAT	carboxyatractyloside
CCCP	carbonyl cyanide trifluoromethoxyphenylhydrazone
DOXYL-	4,4-dimethyl-oxazolidine-N-oxyl-
DTT	1,4-dithiothreitol
EDTA	ethylenediaminetetraacetic acid
EPR/ ESR	electron paramagnetic/spin resonance
ETA	all-*cis*-8,11,14-eicosatrienoic acid
FAs	fatty acids
FCCP	carbonyl cyanide p-(trifluoromethoxy)phenylhydrazone
FCS	fetal calf serum
FFAs	free fatty acids
GDP	guanosine-5'-diphosphate
GFP	green fluorescent protein
GK	Goto Kakizaki rats
GLUTx	glucose transporter isoforms
GMP	guanosine-5'-monophosphate
GPx	glutathion peroxidase
GSH	reduced glutathion
GSIS	glucose-stimulated insulin secretion
GSSG	oxidized glutathion

GTP	guanosine-5'-triphosphate
HAEC	human aortic endothelial cell
HFD	high fat diet
HNE	4-hydroxynonenal
IGT	impaired glucose tolerance
ILx	any interleukin isoform
IMM	inner mitochondrial membrane
JNK	c-Jun N-terminal kinase
KO	gene knockout
LPS	lipopolysaccharide
MAPK	mitogen-activated protein kinases
MCP1	monocyte chemoattractant protein-1
MOPS	morpholinopropanesulfonic acid
NA	numeric aperture
NO	nitrogen monoxide
OGTT	oral glucose tolerance test
(F)PALM	(fluorescence) photoactivation localization microscopy
PMSF	phenylmethanesulfonyl fluoride
PN	purine nucleotide
PROXYL-	2,2,5,5-tetramethyl-1-pyrrolidin-N-oxyl-
PUFAs	polyunsaturated fatty acids
PUMPn	plant uncoupling mitochondrial protein, any isoform
ROS	reactive oxygen species
SIM	sucrose isolation medium
SLS	N-Lauroylsarcosine sodium salt
SNAP	synaptosome-associated protein
SNARE	soluble N-ethylmalemide-sensitive factor attachment protein receptor
SOD	superoxide dismutase
SPQ	6-methoxy-N-(3-sulfopropyl)quinolinium
SRE	sterol regulatory element
SREBP1	sterol regulatory element binding protein-1
STED	stimulated emission depletion microscopy
STORM	stochastic optical reconstruction microscopy
T2DM	type-2 diabetes mellitus
TE	Tris-EDTA buffer
TES	N-tris(hydroxymethyl)methyl-2-aminoethanesulfonic acid

TNF	tumor necrosis factor
UCP1	BAT-specific mitochondrial uncoupling protein 1 (thermogenin)
UCPs,UCPn	uncoupling proteins, any uncoupling protein isoform
VAMP	vesicle-associated membrane protein
WT	wildtype animal
ZDF	Zucker diabetic fatty rats

CONTENTS

1 INTRODUCTION

Mitochondria are subcellular organelles essential for eukaryotic aerobic metabolism, involving citric acid and β-oxidation metabolic pathways, and respiratory chain followed by adenosine triphosphate (ATP) synthesis during oxidative phosphorylation. The role of mitochondria in apoptosis, homeostasis of reactive oxygen species (ROS) and calcium is also very important. Mitochondria participate in cell signal transduction, glucose sensing in pancreatic β-cells, aging, and regulation of body weight. Mitochondria thus play a central role in molecular physiology of the cell and therefore it is not surprising that their pathophysiology is combined with numerous diseases (diabetes mellitus II, atherosclerosis, hypertension, cancer, neurodegenerative diseases and other).

Mitochondria of eukaryotic cells form a reticular network in most cell types. Energetic status of mitochondria, the rate of oxidative phosphorylation, is expressed not only by bioenergetic parameters measurable by classical biophysical methods (*e.g.* respiration and mitochondrial membrane potential) but it is also reflected in morphology of the mitochondrial network. The overall mitochondrial reticulum shape is controlled by the balance between fusion and fission events because both the processes participate in apoptosis in their extremes. Taken together, abnormalities from the regular shape of the mitochondrial network could point to different pathological states.

Mitochondrial uncoupling proteins (UCPs) form a distinct subfamily within the gene family of mitochondrial anion carriers. Likewise chemical uncouplers, UCPs uncouple respiration from ATP synthesis by their protonophoric activity. Nevertheless, only UCP1 isoform in brown adipose tissue (BAT) is present in such a high amount that it can cause nearly complete uncoupling and concomitant heat production. The molecular mechanism of UCP1-catalyzed H^+ transport remains still controversial. Currently, two mechanisms are accepted: *i)* the fatty acid cycling model and *ii)* the proton buffering model. Both hypotheses continue to be matter of debate and arguments have been made for and against both models.

In the case of UCP2 isoform, the situation is even more complicated. More than decade of studies did not answer the question of its function in mitochondria, thus the controversy of uncoupling mechanism is accompanied by the explanation of its physiological role. A concept of a "mild uncoupling" amounting only several mV changes has been developed. The physiological function of such a mild uncoupling might be in suppression of mitochondrial ROS. Among other physiologically acceptable roles of UCP2, regulation of glucose-stimulated insulin

secretion (GSIS) and regulation of mitochondrial Ca^{2+} have been proposed. UCP2 became therefore a candidate gene for diabetes mellitus type-2 treatment.

The aims of the thesis were:

1. verify the fatty acid cycling model of protonophoric activation of UCP1
2. determine if UCP2 binds fatty acids
3. bioenergetic characterization of INS-1E cells (β-cell model)
4. compare the mitochondrial network morphology of diabetic and normal β-cell

2 BACKGROUND

2.1 Mitochondrial uncoupling proteins

Uncoupling proteins (UCPs) form a separate branch within a gene superfamily of mitochondrial anion carriers, containing 46 members in mammals, termed SLC25 [3-5]. The *UCP*s subfamily contains several different proteins expressed in various tissues of numerous organisms. There are currently five known isoforms of these genes in the human genome: *UCP1-5*, all of which are found in mammals, some of which are found in vertebrates and invertebrates [6]. Three other isoforms originally termed plant uncoupling mitochondrial proteins (*PUMP*n) exist in plants [7]. The phylogenetically oldest seems to be the *UCP4* isoform, the orthologues of which exist in *Dictyostelium discoideum* and *Caenorhabditis elegans* [3]. The carrier most sequentially similar to *UCP*s is the oxoglutarate carrier, which, however, lacks the unique uncoupling protein signature sequences [3, 4, 8, 9]. All isoforms of UCPs reside in the inner mitochondrial membrane (IMM).

2.2 Uncoupling protein 1 – distribution, structure and function

Classic UCP1, also known as thermogenin, was discovered in the mid- 70s of the last century [10]. Mammalian-specific brown adipose tissue (BAT), which is a specialized tissue responsible for cold-induced non-shivering thermogenesis, is the tissue where UCP1 is expressed in a huge amount - UCP1 content can cover up to 10-15% of the inner membrane proteins (up to 5% of mitochondrial proteins in total) [11]. Contrary to white fat, the highly innervated and vascularized BAT contains multilocular adipocytes (multivesicular discrete fat droplets per cell) with a high content of tightly packed mitochondria. Thermogenic function of BAT is achieved by rapid oxidation of fatty acids (FAs) and simultaneous uncoupling mediated by UCP1 which leads to heat production [1, 12-16]. The induction of the thermogenic response by cold exposure [17, 18] and/or a high fat diet [19, 20] is referred to as adaptive thermogenesis, cold-induced and diet-induced, respectively. Hypothalamic centers respond to a cold environment by propagating the signals through the sympathetic nervous system, resulting in the release of norepinephrine from the nerve terminals innervating BAT. Norepinephrine binds to β_3-adrenergic receptors located in cell membrane of brown fat cell. Adrenergic stimulation leads to cyclic adenosine monophosphate (cAMP)-dependent lipolysis and free fatty acid

liberation, thus mobilizing substrates for activated brown fat thermogenesis [21-24] – see Figure 1. Also increased brown adipocyte cell differentiation (mitochondriogenesis and concomitant UCP1 synthesis) and proliferation upon cold acclimation or excessive caloric intake is under noradrenergic control [25, 26].
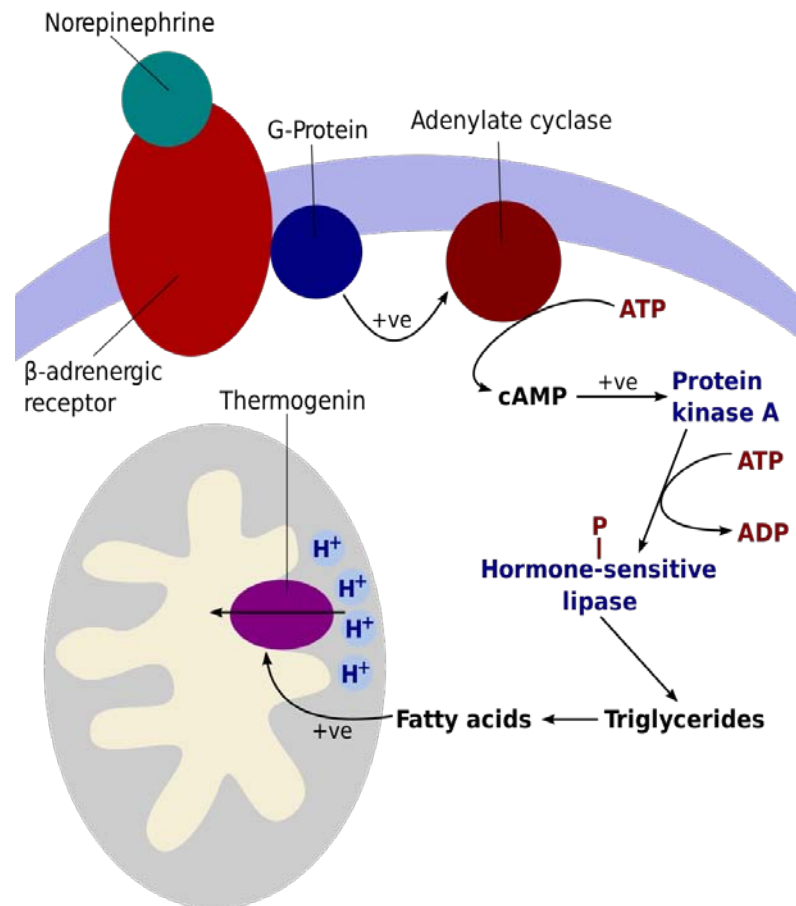
Figure 1 Mechanism of UCP1 activation in brown adipose tissue
(adopted from http://en.wikipedia.org/wiki/Thermogenin)

This muscle-independent phenomenon of nonshivering thermogenesis plays an important role in regulating body temperature during cold acclimation, arousal from hibernation or in newborn mammals and neonates. BAT therefore differentiates during fetal life of most mammals. In humans, BAT is mainly abundant in the axillary, cervical, and perirenal region of human fetus during the third trimester of gestation, but similarly to larger mammals is replaced by unilocular white adipose tissue with increasing age [27]. For the whole life-span, BAT principally persists only in small mammals including rodents. The tissue is localized in

interscapular, thoracic, cervical, axillary, perirenal, and inguinal areas so that the generated heat warms instantly the blood supply to vital organs. Moreover, approximately 60 % of blood flow is passing through BAT which enables it to act as a central heating system of the given organism [28].

Although UCP1 was originally ascribed exclusively to brown adipose tissue, it has been reported recently in thymocytes [29-31], thymus [29, 32, 33], skin [34], brain [35] and pancreatic β-cells [36]. UCP1 is also expressed in adult human subjects under pathological conditions (*e.g.* pheochromocytoma - norepinephrine-secreting tumors) [37].

Native UCP1 is thought to form transmembrane homodimers comprised of 33 kDa subunits with one purine nucleotide binding site [38]. Primary and probable secondary structure of UCP1 monomer is depicted on Figure 2. It is obvious that the monomer is composed of three homologous domains of around 100 residues, each of which contains two transmembrane-spanning α-helices and a long hydrophilic loop. Both, the C- and N-ends are located on the cytosolic side of the IMM, resulting in four cytosolic and three matrix segments [39-41].
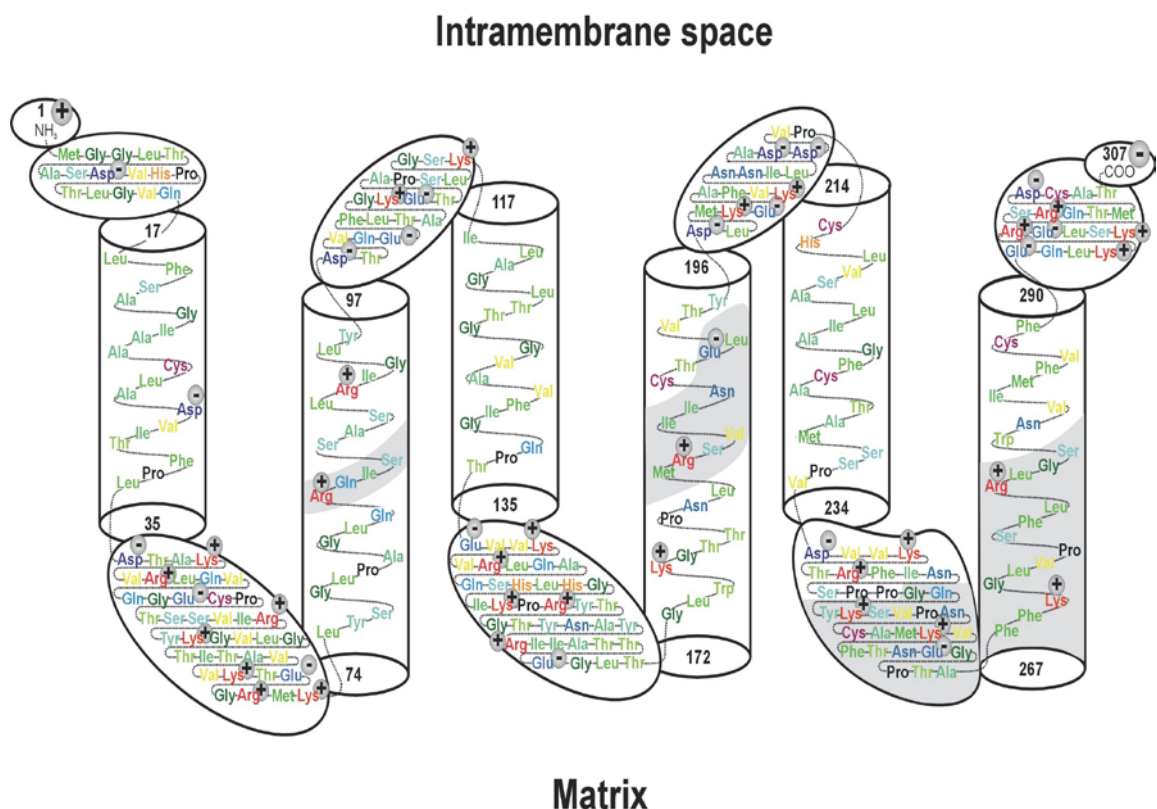
Figure 2 Model of primary structure and transmembrane folding of mammalian (rat) UCP1.

Six short transmembrane α-helices is bound together with long hydrophilic matrix- and intramembrane space loops. The shadowed areas are the loci interacting with purine nucleotide di- and triphosphates (adopted from [2])

UCP1 has wide anion substrate specificity. UCP1 transports monovalent unipolar anions [42-44], including halide anions such as chloride. This makes BAT mitochondria uniquely permeable to chloride at neutral pH. Also other small anions such as hypophosphate and physiologically relevant anions such as pyruvate and other ketocarboxylates are translocated in a uniport mode by UCP1.

UCP1 in brown adipocytes is responsible for specific dissipation of protonmotive force created by respiratory chain complexes into heat by allowing the re-entry of protons translocated by proton pumps of the complexes I, III and IV. The phenomenon is called "uncoupling of oxidative phosphorylation". Note that the role of UCP1 in the catalysis of heat production is simply to provide a short-circuiting backflow pathway for protons. Energy corresponding to the protonmotive force is in a simplified sense of the first law of thermodynamics transferred as heat instead of doing useful work (ATP synthesis).

2.2.1 *Controversy about activation of protonophoretic activity of UCP1*

The mechanism, by which UCP1 exerts its protonophoretic activity, is still to be determined. Free fatty acids released from the triglycerides are considered as physiological activators of UCP1 function *in vivo*. However, there remains considerable controversy about the molecular mechanism of this activation. Three models have been suggested:

- *i)* fatty acid cycling model [45, 46]
- *ii)* proton buffering model [47] and
- *iii)* fatty acid independent proton pathway [48, 49]

For the fatty acid cycling model (Figure 3), it is assumed that UCP1 translocates the anionic forms of FAs from matrix side of the membrane to the intermembrane space, which is driven by electric potential generated by electron transport chain. In the absence of a carrier, charged fatty-acid anions inside the matrix would not be able to cross the IMM. After protonation in the intermembrane space, FA returns in a protonated form by flip-flop mechanism, hence carrying and subsequently releasing proton. Simply, the FA anions are considered as true anionic transport substrates of UCP1, similarly as numerous other unipolar monovalent anions which are conducted by UCP1, of course, usually without cycling, since they cannot return back in a protonated form. Among these anions, FAs have the highest affinity, so they compete with the other conducted anions. In general, higher hydrophobicity, or alkylchain length provides an anion with a higher affinity to UCP1 [42]. Note, that such a mechanism would act until all cycling substrates are removed from the membrane either by metabolism or being bound to sites with higher affinities, if exist [1].

Evidences supporting the fatty acid cycling model are derived from the experiments in which UCP1 was shown to transport alkylsulfonates ranging in alkyl chain length between C11 and C16. These molecules are considered as analogues of fatty acids which cannot be protonated at physiological pH and therefore exist only as an anionic form [42]. Therefore, undecanesulfonate ($C_{11}SO_3^-$) strongly competitively inhibits fatty acid anion uniport mediated by UCP1, while Cl^- can only slightly competitively inhibit FA uniport. On the contrary, both undecansulfonate as well as FAs inhibit Cl^- uniport mediated by UCP1 [46, 50].

The FA cycling model has also been supported by numerous reconstitution studies in liposomes [51, 52] and black lipid membranes (BLM) [53-55].
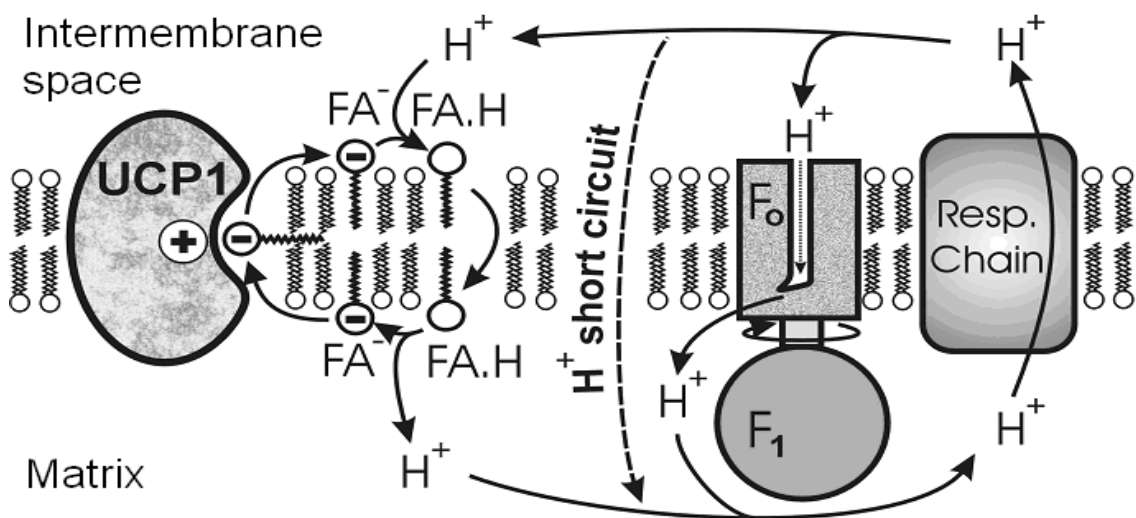
Figure 3 Fatty acid cycling model.

Fatty acid anion is transfered by UCP1 from the mitochondrial matrix across the inner membrane to the intermembrane space, protonated there, and flipping back in the protonated form.
FA – fatty acid, FA⁻ - fatty acid anion, F_OF_1 – subunits of ATP-ase (adopted from [1])

The opposing models to FA cycling hypothesized the existence of incomplete *ii)* or a pure iii) proton-pathway. According to local buffering model *ii)*, intermembrane fatty-acids insert their head groups into the proton transport pathway and provide buffering sites to assist proton translocation via UCP1 [56, 57]. Except of inserted fatty acids, proton transport pathway is formed by histidines and arginines resident in UCP1 structure. The proton-buffering model is supported by the fact that fatty acid activation of UCP1 function is pH-dependent. There is a sharp pH increase across the IMM over the range 7.0-8.0 [58]. The pH dependency may be an indication of the involvement of an amino acid side chain of UCP1 which was proposed in proton buffering model. Also mutagenesis experiments showed amino acids His145, His147 and

Asp27 to be necessary for fatty acids dependent H^+ transport [2].

The third model assumes completely pre-formed pathway for H^+, where fatty acids may or may not serve as mere accelerators of such a pathway [59, 60]. The major distinction of this model from the previous models is that it assumes uncoupling even in the absence of fatty acids.

The only issue, on which all three models agree, is the inhibition by purine nucleotide (PN) di- and triphophosphates. Ježek and colleagues [61] have confirmed inhibitory ability of guanosine- and adenosine monophosphate (GMP and AMP) as well as decrease in guanosine diphosphate (GDP) inhibitory ability when pH is elevated from neutral pH 7 to alkaline (the IC_{50} was by one order of magnitude higher when pH raises by one unit) and when Mg^{2+} is present. Excellent binding studies of Klingenberg and colleagues [62-65] then revealed the existence of a tight binding and loose binding conformation and other details of nucleotide interaction with UCP1. Moreover, these studies confirmed reduction in PN binding in the presence of inorganic anions such as sulfate, pyrophosphate etc.

Most of the studies, however, have demonstrated independent nature of inhibition by PN and activation by FAs, by the other words a non-competitive nature of PN inhibition with regards to FA uniport (*Model i*) [50] or FA-induced activation of uncoupling (*Model ii*) [47, 66]. Electron paramagnetic resonance (EPR) studies have identified an intermediate immobilization of spin-labeled FAs upon ATP binding to UCP1 contrary to a high immobilization on UCP1 in the absence of PN or no immobilization in the presence of alkylsulfonates or FAs as competing species in the FA-binding site [67]. This cannot be interpreted as that ATP and FAs act at the single site.

However, due to the existence of PN inhibition, one must either assume that the content of intramembrane cytosolic solution is such that it allows uncoupling at the thermogenic state in BAT and nearly no uncoupling in the resting state; or one must predict an activator which counteracts PN inhibition if it persists. *In vivo* nucleotide concentrations were estimated by LaNoue and colleagues as 0.5 mM ATP and 2 mM ATP in the thermogenic and resting state, respectively [68]. Ježek *et al.* have shown that just with Mg^{2+} present these concentrations provide an open and closed state of UCP1 [61]. Cannon *et al.* proposed palmitoyl-CoA as a possible physiological antagonist to the nucleotide binding to BAT mitochondria [69].

Currently, the first two mechanisms are generally accepted. Both hypotheses continue to be matter of debate and arguments have been made for and against both models.

Studies on UCP1 are believed to have practical applications to the problem of obesity, a consequence of energy imbalance. Energy wastage might be inducible by therapeutic intervention for the treatment of obesity [70]. It is known that many types of obesity in animal models are associated with a defective BAT function [71].

Human nuclear gene *UCP1* spans 13 kb of chromosome 4 and contains six exons. The promoter region has a TATA box and sequence resembling a cAMP response element [72, 73]. The following other *UCP* isoforms were identified by sequence similarity with *UCP1*.

2.3   Other *UCP* isoforms

In the last decade, isoforms *UCP2*, which exhibits the widest expression pattern among all isoforms in mammals, *UCP3*, expressed typically in skeletal muscle [74, 75], and *UCP4* and *-5*, expressed typically in the brain [76, 77] were discovered.

UCP4 and -5 share only 40% amino acid identity with UCP1. On the other hand, human UCP2 and -3 are both more similar to UCP1. The identity of amino acid sequence between human UCP2 and UCP3 is 71% and the identity with UCP1 is 59% and 57%, respectively [8]. The genomic structures of human *UCP2* and *UCP3* were found to be similar to each other and to *UCP1*. All three genes have relatively few exons – six to eight – and the coding sequence is confined to six exons in all of these. The first two exons of *UCP2* are not translated. In *UCP3*, there is at least one untranslated exon and multiple transcription initiation sites. Concerning the chromosomal localization of *UCP2* and *-3* genes on the human genome, both are present on chromosome 11q13 with the transcription initiation of *UCP2* placed only 7-8 kb downstream of the *UCP3* stop codon. This close arrangement has been interpreted as being the result of a duplication event [6, 78].

Classical mitochondrial experiments as well as reconstitution studies suggest that all UCP isoforms are able to mediate proton translocation across the lipid bilayer. The physiological role of UCP2-5 in non-thermogenic tissues lies hypothetically in their ability to partially uncouple mitochondria in the presence of fatty acids and thus slightly enhance the respiration rate and the concomitant metabolic rate. Only the UCP1 isoform in BAT is present in such a high amount that it can cause nearly complete uncoupling and concomitant heat production. However, not only high content of UCP1 in BAT is required for manifestation of the thermogenic function. Also all stechiometry of the respiratory chain together with low content of the ATP synthase and other conditions must play in accord to produce heat. This was shown in the experiment, where UCP1 has been overexpressed in the heart. No uncoupling took place, probably due to high concentrations of ATP, ADP, and other purine nucleotides [79]. It is therefore speculated that UCPs (and other proteins capable of uncoupling) help to inhibit formation of reactive oxygen species (ROS) by not allowing the membrane potential to rise over a threshold value, thus preventing cell damage [80-83]. Supporting this idea, mild uncoupling caused by free fatty acids was observed to prevent the generation of hydrogen peroxide in plant mitochondria [84,

85]. A rise in proton conductance of various types of mitochondria (muscle, kidney, BAT, spleen, β-cells) caused by superoxide (created by addition of xanthine and xanthine oxidase) in the presence of palmitate was also reported [83]. This rise was inhibited by purine nucleotides, and therefore probably connected to different UCPs. However, it is not clear if superoxide has a direct effect on the protein or if it acts indirectly (*e.g.* via chemical modification of fatty acids).

The function of other UCPs is currently intensely investigated.

2.4   Uncoupling protein 2

UCP2 has a molecular mass of 32 kDa and is expressed widely in humans. UCP2 mRNA has been found in white and brown adipose tissue, skeletal muscle, heart, liver, kidney, pancreas, brain, and cells of immune system (leukocytes, monocytes and macrophages) [86, 87]. Nevertheless, content of UCP2 in all of these tissues is still by one or two order of magnitude lower than content of UCP1 in BAT [88]. However, the data of UCP2 amount were obtained only from measurement and quantification of mRNA due to the lack of suitable antibodies, which makes the direct quantification of protein difficult. Care is needed when extrapolating from mRNA level to protein expression, even more to protein activity.

Not much information is available on molecular properties of UCP2 itself. It is usually assumed that UCP2 has identical properties to UCP1. Although UCP2 was established as mitochondrial transporter, transport substrates are still being recognized. Besides FAs, especially polyunsaturated fatty acids (PUFAs), also downstream by-products and end-products of lipid peroxidation such as hydroperoxy FAs liberated from phospholipids by phospholipase A2, as well as nitrolinoleic acid have been shown as UCP2 transport substrates [89]. Moreover, 4-hydroxynonenal (HNE) [90, 91] and similar compounds have been suggested to activate UCP2 [92].

Likewise for UCP1, modified models of uncoupling for UCP2 have been proposed. A common prediction of models [56, 93] is that compounds arising from lipid peroxidation may initiate function of UCP2, hence may activate UCP2-mediated uncoupling [89, 92]. Even if this uncoupling cannot reach a high extent (in terms of mitochondrial membrane potential, $\Delta \Psi_m$, - rather mere decreases of single units of mV are expected) due to a minute amounts of UCP2 expressed in tissues [94, 95]. However, even such a "mild uncoupling" possesses the ability to significantly attenuate mitochondrial production of superoxide on both Complex III [96, 97] and Complex I [98-100] sites. This ability led to suggestions of a feedback suppression of oxidative stress and particularly lipid peroxidation by its intermediates [89, 92, 101]. Note, that according to the nature of the model for UCP2 transport mechanism (due to the considered transport

substrates), distinct reactive species might play a role in such a feedback mechanism. Theoretically, in the case, if UCP2 is a pure protonophore and lacks the ability to translocate anions, certain "activating" species such as previously suggested HNE would serve a role in such a hypothetical feedback mechanism. HNE and the other reactive alkenals are near-terminal products of lipid peroxidation cascade originating from the PUFA chains still covalently bound to the lipids [90, 91]. Hence, their release is automatically ensured. In turn, according to the FA cycling hypothesis, cleaved-off free PUFAs or hydroperoxy PUFAs [89] represent the exclusive substrate alternative.

Reconstitution studies have shown some functional similarities of UCP2 to UCP1, such as the essential requirement for fatty acid to provide uncoupling and inhibition by ATP, GDP, and other nucleotides [52, 94, 102, 103].

2.4.1 Possible physiological roles of UCP2

More than a decade of UCP2 studies did not answer the basic question of its function in mitochondria and its physiological role, neither demonstrated in indisputable manner exemplar situations under which such roles might be executed. Scientists would hardly find more controversial field, where both mechanism as well as a physiological role were disputed for a studied protein.

On the basis of findings about UCP1, it has been originally suggested that physiological role of UCP2 may involve regulation of body weight, fever, or other processes of adaptive thermogenesis. However, after creation of knockout (KO) mice, it was revealed that mice lacking *Ucp2* gene are not obese (body weights in wildtype and *Ucp2*-KO mice are equivalent) and have a normal response to cold exposure or a high-fat diet. Significantly different, however, was their phenotype with regard to ROS production [80] and β-cells insulin secretion [104]. The attention was therefore shifted to attenuation of ROS formation [8, 56, 93, 105, 106] since mild uncoupling can be principal regulator of oxidative stress, besides ROS protection has a wide implications to cell physiology and pathology. Among other physiologically acceptable roles of UCP2, regulation of glucose-stimulated insulin secretion (GSIS) [107, 108], regulation of mitochondrial Ca^{2+} handling [109-111], atherosclerosis, and neuroprotection have been proposed (see bellow).

2.4.2 UCP2 and immunity response

As already mentioned, UCP2 is highly expressed in the cells of immune system and several studies confirmed important physiological role of UCP2 in regulation of immunity response. Arsenijevic *et al.* [80] have investigated the response to *Toxoplasma gondii* infection

in *Ucp2 (–/–)* mice, and found that the mice are completely resistant to infection, in contrast with the high lethality observed in wildtype (WT) littermates. During this chronic infection, *T. gondii* cysts were nearly three times more numerous in WT mice than in KO mice. To explain this observation, they isolated macrophages from WT and mutant mice and compared their ability to eliminate *T.gondii in vitro*. They found that macrophages isolated from *Ucp2 (–/–)* mice have 80% increased ROS production and greater toxoplasmacidal activity even *in vitro*. Therefore, they concluded that the ability of *Ucp2 (–/–)* mice to more efficiently resist to *T.gondii* infection is related to greater capacity of their macrophages to generate ROS.

Rousset *et al.* [112] extended this work by the observation that UCP2 influences the early stage of immune response. During acute *Listeria monocytogenes* infection, *Ucp2 (–/–)* mice had lower level of anti-inflammatory cytokine Interleukin 10 (IL10). This cytokine mediates its anti-inflammatory effect by inhibiting pro-inflammatory cytokines production. Indeed, low level of IL10 at day 3 after infection resulted in higher level of pro-inflammatory cytokines interferon-γ, IL6, and IL1β and of the chemokine Monocyte chemoattractant protein-1 (MCP1) at day 4 in *Ucp2* ablated mice. This consequently led to significantly higher amount of recruited phagocytes in the spleen of *Ucp2* (−/−) mice and more efficient immune response. Bacterial lipopolysaccharide (LPS) is an endotoxin, which binds to the CD14/TLR4/MD2 receptor complex and thus promotes the secretion of pro-inflammatory cytokines in many cell types, but especially in macrophages. It has been observed that treatment of isolated macrophages with LPS causes decrease of their UCP2 mRNA and protein levels [113]. Recently, it has been published that UCP2 downregulation after LPS treatment is mediated by Mitogen-activated protein kinases (MAPK) family, namely p38 and c-Jun N-terminal kinase (JNK) signalling pathways. In fact, the authors suggested a signal amplification loop, in which this downregulation of UCP2 protein leads to increased level of mitochondrial ROS production in macrophages, which in turn intensifies MAPK signalling [114]. Furthermore, it was observed that overexpression of *UCP2* in macrophage cell line negatively regulates level of nitric oxide generation induced by LPS treatment. This would imply that UCP2 is involved in regulation of generation of bactericidal agens peroxinitrite, which derives by combination of superoxide and nitrogen monoxide (NO) [115].

2.4.3   UCP2 and atherosclerosis

Negative role of ROS in formation of atherosclerotic plaques is well established. Blanc *et al.*[116] investigated, whether UCP2 has a protective role in etiology of this disease. They used low density lipoprotein receptor knockout mice, which are prone to atherosclerosis, and destroyed their bone marrow by irradiation. Subsequently, they performed bone marrow

transplantation with wildtype or *Ucp2 (–/–)* donors. After feeding the mice with atherogenic diet for 7 weeks, they observed significant increase in atherosclerotic lesion size in the aortic sinus and thoracic aorta of *Ucp2 (–/–)* transplanted mice. Analyses of plaque composition revealed a significant increase in macrophage accumulation, apoptotic cell death, and also decrease in collagen content. Nitrotyrosine staining confirmed higher level of ROS in plaques from *Ucp2 (–/–)* transplanted mice. Previous observations are in agreement with the work of Ryu *et al.* [117], who have shown that THP1 monocytes with *UCP2* overexpression had lower protein and mRNA levels of ß2 integrins. Consequently, adhesion of these monocytes to Tumor necrosis factor-α (TNF)–stimulated Human aortic endothelial cell (HAEC) monolayers and to plates coated with intercellular adhesion molecule-1 was reduced. *UCP2* overexpression also inhibited cell spreading and actin polymerization in monocytes treated with TNF-α and MCP-1, and reduced MCP-1–induced transmigration of monocytes through HAEC monolayers.

2.4.4   UCP2 and neuroprotection

Evidence is accumulating that UCP2 is also involved in neuroprotection. Mattiasson *et al.* [118] have demonstrated that UCP2 prevents cell death in global cerebral ischemia. Following cerebral ischemia, the levels of glucose and oxygen rapidly reduce and thus also levels of ATP production by mitochondria are lowered. The main consequence of such energy deficit is a neuronal depolarization with postsynaptic release of glutamate. The binding of glutamate to its receptors on postsynaptic neurons induces entry of Ca^{2+} into the cell. This activates a cascade of intracellular events leading to cell death. In mice overexpressing human UCP2, brain damage after cerebral ischemia was diminished after experimental stroke and traumatic brain injury, and neurological recovery was enhanced. In cultured cortical neurons, UCP2 reduced cell death and inhibited caspase-3 activation induced by oxygen and glucose deprivation. The authors proposed that UCP2 neuroprotective effect can be explained by lowering membrane potential, which is known to decrease the level of Ca^{2+} accumulation in mitochondria. The accumulation of intramitochondrial Ca^{2+} is generally associated with release of cytochrome c and other events leading to apoptosis or cell death.

2.4.5   UCP2 and connection with type-2 diabetes

ATP/ADP ratio is important factor for regulating insulin secretion of pancreatic β-cells (see chap. 2.5.2). If this ratio is decreased by uncoupling of oxidative phosphorylation, the effect of glucose on insulin secretion is reduced. Given the proton leak activity of UCP2, hence its predicted negative effect on ATP synthesis, it was suggested that UCP2 could be a negative regulator of insulin secretion in β-cells. Since 2000, there has been increasing evidence that this

hypothesis is relevant. It was first indicated by adenovirally mediated overexpression of *UCP2* in isolated pancreatic rat islets as well as in insulin-secreting, INS-1 cultured cells, which led to the decreased ATP content and inhibited GSIS [119]. Somewhat conflicting data were obtained using a related approach in which UCP2 was overexpressed in islets isolated from obese Zucker diabetic fatty (ZDF) rats. These animals lack normal leptin receptors, develop obesity-induced type-2 diabetes melitus (T2DM), and have defective GSIS. In apparent contrast to normal rat islets, *UCP2* overexpression in ZDF islets improved GSIS [120].

In 2000, *Ucp2* knockout mice were prepared by Zhang *et al.* [107] They showed that pancreatic islets of Langerhans from *Ucp2* KO mice have increased insulin secretion in response to glucose and lower glucose blood level than control animals.

The set of *in vivo* experiments with mice fed a high fat diet showed that WT mice significantly increased their fasting blood glucose compared with control diet WT mice, but this increase did not occur in *Ucp2 (–/–)* mice. *Ucp2 (–/–)* mice also had significantly lower fed blood glucose concentrations compared with WT mice on either diet. Fasting and fed plasma insulin concentrations rose in both WT and *Ucp2 (–/–)* mice compared with the control diet-fed animals. However, the increase in insulin secretion was higher in HFD *Ucp2 (–/–)* mice compared with HFD WT mice [121].

Furthermore, Zhang *et al.* [107] showed that the leptin-deficient *ob/ob* islets, in which insulin secretion is unresponsive to glucose, expressed much higher levels of UCP2 than control islets. The authors then crossed the *ob/ob* mice with the *Ucp2*-KO mice and showed that the *ob/ob* mice lacking UCP2, although still severely obese, were partially rescued from the development of diabetes as a result of improved β-cell function.

De Souza *et al.*[122] examined effects of short-term treatment of animal models of T2DM with an antisense oligonucleotide RNA to UCP2. The treatment resulted in a significant improvement of hyperglycaemic syndrome. This effect was due to an improvement of insulin secretion, and also to improved peripheral insulin action.

Thus these studies indicate that UCP2 may be a link between obesity, β cell dysfunction, and T2DM. Moreover, there are several reports that associate different polymorphisms in the *UCP2* gene directly with obesity and/or higher risk for development of T2DM. For example, the single nucleotide polymorphism in position -866 of the *UCP2* promoter modulates *UCP2* transcriptional activity in adipose tissue and pancreatic β–cells, which is associated with variations of body mass index and insulin secretion in nondiabetic subjects, respectively. GSIS is significantly lower and insulin sensitivity is reduced in carriers of the -866A/A genotype compared with -866G/G homozygotes or heterozygotes [123]. Type-2 diabetic patients with the A allele need insulin therapy earlier and show higher frequency of insulin treatment [124-126]. Taken together, the more common *UCP2* promoter G allele, while being conductive for obesity,

affords relative protection against T2DM [127].

Two other polymorphisms were also associated with obesity and diabetes: the insertion/deletion in untranslated region of exon 8 and amino acid substitution of valine for alanine in exon 4 of the gene [128, 129].

2.5   β-cell physiology and pathophysiology

2.5.1   Glucose homeostasis

Glucose homeostasis regulates the concentration of glucose in the blood and maintains it within a remarkably narrow range. Glucose homeostasis is controlled primarily by the anabolic hormone insulin and also by several insulin-like growth factors. Insulin is secreted from the pancreas in response to the increase in plasma glucose following a meal. Insulin decreases the plasma glucose concentration by promoting the uptake of glucose into tissues, intracellular glucose metabolism, and glycogen synthesis. Several catabolic hormones (glucagon, catecholamines, cortisol, and growth hormone) oppose the action of insulin; they are known as anti-insulin or counter-regulatory hormones [138-140]. They stimulate both the release of glucose from glycogen stores and its *de novo* synthesis, thus causing an increase in glucose concentration in plasma. The fine balance between insulin and glucagon action is a key factor in the control of fuel metabolism. Glucagon and insulin are both secreted from the same anatomic location - the pancreatic islets of Langerhans, which constitute approximately 1 to 2 % of the mass of the pancreas. There are approximately one million islets in a healthy adult human pancreas, which are distributed evenly throughout the organ (see Figure 4 E). Glucagon is secreted by α-cells, whereas insulin is secreted by β-cells. β-cells constitute approximately 60 % of all islet cells (see Figure 4 F). In islets, there are at least three other kinds of endocrine cells, δ cells - secreting somatostatin, PP cells - secreting pancreatic polypeptide, and ε cells - secreting ghrelin (see Figure 4 A-D) [141-143].
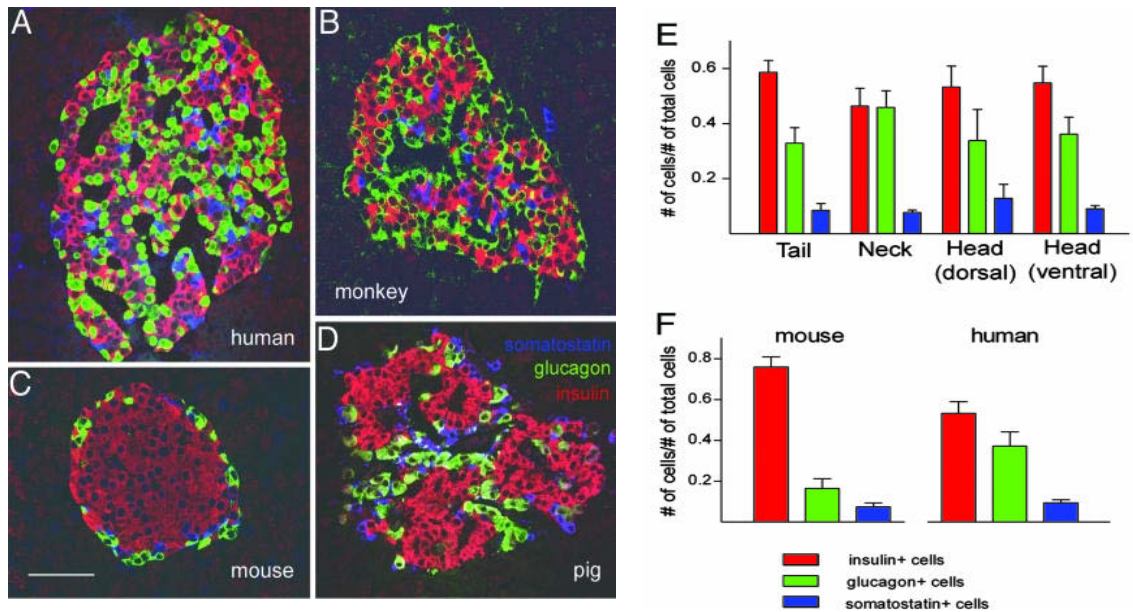
Figure 4 Interspecies differences in morphology of Langerhans islets.

(A–D) Confocal micrographs (1-µm optical sections), showing representative immunostained pancreatic sections containing islets of Langerhans from human (**A**), monkey (**B**), mouse (**C**), and pig (**D**). Insulin-immunoreactive (red), glucagon-immunoreactive (green), and somatostatin-immunoreactive (blue). (**E**) Quantitative enumeration of the contribution of insulin-, glucagon-, and somatostatin-immunoreactive cells to the composition of islets in four different regions of the human pancreas. (**F**) Comparison of the cell composition of human islets with that of mouse islets (adopted from [141]).

2.5.2   *Possible mechanism of β-cell glucose sensing*

Insulin secretion is controlled by nutrients and by hormonal and neural factors[144-146]. Among these, glucose is by far the most important regulator of the machinery of insulin secretion [147-149]. However, the precise mechanism of glucose-derived signal(s) controlling GSIS in β-cells is still unclear.

The primary glucose transporter responsible for shuttling glucose into the β-cells of rodents is glucose transporter 2 isoform (GLUT2). Note that in peripheral tissues isoform GLUT4 is the major glucose transporter. The GLUT2 transporter has quite low affinity for glucose but high transport capacity. Apart from β-cells, GLUT2 is expressed only in the liver and intestine. It has been shown that transport activity via this transporter can be modulated by phoshorylation of GLUT2 by protein kinase A [150]. In addition to GLUT2, human β-cells widely express GLUT1. Unlike GLUT2, this transporter has high affinity and also high transport capacity [151]. Therefore, human β-cells possess quite a huge transport potential for glucose. This fact could help explain, why the sigmoid curve of insulin secretion dependency on glucose concentration by humans is shifted to the left in contrast to rodents.

As in other cells, in β-cells glucose ultimately undergoes glycolysis. The first step of glycolysis is phosphorylation of glucose by glucokinase; this is also the rate limiting step of

glycolysis [152, 153], whereas transport into β-cells greatly exceeds the rate of its phosphorylation. High rates of glycolysis are maintained through the activity of mitochondrial shuttles, mainly the glycerophosphate and malate/aspartate shuttles [154, 155], which allow the reoxidation of cytosolic NADH. The end product of glycolysis is pyruvate. A particular feature of the β-cell is not only the tight link between glycolysis and mitochondrial oxidative metabolism, but also the extremely high proportion of glucose-derived carbons oxidized in the mitochondria [156]. The very low expression of monocarboxylate transporters in the plasma membrane and the low activity of lactate dehydrogenase act conjointly to drive pyruvate into the mitochondria [157-159]. Therefore the most plausible mechanism of GSIS assumes that the glucose sensor is represented by mitochondria of pancreatic β-cells[160].

Elevating oxidative phosphorylation linked to glycolysis leads to enhanced ATP production in the matrix of mitochondria and its export to the cytosol, thereby the cytosolic ATP/ADP ratio, plasma membrane depolarization due to closing of the K_{ATP} channel and opening of the voltage dependent Ca^{2+} channel. However, there are still many questions that remain unanswered. Exactly how K_{ATP} channels are regulated *in vivo* is still unclear. When pancreatic β-cells are exposed to increasing concentrations of glucose the activity of K_{ATP} channels decreases [161, 162]. However, the ATP concentration required to cause half-maximal inhibition of channel activity is approximately 10 μM in *in vitro* experiments [163, 164]. Because intracellular ATP concentration in β-cells is normally in the millimolar range, theoretically no channel activity would occur [162].

The other problem is the seemingly small effect on ATP concentration of various substrates, including those that markedly enhance insulin secretion such as glucose [165-168]. This leads to the question, whether ATP really is the critical physiological regulator of K_{ATP} channel activity. In contrast to ATP, only a small fraction of total cellular ADP is free. It was found that increased glucose concentration from 0 mM to 30 mM was associated with a tenfold decline in the concentration of free ADP (starting at approximately 50 μM ADP at 0 mM glucose), whereas the concentration of ATP remained nearly constant. These data suggest that a sharp decrease in free ADP with only a relatively small change in ATP concentrations is the characteristic feature of the response of β-cells to glucose stimulation [166, 169, 170].

This leads to the conclusion that a considerable increase in glycolitic flux and a sharp decrease in free ADP levels could be the necessary conditions leading to closure of K_{ATP} channels and to insulin release following glucose challenge. In the absence of glucose, enough K_{ATP} channels are opened to dictate a hyperpolarized resting membrane potential of -70 mV [171]. Closure of the K_{ATP} channels results in depolarization of the plasma membrane. Once the membrane potential is more positive than about -40 mV, Ca^{2+} channels open, allowing the influx of extracellular Ca^{2+}. The resulting rise in cytoplasmatic Ca^{2+} concentration then triggers

exocytosis of secretory granules containing insulin [172] (see Figure 5).
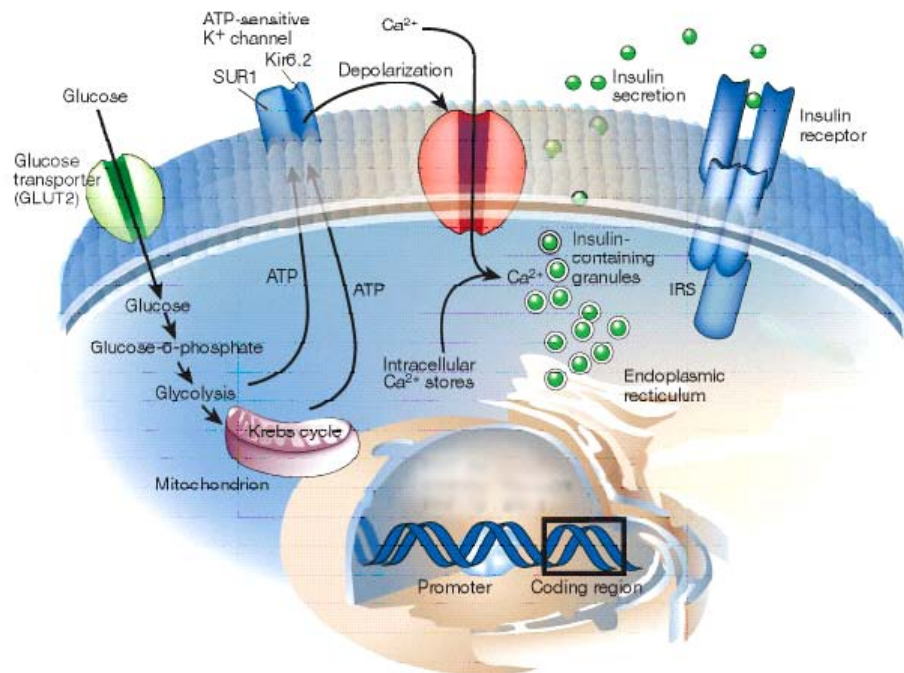
Figure 5 Model of pancreatic β-cell sensing.

Glucose is transported into the β-cell by the glucose transporter 2 isoform (GLUT2). The generation of ATP by glycolysis and the Krebs cycle leads to closure of the ATP-sensitive K$^+$ channel – a hetero-octamer comprised of four subunits of the sulphonylurea 1 receptor (SUR1) and four subunits of the inwardly rectifying K$^+$ channel Kir6.2. The closing of the ATP-sensitive K$^+$ channel leads to depolarization of the plasma membrane and influx of extracellular calcium. Together with calcium mobilized from intracellular stores, this leads to fusion of insulin-containing secretory granules with the plasma membrane and the release of insulin into the circulation. The pancreatic beta-cells have insulin receptors and there is evidence for an autocrine action of insulin on beta-cell function, including transcription of the glucokinase and insulin genes (adopted and modified from [147])

Although changes in cytosolic ATP/ADP ratio are believed to be the key factor for β-cell sensing, also other downstream intermediates of glucose metabolism and tricarboxilic cycle, can play any role in modulation of GSIS (*e.g.*[149, 173-175]). Kibbey *et al.* [176] pointed out that another purine nucleotide – GTP better reflects rates of glucose oxidation in a cell. Both ATP and GTP are metabolically generated in the mitochondrial matrix, except for a small amount of ATP, which is synthesized in the cytosol by substrate phosphorylation during the glycolysis. Mitochondrial ATP is produced predominantly by oxidative phosphorylation and thus is dependent on the mitochondrial membrane potential generated primarily from NADH oxidation. Only a small fraction of ATP is directly formed in the tricarboxylic acid cycle by the isoforms

of succinyl-CoA synthetase. In principle, between 1 and 29 mitochondrial ATP are generated per molecule of glucose metabolized, depending on the tightness of coupling between mitochondrial membrane potential and ATP synthesis. Unlike the widely varying synthesis efficiency, changes in the matrix ATP/ADP ratio are relatively limited due to the rapid export of mitochondrial ATP to the cytosol via the ATP/ADP antiporter. Thus, at least within the matrix, ATP production rates do not necessarily reflect rates of glucose oxidation. In distinct contrast, mitochondrial GTP is produced only by the GTP-specific isoform of succinyl-CoA synthetase with each subsequent turn of the tricarboxilic acid cycle. Assuming similar fluxes through each isoform, approximately one molecule of GTP will be generated per molecule of oxidized glucose. Thus, GTP production is well poised to reflect metabolic activity at least within the matrix. Experiments with a silenced ATP-isoform of succinyl CoA show increased insulin release, which is not associated with an increase in the ATP/ADP ratio. Conversely, when GTP synthesis is decreased by silencing GTP-isoform, GSIS is impaired.

2.5.3   Role of ROS in β-cell physiology

Potential glucose-related pathways, through which ROS in cells can be formed, generally include autooxidation, oxidative phosphorylation, glycosylation, and the glucosamine pathways [208-210]. In the process of cell respiration, there are at least three stages that are associated with increased superoxide generation. These include increased substrate supply, decreased ADP concentration, and increased intracellular Ca^{2+} concentration.

The major source of ROS in pancreatic islets is still controversial. Some studies implicate the expression and activity of NADPH oxidase (the same system used by macrophages against bacteria) as the major source of glucose stimulated ROS [211]. The main location of superoxide generation in mitochondria is the respiratory chain, namely NADH dehydrogenase at Complex I [99, 100] and the interface between ubiquinone and complex III [96, 97]. Superoxide is a very reactive molecule. In the worst case, hydroxyl radical can be created by its reaction with water, which is even more reactive and causes cell damages. Most of the superoxide is converted to less reactive hydrogen peroxide by superoxide dismutase (SOD) isoenzymes, and finally to oxygen and water mainly by catalase, glutathione peroxidases (GPxs) and peroxiredoxin.

There are many indications that deteriorating glycemic control in type-2 diabetes causes oxidative stress on β-cells, and this may be due to the fact that Langerhans islets have the lowest intrinsic antioxidant capacity compared with other metabolic tissues, such as liver, kidney, skeletal muscle, and fat. It was reported that islets contain relatively small activities for the major antioxidant enzymes, Cu/Zn SOD, Mn SOD, catalase, and GPx [212]. This observation was more recently reinforced by the interesting observation that high glucose concentrations

caused cellular stress in islets (as indicated by a rise in the heme oxygenase-1 protein amount), but did not induce higher activities of the antioxidant enzymes [213]. This suggests that the islet is among the most vulnerable tissues during times of oxidative stress. Despite this, the catalytic capacity of β-cells for conversion of superoxide into H_2O_2 in cytoplasm and mitochondria is considered to be physiologically sufficient [214]. However, levels of the H_2O_2 inactivating enzymes are extremely low in β-cells, composing only 1% of the expression levels in the liver [215]. On the other hand, this may provide a system that is sensitive to reactive oxygen species as a signal. Some reactive oxygen species seem to serve as physiological mediators of many cellular responses and this raises the question of whether these molecules could contribute to signaling by glucose sensing in β-cells. Unlike superoxide, H_2O_2 is a stable and uncharged molecule. That is why it is freely diffusible and it can be rapidly synthesized and destroyed in response to external stimuli. By this definition, H_2O_2 arguably meets the important criteria for an intracellular messenger, and a growing body of evidence supports this hypothesis. To date, many important signal transduction molecules or processes in β-cells that potentially regulate insulin secretion have been recognized as downstream targets of H_2O_2, including K^+_{ATP} channel, Ca^{2+} influx and release, and many others [216, 217].

Despite a positive role of ROS in GSIS, excessive and/or sustained ROS production can directly or indirectly disturb the integrity and physiological function of cellular macromolecules such as DNA, proteins or lipids. Such disturbances contribute to the pathogenesis of various diseases, including diabetes. Most cells, including β-cells, have intricate mechanisms of defense against ROS toxicity. In response to oxidative stress, cells increase intracellular antioxidant potential by directly increasing transcription of many so-called antioxidant enzymes. Besides the enzymes mentioned above, UCP2 also seems to have a role, although the mechanism of decreasing ROS by UCP2 may be indirect.

Experiments with *Ucp2* knockouts showed that ROS levels are elevated in control *Ucp2* (−/−) islets as compared to wildtype and *Ucp2* (−/−) islets overexpressing *Ucp2*. Palmitate increases ROS in wildtype and *Ucp2* (−/−) islets overexpressing *Ucp2* but not in *Ucp2* (−/−) islets. Thus, *Ucp2* (−/−) islets resist the toxic effects of palmitate by maintaining glucose-dependent metabolism-secretion coupling. Moreover, higher free fatty acid oxidation rates prevent accumulation of triglyceride in *Ucp2* (−/−) islets, such accumulation being associated with lipotoxicity. Pancreatic islets isolated from *Ucp2*-deficient mice maintain GSIS after chronic hyperglycemia, and GSIS is not improved further by removal of superoxide, which indicates that superoxide-mediated loss of glucose sensing is specifically caused by the activation of UCP2 [218].

2.5.4 Role of free fatty acids in GSIS

Fatty acids are stored in adipocytes in esterified form as triglycerides. Under starvation conditions, FAs are released from adipose stores into the blood stream and serve as an important energy source. However, FFAs have been found to have a broader function and can exert the ability to act as potent signaling molecules in a variety of cellular processes in many cell types, including β-cells. It is now clear that FFAs play a very important role in β-cell dysfunction. There is strong evidence that fatty acids, which under normal circumstances are physiological fuels for the β-cell, become toxic when present at elevated concentrations for prolonged periods of time (first shown by Zhou and Grill [177]). Adverse effects of chronic exposure of the β-cell to elevated fatty acid concentrations include decreased GSIS, impaired insulin gene expression, and increased cell death [178-180]. However, it seems that in the presence of physiological glucose concentrations, excessive fatty acids are readily disposed of through mitochondrial β-oxidation. In contrast, when both fatty acids and glucose are elevated, accumulation of metabolites derived from fatty acid esterification impairs β-cell function. This is supported by several observations. *In vitro*, prolonged exposure of isolated rat islets to palmitate inhibits insulin gene expression only in the presence of high glucose. This is accompanied by a glucose-dependent increase in neutral lipid synthesis. *In vivo*, the glucose-lowering agent phlorizin, but not the lipid-lowering agent bezafibrate, lowers islet triglyceride content and prevents the decrease in insulin mRNA levels in ZDF rats [181]. Finally, a HFD impairs GSIS in hyperglycemic Goto Kakizaki (GK) rats, but not in normoglycemic Wistar rats, an effect prevented by normalization of blood glucose in GK rats [182]. Overall, these findings support the hypothesis that lipotoxicity only occurs in the context of chronic hyperglycemia, consistent with the observation that most individuals with increased circulating lipid levels have normal β-cell function [183].

The accute effect of FFAs on β-cells is enhancement of insulin secretion [184, 185]. As with a glucose stimulus, there is an increase in intracellular calcium concentration but this increase is probably independent on K_{ATP} channel [186]. Nevertheless, the long-term effect on GSIS is negative. When exposed to palmitate, oleate or stearate for 48 hours, rat islets exhibit increased insulin secretion at basal glucose levels, but a profound inhibition of GSIS [108, 187, 188]. In addition to the fact that FFAs inhibit gene expression at the mRNA level [189], there are four major points at which FFAs might contribute to the inhibition of GSIS:

1) The simultaneous presence of elevated glucose and fatty acids results in accumulation of cytosolic citrate, the precursor of malonyl-CoA, which in turn inhibits carnitine-palmitoyl-transferase 1 (the enzyme responsible for transport of activated fatty acids into mitochondria) and subsequently results in accumulation of long-chain fatty acyl-CoA. The accumulation of

long-chain fatty acyl-CoA mediates the deleterious effect of fatty acids on GSIS [190, 191].

2) FFAs induce accumulation of triglycerids in β-cells. GSIS appears to be inversely correlated with triglyceride content [192].

3) FFAs activate/open the K_{ATP} channel in β-cells [193].

4) Expression of *UCP2* in β-cells is increased by FFAs.

How FFAs upregulate *UCP2* expression is not yet clear, although FFA oxidation and peroxisome proliferator-activated receptors (PPARs) pathway have been suggested. *PPAR-γ* is a member of the ligand-dependent transcriptional factors and is mainly expressed in adipose tissue, hematopoetic cells, and the immune system [194]. PPAR-γ is also present in rat islets, including in β-cells, and it is known to be involved in many cellular functions as a crucial transcription factor to upregulate expression of the lipogenic enzymes. Its overexpression in β-cells significantly suppresses insulin secretion induced by stimulatory concentrations of glucose due to higher expression of *UCP2* [195]. Also, another member of the PPARs, *PPAR-α*, and its adenoviral overexpression led to double expression of *UCP2* in insulinoma cells [196]. Higher expression of *PPAR-α* and *γ* in β-cells is also caused by chronic exposure to elevated concentrations of FAs [197, 198].

Moreover, experiments with oleic acid and 48-h exposure of INS-1(832/13) β-cells identified an enhancer region (-86/-44) of the *UCP2* promoter, which is responsible for both basal and FFA-stimulated *UCP2* gene transcription [199, 200]. The enhancer contains tightly clustered Sp1 (universal transcription factor), sterol regulatory element (SRE), and double E-Box elements. While all three sequence motifs are required for basal activity of the *UCP2* promoter, mutations in either the SRE or the E-Box elements eliminate the response to FFAs. The SRE and sterol regulatory element binding protein-1 (SREBP1) appear to be crucial to the response of the *UCP2* gene to FFAs, since overexpression of the nuclear forms of the *SREBP*s increases *UCP2* promoter activity by 7–10-fold and restores the ability of E-Box mutants to respond to oleic acid. Therefore, it seems that SREBP is the major modulator of *UCP2* gene transcription by FFA, while E-Box binding factors play a supportive role.

2.5.5   *Diabetes mellitus*

Diabetes mellitus is a heterogeneous group of disorders characterized by high blood glucose levels and resulting adverse pathogenesis. It is becoming a major threat to public health in the 21st century. The past two decades have seen an explosive increase in the number of people diagnosed with diabetes. Diabetes is the sixth leading cause of death and this is mainly due to its cardiovascular complications. The macro- and micro-vascular consequences of the disease represent a major economic burden worldwide. It seems the incidence of this disease

will grow even more rapidly in the future from the current estimate of 150 million to 220 million in 2010, and 300 million in 2025 [130]. The main causes for such "an epidemic" are seen in the changes in human behavior and lifestyle over the last century.

There are two main forms of diabetes, type-1 and type-2. Type-1, or insulin-dependent diabetes, is an autoimmune disease, in which the pancreatic β-cells are completely destroyed by the immune system, resulting in absolute insulin deficiency. People with type-1 diabetes must take exogenous insulin for survival. Its frequency is relatively low.

Over 90 % of diagnosed diabetes is type-2, which is "insulin-independent" and develops rather in adults. Type-2 diabetes is a polygenic disorder in nature and may involve polymorphism in multiple genes encoding the proteins involved in insulin signaling, insulin secretion and intermediate metabolism. Hence, type-2 diabetes is undoubtedly a multifactorial disease which is usually manifestation of a much broader disorder, commonly called the metabolic syndrome. The metabolic syndrome includes the T2DM and at least another two risk factors of following: hypertension, obesity, hypertriglyceridemie, or microalbuminurie [130].

In conjunction with genetic susceptibility, particularly in certain ethnic groups, T2DM is brought on by environmental and behavioral factors such as a sedentary lifestyle and excessive food intake [131]. When food intake chronically exceeds metabolic needs, efficient metabolism causes excess energy storage and it results in obesity, a common condition associated with T2DM, hyperlipidemia, and premature heart disease. However, recently T2DM has been recognized as an "oxidative stress" disease, which might inevitably develop during aging and is potentiated by the mentioned factors. Many clinical studies indicate that patients with T2DM are subjected to chronic oxidative stress caused by enhanced amounts of ROS. Pro-oxidants and markers for oxidative tissue damage, such as 8-hydroxy-deoxyguanine, HNE-proteins, 8-epi-prostaglandin F2α, hydroperoxides, and oxidation of DNA bases, have been reported to be elevated in serum, plasma, white blood cells, and pancreas biopsies of patients with T2DM [201-205]. Compared with nondiabetic control subjects, these markers demonstrated changes up to fivefold above normal value. Erythrocytes from diabetic patients contain low levels of the reduced form of glutathione (GSH), the primary intracellular antioxidant, high levels of the oxidized form (GSSG), and as a result reduced the GSH/GSSG ratio [206]. Intravenous infusion of GSH in type-2 diabetic patients improved insulin secretion and glucose tolerance during oral glucose tolerance tests (OGTT) [207].

People with this type-of diabetes are not dependent on exogenous insulin but may require insulin for control of blood glucose levels if this is not achieved with diet alone or with oral hypoglycemic drugs. The exact cause of type-2 diabetes is as yet unknown. The disease appears to start with development of insulin resistance in peripheral tissues, such as skeletal muscle or white adipose tissue, which leads to a compensatory over-secretion of insulin by the pancreas

due to an expansion of β-cell mass [132-134]. Regardless of the primary causes of type-2 diabetes, a common clinical course for patients is to respond to therapy initially by normalizing their fasting glucose levels, but then to undergo gradual deterioration in glycemic control despite optimal medical management using a variety of drugs. Even the initial response in fasting glucose may be misleading because many patients still manifest abnormal glucose levels postprandially. This scenario gives rise to the concept of glucose toxicity, which assumes chronic exposure to abnormally high levels of glucose over many years as a pathogenic force that leads to toxic effects on the β-cell. Chronic hyperglycemia leads to irreversible β-cell dysfunction, associated with impaired glucose-induced gene expression and secretion and, ultimately, reduced β-cell mass via apoptosis [135]. A number of mechanisms may contribute to glucotoxicity, including the induction of chronic oxidative stress and accumulation of advanced glycation end-products with subsequent damage to various cellular components. Hence, chronic hyperglycemia, the adverse outcome of the initial polygenic disorder, in time becomes a secondary adverse force on the β-cell, leading to a vicious cycle of continuous deterioration of β-cell function. Similar logic has been advanced to posit abnormal lipid levels as a causative force in the relentless deterioration of the β-cell. Proponents of this theory point out that most people with T2DM are obese individuals who tend to have elevated lipid levels in their blood that become higher as glycemia worsens, and that intra-islet lipid accumulation can decrease β-cell function. Moreover, nondiabetic family members of individuals with T2DM have been found to have metabolic abnormalities, such as elevated levels of circulating free fatty acids (FFAs) years before the development of impaired glucose tolerance (IGT) [136, 137].

Type-2 diabetes is diagnosed when the blood glucose levels exceed 6.1 mmol/l upon fasting, and 10 mmol/l 2 hours post-glucose load. Intermediate values of blood glucose between 6.7 and 9.9 mmol/l 2 hours post-glucose load indicate IGT, which often leads to overt diabetes [130].

Prevention and treatment of type-2 diabetes focus mainly on different strategies for improvement of insulin resistance and stimulation of insulin secretion. Better understanding of the cellular principles that lead to gradual β-cell failure in the face of insulin resistance could help to develop novel approaches based on reestablishing normal stimulus-secretion coupling in the β-cells.

2.6   Visualization of mitochondrial network

Mitochondria are currently recognized not only as the cell's powerhouse, but also as important modulators in the molecular physiology of the cell. The impairment of their function most frequently leads to oxidative stress causing cellular dysbalance or initiation of various forms of cell death, both being dominating processes in pathophysiology of numerous diseases and aging [219-225]. The oxidative stress stems in many cases from the elevated mitochondrial superoxide production. Moderate elevation of superoxide levels may participate in redox signaling, whereas repeated strongly self-accelerating oxidative stress might disrupt redox homeostasis in certain diseases and aging. Frequently, oxidative stress comes from electron transfer retardation, hence respiratory inhibition [91].

Predominantly, textbook images of mitochondrial morphology based on electron micrographs are represented by solitary shapes, which we now consider as sections of mitochondrial tubules. These kidney shaped organelles typically exhibit inner structures of folded sheet-like cristae [226]. Recent electron tomography data has however revealed different cristae shapes [227], showing that the inner membrane forms "sacks" with bottleneck outlets proximal to the outer membrane. Pioneering observations of Hackenbrock more than 40 years ago [226] revealed rapid and reversible changes of the mitochondria cristae shapes from the so-called "orthodox" to "condensed" conformations upon activation of ATP synthesis.

During the last two decades, it has been established that mitochondria of eukaryotic cells form a reticular network in most cell types. The network is continuously remodeled by cycles of fission and fusion events, giving rise to various mitochondrial reticulum shapes, ranging from long, branched, and interconnected tubules to solitary sacks or cisternae. The number of tubules, their connections, overall morphology, and subcellular distribution is thus dynamically altered. Consequently, mitochondrial network morphology must be linked to the mitochondrial function or state, thus reflecting specific cellular requirements or pathological states.

For remodeling of mitochondrial network, group of proteins called mitodynamins is responsible. The link between oxidative phosphorylation and activity of mitodynamins is given by GTP levels as most of the mitodynamins are GTPases [228]. The knowledge of upstream modulators of mitochondrial dynamics is still not complete. For example, Ca^{2+} was assumed to modulate the activity of dynamin and regulatory GTPases resulting in mitochondrial morphological alternations, perhaps through regulation of mitochondrial movement along the microtubule scaffold [229]. A fine balance between fusion and fission must exist as both processes in their extremes participate in apoptosis [230, 231], thus any serious deviation can have harmful effects on cells.

Recently, it has been recognized that not only common bioenergetic parameters – respiration, Δp and their components, electron and substrate fluxes, but also an overall morphology or dynamics of mitochondrial network within the living cells may reflect their bioenergetics, and therefore healthy or disease status [232-236]. Numerous evidence has been reported showing that mitochondrial morphology is crucially linked to the energy metabolism. A first link is given by the already mentioned GTP requirement for mitodynamins. GTP is produced by the Krebs cycle (in detail discussed in 2.5.2) or from ATP by matrix and cytosolic nucleoside diphosphate kinases. Its export mechanism from the matrix is unknown. Variations in respiration and their feedback to Krebs cycle and also changes in ATP levels might be connected to possible mitochondrial morphology modulators. In general, it seems that undisturbed highly efficient oxidative phosphorylation correlates with a highly interconnected, ramified network and enlarged cristae compartments, whereas low oxidative phosphorylation activity and high glycolysis correlate with bulkier or more spherical tubules, or 2D images of apparently solitary mitochondria displaying reduced intracristae space [232, 233]. Thus the mitochondrial network with apparently thinner, more branched, and interconnected tubules has been reported when cellular energy substrates were shifted from glycolytic to those allowing predominant oxidative phosphorylation.

The first super-resolution 3D imaging of mitochondrial networks has been reported by Egner *et al.* in yeast (*S. cerevisiae*) using 4Pi microscopy (see bellow) for imaging of their networks [237]. Utilizing 4Pi microscopy as well, details of a portion of mitochondrial reticulum recognizing tubule diameter of 200–400 nm in fixed mammalian cells have been reported by Medda *et al.* [238]. Also our group showed that mitochondria form a nearly completely interconnected tubular network with a fairly uniform tubule diameter of 270 ± 30 nm in insulinoma INS-1E cells and 280 ± 40 nm in hepatocellular carcinoma HEP-G2 cells, using a similar instrument [239].

A rich potential of mitochondrial morphology as a medical diagnostic tool has already been proven. Fragmentation of the mitochondrial network has been observed in fibroblasts from patients with alterations of mitochondrial energy production caused by genetic defects in respiratory chain subunits [234]. Mitochondrial fission is an early event in ischemic stroke *in vivo* and is also induced by nitric oxide in neurons [240]. Simulations of pathologies can be seen in manipulations of cell energetic status. Thus, when uncouplers like carbonyl cyanide 4-(trifluoromethoxy)phenylhydrazone (FCCP) were added to culture cells for time periods ranging from a minute up to a day, remodeling [241], fragmentation/fission of mitochondrial reticulum [242-245], apoptosis [246, 247], and changes in gene expression [248, 249] were observed.

2.6.1 A short introduction to high resolution microscopy

The optical resolution in far field light microscopy is limited mainly by diffraction. The axial resolution is poorer than the lateral due to the limitation of the aperture along the optical axis when focusing with a single lens. During the last two decades a handful of super-resolution microscopy techniques, that break the diffraction limit described by Abbe, have been developed.

In 4Pi microscopy, two opposing objectives are used to coherently illuminate the object simultaneously from both sides to give a greater total aperture [250-252]. Combining them coherently for fluorescence excitation as well as detection (4Pi microscopy of 'type C') enables three-dimensional (3D) imaging of fixed biological samples with ~ 7-fold improved axial resolution (see Figure 6) [253]. Its lateral (xy) resolution equals to that of a conventional confocal microscope, given by the Abbe's condition $\Delta r = \lambda / 2NA$, with NA denoting the numerical aperture of the lens and λ the wavelength of light. For widely used green fluorescent protein (GFP) and high NA objectives this xy resolution is about 250 nm.
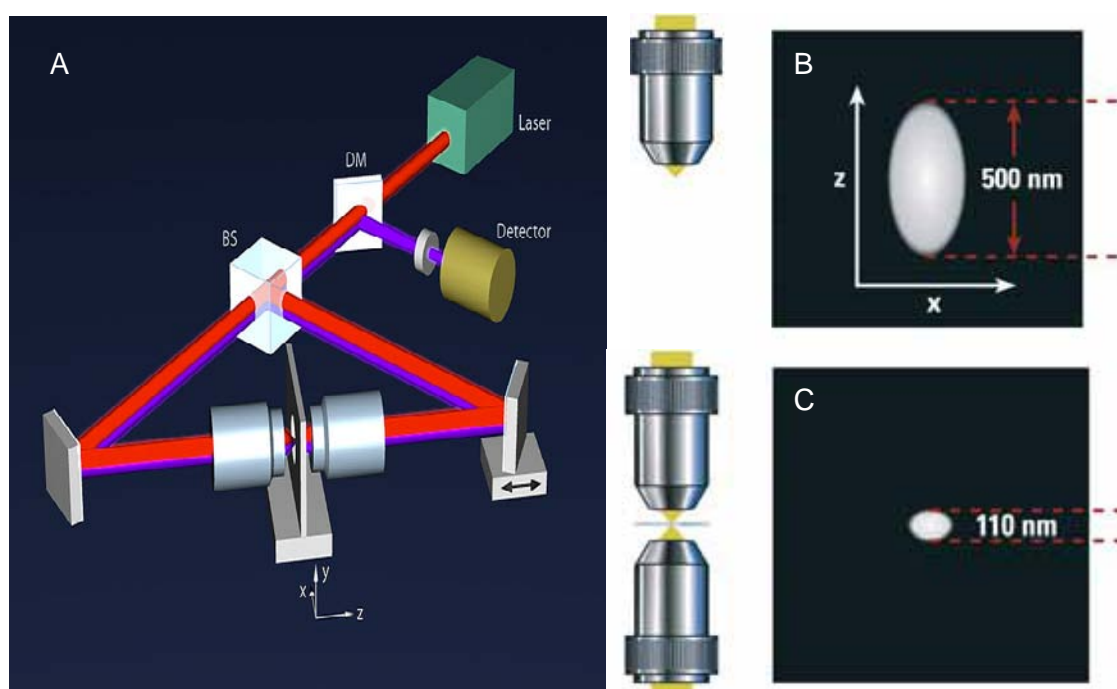
Figure 6 Scheme of a 4Pi microscope (**A**) and comparison of axial resolution of conventional confocal (**B**) with 4Pi microscopy (**C**)

The laser light is divided by a beam splitter (BS) and directed by mirrors towards the two opposing objective lenses. At the common focal point superposition of both focused light beams occurs. Excited molecules at this position emit fluorescence light which is collected by both objective lenses, combined by the same beam splitter and deflected by a dichroic mirror (DM) onto a detector (adopted from http://www.mpibpc.mpg.de/groups/hell/4Pi.htm and Leica letters).

New emerging super-resolution fluorescence microscopy techniques next to 4Pi microscopy go even further and enable sufficient resolution needed for observing of individual protein molecules (*e.g.* GFP). Stimulated emission depletion (STED) microscopy, first realized in 1994 [254], is overcoming Abbe's resolution limit by combining laser scanning microscopy with actively switching off fluorescent probes in the outskirts of the laser focus. This limits fluorescence emission to the center of the excitation laser focus and results in an effective lateral focus size (and hence resolution) of typically 25–70 nm (and better) across [255, 256]. To get a true 3D sub-diffraction resolution, STED has been combined with the 4Pi principle in a technique called *iso*-STED in which a true 3D resolution of ~ 45 nm has been achieved using organic Atto dyes [257, 258]. The *iso*-STED technique has been successfully used for 3D reconstruction of a part of the mitochondrial tubule outer membrane (immunostained) confirming the typical diameter of mitochondrial tubules of around 250 nm [257]. Recently, *iso*-STED has also been able to resolve cristae sacks in combination with the outer membrane contour of mitochondrial tubules [258].

In 2006, a new fluorescence wide-field microscopy-based technique has been developed which also achieves resolution well below 100 nm. Termed fluorescence photoactivation localization microscopy (FPALM or PALM) [259, 260] or stochastic optical reconstruction microscopy (STORM) [261] and published by three groups practically simultaneously, this technique takes an advantage of photophysically switching fluorescent probes [262, 263]. Instead of imaging all fluorescent probes at the same time, only a small fraction of photoactivatable (or photoswitchable) fluorophores is activated at any time and its fluorescence detected. The fraction of molecules is activated stochastically and at such a low density that the activated probes can be imaged as single molecules. Utilizing algorithms known from particle-tracking experiments over decades, these molecules can be localized to a much better accuracy than the width of their diffraction-limited images. Bleaching and subsequent imaging of many of these fractions (typically thousands), and combination of the determined particle positions finally renders a 2D image with 20 to 40 nm resolution. This scheme which had been originally proposed for 2D imaging recently got expanded to 3D imaging [264-266] and is now able to image sub-cellular structures at sub-100 nm 3D resolution.

2.6.2   *Animal models of T2DM*

There are several widely used animal models of T2DM.

Mice that harbor genetic mutations rendering them incapable of expressing functional leptin protein (*ob/ob*) or leptin receptor (*db/db*) are characterized by the development of obesity and T2DM. These mice are hyperphagic and insulin resistant, and have high circulating blood

insulin and glucose levels. This phenotype in *ob/ob* mice is rapidly normalized by leptin treatment [267-269].

Another model – ZDF rats is completely insensitive to the lipogenic action of leptin because of a Gln 269 → Pro mutation in the extracellular domain of leptin receptors [270, 271]. The lack of leptin activity in their islets is reflected by an increase in intracellular islet fat ranging from 10 to 100 times the normal [272].

Also Goto-Kakizaki rats have been used in numerous studies. GK rat is a spontaneous animal model of T2DM. This model was established by selective inbreeding of Wistar rats using high values in the OGTT. GK rats are characterized by no obesity, impaired GSIS, and peripheral neuropathy and renal disturbance as complications of T2DM are noted [273-275]. This model is characterized by an onset of Langerhans islet pathology, indicated by islet hypertrophy with a decreasing number of insulin-secreting β-cells [276, 277] . Possible causes of T2DM etiology in GK rats might include mitochondrial dysfunction, besides the reduced expression of several exocytotic soluble N-ethylmalemide-sensitive factor attachment protein receptor (SNARE) complexes, such as Syntaxin-1A, synaptosome-associated protein (SNAP-25), vesicle-associated membrane protein (VAMP-2), and nSec1/munc18 proteins. These complexes are important for the docking and fusion between insulin granules and β-cell membrane. Thus, a reduced number of docking granules would contribute to the impaired β-cell insulin secretion. Also the decreased mtDNA content in Langerhans islets [278] and skeletal muscle [279] has been reported during development of GK rats. It is not clear, whether it reflects diminished number of β-cells in an islet or number of mtDNA copies within a single remaining β-cell.

3 MATERIALS AND METHODS

All chemicals were purchased from Sigma unless stated otherwise.

3.1 Isolation of brown adipose tissue mitochondria

Brown adipose tissue mitochondria isolation protocol has been devised on the basis of Cannon and Lindberg procedure [280] with some modifications. Especially the addition of ATP into the sucrose isolation medium (SIM) was proposed by LaNoue *et al.* [281] to prevent loss of solutes and contraction of the matrix. SIM-A contained 250 mM sucrose, 10 mM morpholinopropanesulfonic acid (MOPS), 1 mM ethylenediaminetetraacetic acid (EDTA), pH 6.8 adjusted at 25 $^{\circ}$C with Tris. SIM-B and SIM-C had the same composition but 2 mM ATP, 2 mg/ml and 5 mg/ml FA-free bovine serum albumin (BSA), respectively, were included prior to use.

Adult male Golden Syrian hamster (Anlab) bred at 10 $^{\circ}$C for at least 3 weeks was anesthetized and decapitated. BAT depots were dissected out from the interscapular, axillary, cervical, and inner thoracic regions, cleaned from white adipose, muscle, and connective tissues, pooled into SIM-B, minced with scissors into pieces and homogenized by hand in a Potter-Elvehjem homogenizer with a Teflon pestle (Cole-Parmer). The homogenate was filtered through a cheesecloth, brought to volume of ~90 ml with SIM-B and centrifuged at 9,000 × g for 10 min. The floating fat layer was discarded. The pellets were resuspended into 90 ml of SIM-B and centrifuged at 900 × g for 10 min to remove cell debris. The resulting supernatant was centrifuged at 9,000 × g for 10 min. The pellets were resuspended into 10 ml of SIM-C and incubated with 1.8 g of Dowex Retardion 11A8 ion exchange resin (Sigma) for 1 h. The Dowex was filtered out. The filtrate was brought to volume of ~90 ml with SIM-C and centrifuged at 9,000 × g for 10 min. The final pellet was resuspended in 150 mM KCl, 10 mM MOPS, 1 mM EDTA, pH 6.8 adjusted at 25 $^{\circ}$C with Tris for mitochondrial respiration experiments. All above steps were carried at 4 $^{\circ}$C. The mitochondrial stock suspension was kept on ice in an open test tube. The protein content was estimated following the Lowry method with BSA as a standard [282].

3.2 Isolation of rat heart mitochondria

Rat was anesthetized and heart, while still beating, removed and placed into beaker, kept in ice, filled with ice-cold buffer contained 250 mM sucrose, 10 mM Tris-MOPS, 1 mM Tris-EDTA, pH 6.8. Heart was immediately cut into several pieces and the bloody buffer was

decanted. For each gram of heart tissue, 15 ml of fresh buffer, supplemented with 0.2 mg/ml Nagarse protease (Sigma) was added. The heart was then further minced with scissors and homogenized by hand in a Potter-Elvehjem homogenizer with a Teflon pestle. The homogenate was filtered through a cheesecloth and centrifuged at $1000 \times g$ for 5 min. Supernatant was then centrifuged at $10,000 \times g$ for 10 min. Resulting pellet was homogenized in fresh buffer with addition of 5 mg/ml BSA. Both the centrifugal steps were then repeated and the final pellet was then resuspended in buffer without BSA.

3.3   Measurements of BAT and rat heart mitochondria respiration and details of the carnitine cycle assay

Respiration was assayed in medium containing 50 mM KCl, 1 mM Tris-EDTA, 4 mM KP_i, 2 mM $MgCl_2$, 20 mM N-tris(hydroxymethyl)methyl-2-aminoethanesulfonic acid potassium salt (K-TES), pH 7.2, in a 2 ml glass chamber respirometer equipped with a Clark oxygen probe (YSI, USA) at $37^{o}C$. Routinely, 0.75 μM cyclosporin A was added to the respiratory medium prior to BAT or rat heart mitochondria addition (both 0.5 mg/ml). First, the carnitine cycle was induced by the addition of 0.2 mM ATP, 0.5 mM carnitine, and 10 μM Coenzyme A, to facilitate inward transport and β-oxidation of endogenous FAs. CoA initiates acylCoA synthesis (for which ATP is added), conversion of acylCoA into acylcarnitine by the carnitine-palmitoyl transferase-1, and transport of acylcarnitine, in exchange for the carnitine, to the matrix, where β-oxidation takes place. Induction of carnitine cycle results in well coupled BAT mitochondria.

In a standard experiment, after 5 min of carnitine cycle, 12.5 μM etomoxir, an inhibitor of carnitine-palmitoyl transferase-1, was added to prevent further import and β-oxidation of the subsequently added FAs, and also 2.5 μM carboxyatractyloside (CAT) and 1 μg/ml oligomycin were added, to prevent FA cycling mediated by the ADP/ATP carrier and H^+ leak on F_O-ATPase, respectively. Then, either 5 mM pyruvate and 5 mM malate or 5 mM citrate and 5 mM malate were added from their Tris-buffered stock solutions. The first phase of rapid O_2 uptake indicated respiration of endogenous substrates, as it occurred also in the presence of 12.5 μM etomoxir. A subsequent slow decline of respiration indicated proceeding β-oxidation. With etomoxir added from the beginning, a highly uncoupled respiration of BAT mitochondria occurred after subsequent addition of substrates, obviously due to the un-combusted endogenous FA. Similar pattern (but less pronounced) was found with heart mitochondria.

3.4   Monitoring of mitochondrial membrane potential by safranine fluorescence

The changes in the IMM potential were monitored by safranine fluorescence. Safranine

fluorescence is inverse proportional to $\Delta\Psi_m$. Mitochondria, typically 0.5 mg/ml, were incubated 5 min with 5 μM safranine in 2 ml fluorescence cuvette. The measurement was done on a RF5301 PC fluorometer (Shimadzu, Japan), with polarization filters (Polaroid) in cross-orientation in order to decrease light scattering. Excitation was set at 495 nm (5 nm slit width) and emission at 576 nm (10 nm slit width).

3.5 Preparation of liposomes and assay of their internal acidification

20 mg of L-α-phosphatidylcholine (99%) was dried under nitrogen and stored under vacuum overnight. Dried lipids were mixed with 1 ml of internal medium, containing 50 mM K-TES, 80 mM K_2SO_4, 2 mM K-EDTA, pH 7.2, and they were vortexed and sonicated to clarity. Octylpentaoxyethylene (40 mg, Bachem) and 6-methoxy-N-(3-sulfopropyl) quinolinium (SPQ, 2 mM) were added and the mixture was incubated with Bio-Beads SM-2 (Bio-Rad) to remove detergent and to form unilamellar vesicles. The external SPQ was removed by passage through spin columns of Sephadex G-50 coarse (Amersham), pre-equilibrated with the assay medium, which was identical to the internal medium. Increases in intraliposomal $[H^+]$ were obtained from increasing SPQ fluorescence due to diminished quenching by TES^- anion.

3.6 *E. coli* expression of UCP2

Bacterial strain BL21(DE3) (Novagen) containing plasmid pET21a with cDNA coding sequence for human UCP2 open reading frame inserted between the *Nde1* and *Not1* sites of the vector (Novagen) were donated by Dr. R. E. Gimeno and Louis A. Tartaglia (Millennium Pharmaceuticals, Inc., Cambridge, MA). Transformed cells were grown in the presence of carbenicillin (0.1 mg/ml) at 37 °C until A_{600} reached 0.3-0.4. The expression of UCP2 was induced with 1 mM isopropyl-β-D-thiogalactopyranoside and it was incubated at 30 °C for 3 h. Cells from a 700-ml culture were lysed in a French press (Fisher Sci.) in 20 ml of lysis buffer (10 mM Tris, 1 mM EDTA, 1 mM 1,4-dithiothreitol (DTT), pH 7). The lysate was centrifuged at 27,000 × g for 15 min. The pellet was resuspended in 20 ml of lysis buffer and centrifuged at 1,000 × g for 3 min. 1 ml-aliquots of the supernatant were centrifuged at 14,000 × g for 15 min. The resulting pelleted inclusion bodies were stored frozen at -80 °C.

3.7 Extraction of UCP2 from inclusion bodies

Each pelleted aliquot of inclusion bodies (roughly 2 mg of protein) was washed by gentle pipetting in 1 ml of phosphate buffer (150 mM Na_2HPO_4, 25 mM EDTA, 10 mM DTT, 2 mM phenylmethanesulfonyl fluoride (PMSF), 5% ethyleneglycol, 2% Triton X-100, pH 7.9

adjusted at 25 $^{\circ}$C with NaOH) and centrifuged at 12,000 × g for 12 min. The pellet was washed and presolubilized by gentle pipetting in 1 ml of phosphate buffer without the Triton X-100, which was substituted by 100 μl of solubilization buffer (2% N-Lauroylsarcosine sodium salt (SLS), 100 mM Tris, 2 mM EDTA, 10% glycerol, pH 7.8 adjusted at 25 $^{\circ}$C with HCl) and centrifuged at 12,000 × g for 12 min. The pellet was solubilized by gentle pipetting in 1 ml of the solubilization buffer during 15 min incubation at room temperature. The protein extract was diluted 4-fold in a glass beaker by adding subsequent 0.5 ml-aliquots of Tris-EDTA buffer (TE buffer: 50 mM Tris, 0.2 mM EDTA, pH 7.2 adjusted at 25 $^{\circ}$C with HCl) every 15 minutes at room temperature. To remove unsolubilized particles, the diluted protein extract was centrifuged at 12,000 × g for 12 min. The supernatant was further diluted 2.5-fold in a glass beaker by adding subsequent 0.5 ml-aliquots every 30 min, into the constantly-stirred solution, of TE buffer containing final concentrations of 1 mM DTT, 1 mM ATP and 0.1% nonaethylene glycol monodecyl ether ($C_{12}E_9$). The exchange of SLS for nonionic detergent $C_{12}E_9$ was completed by removing it in a three-step dialysis using a 14,000 MWCO membrane at 1:100 dilution - first overnight against TE buffer with 0.1% $C_{12}E_9$ containing 0.5 mM DTT, 0.5 mM ATP, 1 mg/ml BSA; second 6 h against TE buffer with 0.1% $C_{12}E_9$ containing 0.1 mM DTT, 1 mg/ml BSA; third overnight against TE buffer. To remove any precipitated protein, the collected retentate was centrifuged at 12,000 x g for 12 min. The protein was concentrated ~4-fold using the 10,000 MWCO Amicon Ultra-15 centrifugal filter device (Millipore) to gain final aliquots of ~1 mg/ml protein which were stored at -80 $^{\circ}$C. All above steps were carried at 4 $^{\circ}$C unless stated otherwise. The protein content was estimated according Lowry and Peterson with BSA as a standard [145].

3.8   EPR spectroscopy of spin-labeled fatty acids

EPR spectroscopy provides a powerful tool to study structure/function relationships in proteins [146-148]. EPR spectra were recorded on a Bruker Elexsys E580 EPR spectrometer operating in the X-band mode (9.7 GHz). The microwave power was set to 8 mW, receiver gain of 64 to 72 dB with modulation amplitude 1 G and 100 kHz field modulation frequency. Typically 60- or 30μl aliquots of solubilized UCP2 in $C_{12}E_9$ micelles were incubated 30 min with 4-fold excess of spin-labeled fatty acid. To study our protein system, we used 5- and 7-DOXYL stearic acid (DOXYL = 4,4-dimethyl-oxazolidine-N-oxyl) and 4-PROXYL palmitic acid (PROXYL = 2,2,5,5-tetramethyl-1-pyrrolidin-N-oxyl) – see Figure 7. The PROXYL group is less senzitive to degradation due to the lack of the DOXYL oxygen of the axazoline ring. The first one is commercially available from the company TCI Europe Ltd the second was a kind gift from Prof. Hideg, Hungary.

Prior the measurement, when applicable also an additional competing FA was added

together with the sample into quartz capillary, which was inserted into the resonator.

The EPR spectra were obtained by averaging two scans at 100 G magnetic field scan sweep width with a center field of 3452 G. The baseline has been subtracted from the recorded spectra. As a measure of molecular mobility the $2A_{zz}$ spectral parameters, defined as the separation between the outer hyperfine extremes, were evaluated from the triplet EPR spectra. Narrower width scans with double resolution were re-recorded for acquiring precise shapes of EPR spectra at the low field and high field regions.

EPR measurements have been carried out at Technische Universität Kaiserslautern.
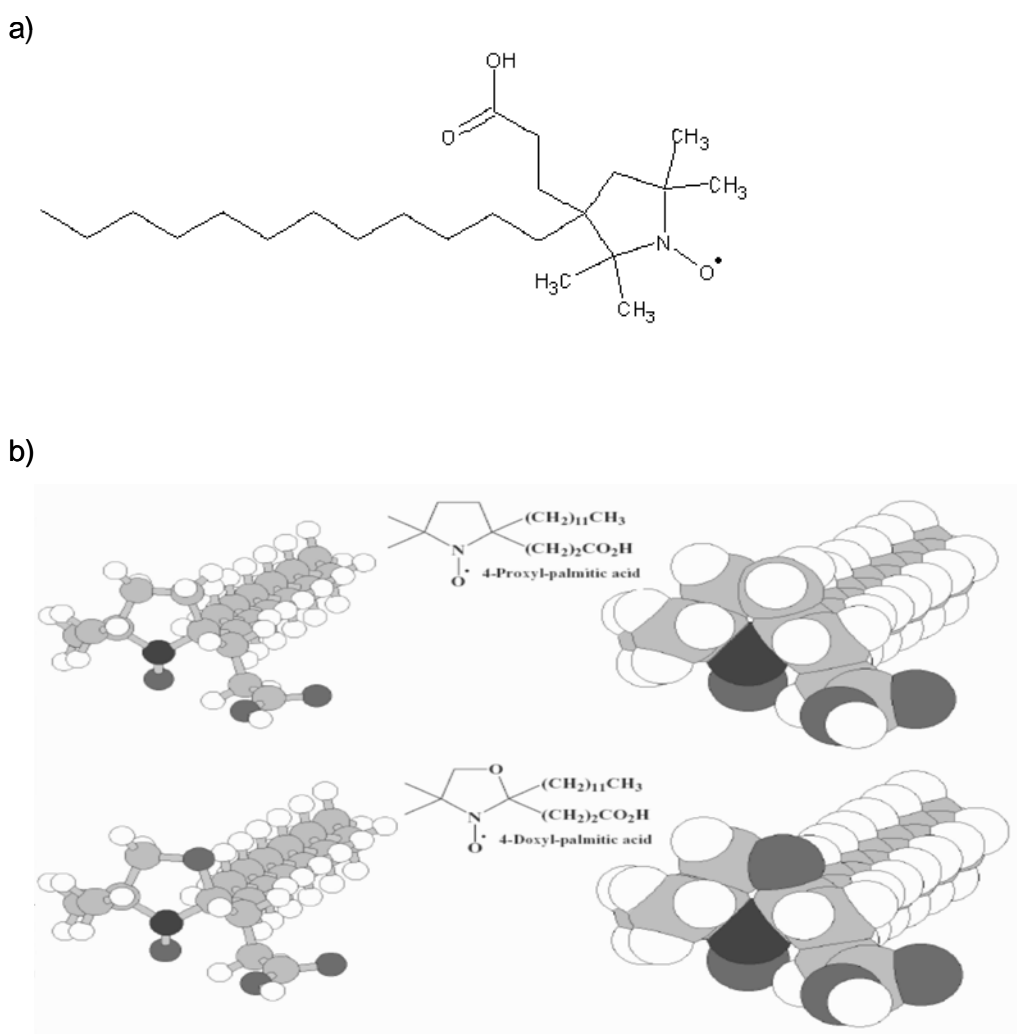
Figure 7 Chemical formulas of PROXYL- and DOXYL-fatty acid spin labels

For simplicity, 4-PROXYL- and 4-DOXYL-palmitic acids are compared, showing the same orientation of their nitroxides toward the fatty acid alkyl chains.
a) skeletal formula of 4-PROXYL palmitic acid
b) calotte models of 4-PROXYL and 4-DOXYL palmitic acid with the detail of PROXYL and DOXYL ring

3.9　Cell cultivation

INS-1E cell line was a kind gift of Prof. Pierre Maechler, University of Geneva. This cell line was derived from rat insulinoma INS-1 cells. These parental cells due to their nonclonal nature are not stable over extended culture periods in terms of insulin secretion. Clonal INS-1E cells were isolated based on their insulin content and their secretory responses to glucose. Therefore, INS-1E cells represent a stable β-cell model [283].

For experiments passages between No. 70 to 90 were taken. The cells were routinely cultivated in RPMI medium 1640 supplemented with 5% fetal calf serum (FCS; Biochrom), 10 mM 4-(2-hydroxyethyl)-1-piperazineethanesulfonate (HEPES; PAA), 2 mM L-glutamine, 1 mM Na pyruvate, 50 μM mercaptoethanol, 100 U/ml of Penicillin, and 100 μg/ml Streptomycin (both PAA). Cells were cultured at 37°C and 5% CO_2 in humidified atmosfere.

Two days before measurement cells were seeded on 6-well test plates (~1.7 million cells per well) and cultivated in RPMI medium. INS-1E cells were either assayed in the cultivation medium or were pretreated in order to deplete glucose (starve the cells). The standard pretreatment was performed as follows. After a variable time interval, which was optimized to one hour before the assay (see chap.), cells were prewashed by modified Krebs-Ringer-bicarbonate-HEPES medium (KRBH: 115 mM NaCl; 5 mM KCl; 2.2 mM $MgCl_2$; 2.5 mM $CaCl_2$; 24 mM $NaHCO_3$; 20 mM HEPES; 0.5% bovine serum albumine, BSA; pH 7.4). The assay was conducted in the KRBH without BSA at 37 °C after washing off the cells with 2 ml of KRBH. Generally, the cell viability after any treatment was controlled by returning cells to RPMI medium to check their ability of further growing.

3.10　Langerhans islet isolation

Wistar rats (Anlab or Charles River Lab.) and Goto Kakizaki rats (Taconic) were bred, housed, and sacrificed in accordance with the European Guidelines on Laboratory Animal Care and according to the Institute of Clinical and Experimental Medicine licensing committee approval. 36 week old male rats were taken for this work.

Goto Kakizaki rats were derived by embryo transfer from Danish (Aarhus) colony established in 1994 from the original Tohoku University (Japan) colony initiated in 1975. 4Pi microscopic images were done with islet samples isolated always from two Goto Kakizaki rats, weighing over 400 g and exhibiting hyperglycemia and crimpled intravenous glucose tolerance test (IGTT; ~20 mM glucose remained 60 min after glucose intake). Wistar rats were normo-glycemic and their IGTT had non-diabetic profile.

Langerhans islet isolation was performed according to a standard protocol by colleagues from IKEM [284]. Rats were anesthetized by intramuscular injection of Narketan (50 mg/kg;

Chassot GmbH) and Domitor (0.25 mg/kg; Orion Pharma). Under general anesthesia the abdomen was opened and rats were bled by cutting through of abdominal aorta. The common bile duct was cannulated and the pancreases were distended by an infusion of 15 ml collagenase solution (1 mg/ml; Sevapharma) in Hank´s balanced salt solution (HBSS; Sigma). The pancreases were excised, incubated and shook at 37°C for 20 minutes. The digest was washed 3 times with Hanks balanced salt solution (HBSS; Sigma) to deactivate and dilute collagenase. Islets were then separated from exocrine tissue by centrifugation over a discontinuous Ficoll gradient.

Purified islets were cultivated in RPMI 1640 medium without glucose (Gibco) supplemented with 10% FCS, 10 mM HEPES, 5 mM glucose, 2 mM L-glutamine, 1 mM Na pyruvate, 50 μM mercaptoethanol, 100 U/ml of Penicillin, and 100 μg/ml Streptomycin in a humidified CO_2 incubator at 37 °C and 5% CO_2 atmosphere. Islet viability was checked by propidium iodide and acridine orange staining.

3.11   Measurements of *in situ* mitochondrial membrane potential of INS-1E cells

In situ $\Delta\Psi_m$ was monitored by tetramethylrhodamine ethyl ester (TMRE) fluorescent probe (Molecular Probes) on a Fluorolog 322 fluorometer (Spex-Jobin-Yvon-Horiba). Excitation was set at 546 nm (slit width 10 nm) and emission at 574 nm (slit width 10 nm). 10 nM TMRE was added to the medium during the pretreatment for 15 min.

Alternatively, we employed fluorescent probe JC-1 (Molecular Probes), a voltage sensitive dye [285] that also selectively enters mitochondria. When excited at 490 nm (slit with 5 nm), the dye will emit green fluorescence at low $\Delta\Psi_m\square$ or red fluorescence at high $\Delta\Psi_m$ originating from the formed aggregates. Thus, simultaneous recording of emission signals at 593 nm (slit width 5 nm) and 537 nm (slit width 5 nm) was performed and ratio of signal of 593 nm to 537 nm was used as an index of increasing $\Delta\Psi_m$. 1 μM JC-1 was added to the medium during the pretreatment for 15 min.

3.12   Measurements of INS-1E cell respiration

Cell respiration was measured on Oxygraph 2k (Oroboros) which is equipped with two polarografic sensors with gold catodes and silver anodes. 1 M KCl solution is used as an electrolyte. Respiration is measured in a glassy chamber which is sterilized with 70% ethanol for 30 min before every measurement. The chamber is calibrated for 2 ml volume. Setting of the Oxygraph was as follows: polarization voltage 800 mV, gain 4 and stirrer speed 750 RPM.

Prior to the assay air calibration and background correction were performed.

3.13   Assay of total cell ATP/ADP ratio

After 60 min of glucose depletion, cells were not detached but were incubated with various concentrations of glucose and with or without 10 μM linoleic acid for 15 min at 37 °C. A Luciferase ATP assay kit (Roche) was employed after terminating incubations by boiling as suggested by the manufacturer. A half of the sample was used to convert ADP to ATP by pyruvate kinase reaction with phosphoenolpyruvate. Chemiluminescence of samples at 557 nm was quantified on a Fluorolog 322 fluorometer with switched-off excitation. ADP amounts were obtained by subtracting the ATP amounts from the total ADP + ATP amounts. Calibrations were performed separately for cell-free samples with and without pyruvate kinase.

3.14   Insulin secretion

Cells were seeded on poly-L-lysine coated 24-well plates at a density of 0.5×10^6 cells per well. After 60 min of glucose depletion, cells were not detached. GSIS was determined by static incubations. Secreted insulin was collected for 10 or 15min after glucose addition to glucose-depleted cells in 1ml of KRBH. Samples were then centrifuged at $500 \times g$ for 5 min to prevent contamination of cytoplasmic insulin and supernatants were immediately frozen in liquid nitrogen. The amount of released insulin was determined by RIA kit (ICN Radiochemical) using human insulin (part of the kit) as a standard.

3.15   Fusion protein constructs

The vector for mitochondrial addressing peptide (MAP)-conjugated redox-sensitive GFP (mRoGFP, a modified EGFP vector) was a kind gift of Dr. Rossignol, Univ. Bordeaux, France. The mRoGFP sequence was inserted into the Viral Power system vector, the pLenti 6.3/V5-DEST vector (Invitrogen), while ligated by T4 DNA ligase (USB). Lentiviral particles were isolated as described below.

3.16   Lentiviral particle production

The pLenti 6.3/V5-DEST-based construct have been multiplied, purified (QIA filter plasmid Maxiprep kit - Qiagen) and used for lentiviral particle production according to the manufacturer's (Invitrogen) instructions. Thus the lentiviral stock (containing the packaged pLenti expression construct) was produced by co-transfecting the optimized packaging plasmid mix (packaging plasmids pLP1, pLP2, and pLP/VSVG, which supplies the helper functions as well as structural and replication proteins required to produce the lentiviruses) and our expression constructs into the 293LTV cell line (Cell Biolabs). This cell line is stably and constitutively expressing the SV40 large T antigen facilitating an optimal lentivirus production.

Lipofectamine 2000 (Invitrogen) was used as the transfection reagent. The lentiviral stock was filtered and concentrated by PEG-it Virus Precipitation Solution (SBI) or using its separation by ultracentrifugation. Before proceeding to transduction and expression experiments, the titer of the lentiviral stock was determined, using fluorescence-activated cell sorting (Becton Dickinson LSR II).

3.17   Preparation of samples for 4Pi microscopy

INS-1E cells and Langerhans islets were cultured for 2 – 4 days on 4Pi quartz coverslips coated with poly-L-lysine. Islets had to be anchored onto the support, by letting the contaminating fibroblasts to attach to poly-L-lysine. The samples were then fixed with 4% paraformaldehyde and 0.025% glutaraldehyde (both Electron Microscopy Sci.) for 60 min at 25 °C. The unreacted aldehydes were reduced by 1 mg/ml sodium borohydride (pH 8; Sigma)) three times for 15 min. Finally, the coverslips were washed three times in PBS. The coverslips with fixed and immunostained islets (see below) were mounted in the 4Pi sample holders using 87.5% glycerol/PBS mounting medium with a refractive index of 1.460. Previous studies of mitochondria imaged with 4Pi microscopy have shown no morphological changes induced by this embedding [238]. The coverslip was then sealed to the sample holder using a two-component silicone glue Twinsil (Picodent). A conventional confocal microscope (Leica TSC SP2, equipped with a PL APO 100×/1.4–0.7 oil immersion objective) was employed for quality control during sample preparation.

3.18   Identification of β-cells within the Langerhans islets

Immunohistochemical staining against β-cell specific GLUT2 as a surface antigen has been performed to distinguish β-cells in Langerhans islet. Fixed islets were three times washed with phosphate buffer saline (PBS) and blocked with 5% donkey serum (Jackson Immunoresearch), 0.1 M glycine, 0.05% Tween 20 in PBS. Samples were incubated with rabbit anti-GLUT2 antibodies (1:200; Jackson Immunoresearch) in the blocking solution at 4 °C overnight. After 3-times washing in PBS containing 0.1 M glycine and 0.05% Tween 20, secondary Alexa 555-conjugated donkey anti-rabbit IgG antibodies (Invitrogen) were incubated with samples for two hours at room temperature. Final washing was done three times by PBS.

3.19   4Pi microscopy

Data were collected with a Leica TCS 4Pi microscope set up to operate in Type C mode, equipped with a pair of 100×/1.35 NA glycerol immersion objectives. mRoGFP fluorescence was recorded using two-photon excitation at 906 nm wavelength (Chameleon laser, Coherent Laser Group) and photon counting avalanche photodiodes. A short pass SP700 filter followed

by 525/50 (Chroma Technology Corp.) band pass filter was used in the detection path. The pinhole was set to 1 "Airy unit" while the beam expander was set to 3. The objective correction collars, focus alignment, and the interference phase of the microscope were adjusted for each individual sample. The embedding medium, in this case 87.5% glycerol/PBS with a refractive index of 1.460, was also used as the immersion medium to ensure continuity in the refractive index from objective to objective. Stacks of xz-images were recorded with a y-distance between neighboring slices of 31 nm. The pixel size in each xz image was chosen between 31 nm×31 nm for control β-cells and 45 nm×45 nm for diabetic β-cells. Stack dimensions were adapted to the cell size and were 15–24 μm×10–14 μm×12 μm for control β-cells and 24 μm×24 μm×12 –17 μm for diabetic β-cells. In data post-processing, each stack was smoothed and 3-point deconvolved with the LCS software (Leica Microsystems).

3.20   3D image analysis

3D projections were created with Amira 5.2.2 software (Visage Imaging). Several 3D projection methods were used. First, Voltex plots were inspected, illustrating the representation of the 3D data ensemble after 3-point deconvolution. The most frequently used 3D projections in an iso-surface mode had to be optimized in order to avoid inclusion of noise on one hand and not cutting too much signal on the other hand by proper setting thresholds. The intensity threshold (I_T) should be adjusted to rather low values, but high enough to avoid a "rough" surface appearance of mitochondrial tubules with small blebs originating from included background. It must be point out that the resulting objects are not representing the ~100 nm resolution of the microscope anymore but are optimized for visualization of the tubular network and its connectivity. Varying I_T from 10 to *e.g.* 90 shows a characteristic artificial disintegration of the mitochondrial tubules. Setting the I_T to 90 means that only intensities of 90 and above (maximum 255) are taken into the account. Background noise automatically vanishes, but dim signal is also excluded. Analysis of proper I_T values is thus very important for judging the connectivity of mitochondrial network. Additionally, another 3D display has been utilized, using the "Autoskeleton" module of Amira 5.2.2. software package. This method provides another representation of disconnected parts of the network and transfers signal intensities into diameters of representative cylinders. Alternatively, color-coding of separate objects was employed to count the numbers of each object types in 3D projections made using Paraview (Sandia Corporation), while varying I_T values. Volume of the network was taken as the number of voxels above I_T. By multiplying this number with the volume of a single voxel, an estimate for the volume of the tubular system can be generated. The "Autoskeleton" module has been used to sort the individual fragments and calculate their volumes.

The diameters of tubules and other objects were either calculated by an "interferometric"

or a "ruler" method. The interferometric method employed analysis of minima and maxima of the axial intensity profile [237] through at least ten objects which were confirmed as tubules, e.g. they were present in several subsequent frames of a data stack. Objects with extremely large diameters are excluded by this method as they do not provide a proper point-spread function. The ruler method simply measured at least 70 diameters using profile quantification tool of the Leica software on the raw xz data stacks. Also in this case larger objects potentially representing rings, large cisternae, or spheres were excluded from this analysis.

4 RESULTS

The traces and spectra shown in this chapter are representative of three or more independent experiments.

## 4.1 Testing whether alkylsulfonates are able to activate UCP1

Even after more than 30 years of intensive studies of UCP1, the molecular mechanism of its protonophoretic activity is still a matter of debate. The earliest experiments on the bioenergetic properties of BAT mitochondria revealed an unusual permeability to halide anions that could be inhibited by purine nucleotides [286]. Later it was shown that UCP1 could catalyze the translocation of wide variety of anions [42], including fatty acid anions and alkylsulfonates.

There exist three fundamentally different models regarding the mechanism and the role of FAs in uncoupling mentioned in chap. 2.2.1. Rial *et al.* [59] impeached the fatty acid cycling mechanism on the basis of their observation that undecanesulfonate caused increase BAT mitochondria respiration under conditions identical to those required for the activation by fatty acids. Since liposome studies have shown that alkylsulfonates cannot flip-flop across the membrane [46], this result would imply that the fatty acid cycling mechanism cannot be the underlying transport mechanism of UCP1. We tried to verify their observations.

4.1.1 Effect of undecanesulfonate on BAT mitochondria respiration

First, we have re-evaluated experiments reported by Rial *et al.* [59], studying effects of $C_{11}SO_3^-$ in the presence of 0.66 mg BSA ml^{-1}, in order to access an extent of putative uncoupling (Figure 8 a). BAT mitochondria depleted of endogenous FAs by preceding a carnitine cycle were supplemented after 5 min with pyruvate and malate which re-stored respiration to rates listed in the Table 1 (page 51). Addition of 200 μM $C_{11}SO_3^-$ to the respiratory medium with BSA 0.66 $mg.ml^{-1}$ accelerated respiration by 1.8 fold (Figure 8 a) or 2-fold for malate and citrate. With increasing or decreasing BSA these ratios were even higher or lower, respectively (Table 1). In the absence of BSA, respiration was faster, but 200 μM $C_{11}SO_3^-$ increased it only ~1.2- fold (Figure 8 b, the left trace). One can clearly recognize this slight acceleration of respiration, when compared to the respiration which was allowed to proceed without the $C_{11}SO_3^-$ addition (Figure 8 b, the right trace). This effect might be

interpreted as a mild uncoupling. However, it has much greater extent in the presence of BSA, as derived from the surplus of respiration, caused by $C_{11}SO_3^-$, which was significantly higher with BSA than without BSA (Table 1). This can be due to a release of residual FAs bound on BSA upon $C_{11}SO_3^-$ addition (see below). The released FAs normally function as cycling substrates of UCP1 and thus uncouple BAT mitochondria.
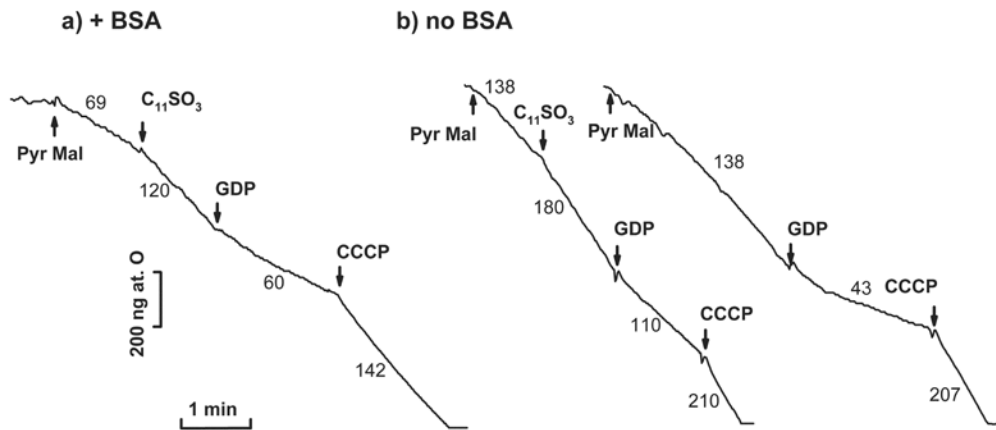
Figure 8 Undecanesulfonate effect on respiration of BAT mitochondria

a) in the presence of BSA (0.66 mg.ml^{-1})
b) in the absence of BSA
BAT mitochondria were depleted of endogenous fatty acids using the carnitine cycle ongoing for 5 min (this part of the traces is omitted) and after the slow down of respiration due to nearly complete combustion of endogenous FAs, 5 mM Tris-pyruvate and 5 mM Tris-malate were added. 200 μM undecanesulfonate ($C_{11}SO_3^-$) was added as indicated by arrows, followed by the additions of 1 mM Tris-GDP. The right trace in (**b**) was measured without $C_{11}SO_3^-$ addition for comparison. At the end of each run, 1 μM CCCP was added. The numbers at the traces indicate respiration rates in ng atoms O min^{-1}mg protein^{-1}.

Another aspect of undecanesulfonate effect in BAT mitochondria can be seen in the decrease of purine nucleotide affinity to UCP1 in its presence, as has already been described elsewhere ([287]). This effect could contribute to the observations in our experiments. Indeed, GDP (1 mM) inhibited respiration most strongly when no $C_{11}SO^{3-}$ was added (Figure 8 b, the right trace), slightly less with BSA plus $C_{11}SO^{3-}$ (Figure 8 a), and its lowest inhibitory effect was observed after addition of $C_{11}SO^{3-}$ without BSA (Figure 8 b, the left trace). Note, we do not compare to zero nucleotide levels, since 0.2 mM ATP was always present due to induction of the carnitine cycle.

4.1.2   Effect of undecanesulfonate on membrane potential of BAT mitochondria

To investigate that a release of residual FAs bound on BSA upon $C_{11}SO_3^-$ addition is a probable cause of a part of the observable slight uncoupling in BAT mitochondria, we monitored membrane potential with Safranine (Figure 9) during the course of the experiment, such as described in Figure 8. Upon $C_{11}SO_3^-$ addition in the presence of 0.1 or 0.66 mg.ml^{-1} BSA from the beginning (Figure 9 panel A, the upper and the lower trace, respectively), mitochondrial membrane potential ($\Delta\Psi_m$) dropped, further addition of GDP restored it to a high value, and FCCP reduced it again. The GDP re-coupling effect was slightly higher with higher BSA concentration. However, without BSA, $C_{11}SO_3^-$ did not cause any $\Delta\Psi_m$ decrease and GDP increased it to a high value, which was collapsed by FCCP (Figure 9 panel B, the upper trace). Moreover, no undecanesulfonate-induced $\Delta\Psi_m$ decrease was observed when BSA was added after the carnitine cycle, so that BSA could not absorb endogenous FAs (not shown). Actually, with GDP a higher $\Delta\Psi_m$ was reached in the presence of $C_{11}SO_3^-$ than in its absence (Figure 9 panel B). When $C_{11}SO_3^-$ does not decrease $\Delta\Psi_m$ and slightly enhances respiration, the effect is not uncoupling by definition. This is what happens without added BSA.

Figure 9 Undecanesulfonate effects on membrane potential of BAT mitochondria

a) in the presence of BSA (0.1 and 0.66 mg.ml^{-1} in the upper and the lower trace, respectively)
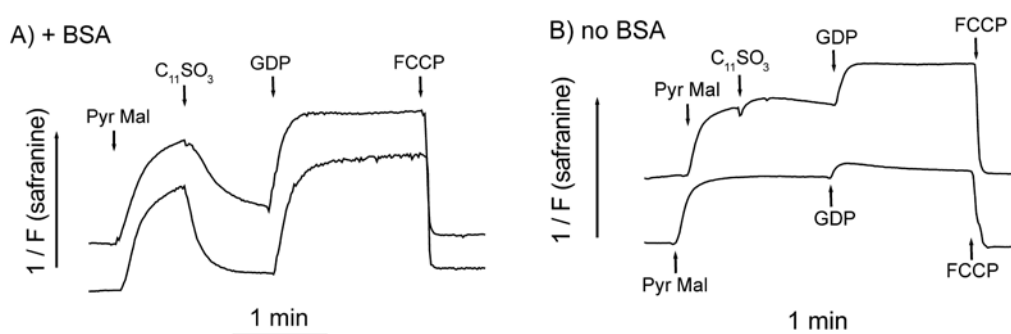**b**) in the absence of BSA
BAT mitochondria were depleted of endogenous fatty acids using the carnitine cycle ongoing for 5 min as described in Methods (this part of the traces is omitted) and 5 mM Tris-pyruvate with 5 mM Tris-malate were added. 200 μM undecanesulfonate ($C_{11}SO_3^-$) was added as indicated by arrows, followed by the additions of 1 mM GDP. For comparison, the lower trace in (**b**) was measured without $C_{11}SO_3^-$ addition. The traces are offset for clarity. At the end of each run, 1 μM FCCP was added.

4.1.3   Effect of undecanesulfonate on rat heart mitochondria respiration

To investigate a slight $C_{11}SO_3^-$-induced acceleration of respiration in the absence of BSA and to judge, whether this effect is independent of UCP1, we have studied it further in rat heart

mitochondria. We were able to induce the carnitine cycle in heart mitochondria. After the cycle had run for 5 min, oligomycin was added, which converted heart mitochondria into a highly coupled state. As in BAT mitochondria, the addition of $C_{11}SO_3^-$ slightly accelerated the coupled respiration, but equally in the presence or absence of BSA (Figure 10 a, Table 1 page 51). When 5 μM lauric acid was added to simulate similar endogenous FA levels in heart mitochondria as in hamster BAT mitochondria, and oligomycin was omitted, to allow a high H^+ leak due to the F_O ATPase, the rate of respiration was much higher than at state 4. Without further substrate added, respiration was dependent on the addition of CoA, carnitine (and 0.2 mM ATP) and hence represented ongoing β-oxidation of the added lauric acid (not shown). Addition of pyruvate and malate (Figure 10 b) further increased the respiration rate, and addition of 200 μM $C_{11}SO_3^-$ lead to the same slight (~1.25 fold) accelerating effect on respiration as in the case of BAT mitochondria. When BSA was present (together with 5 μM lauric acid), addition of 200 μM $C_{11}SO_3^-$ led to the same small accelerating effect as in the absence of BSA (Figure 10 b, the right trace).
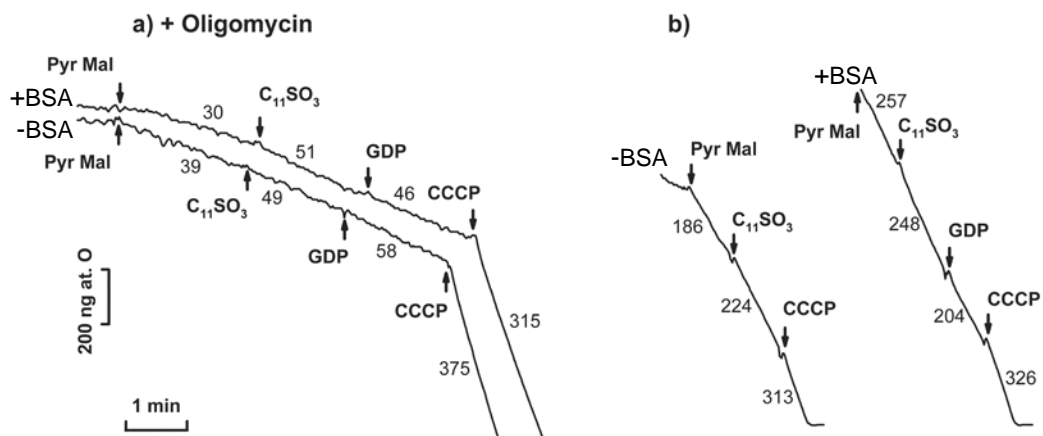
Figure 10 Undecanesulfonate effect on respiration of rat heart mitochondria

a) in the presence of 1 μg oligomycin per ml (state 4 respiration)
b) in the absence of oligomycin but with 5 μM lauric acid added prior to the initiation of the carnitine cycle. The cycle (as described in Methods) was ongoing for 5 min prior to substrate addition (this part of the traces is omitted). After this period, 5 mM Tris-pyruvate and 5 mM Tris-malate were added. Right traces in both panels, a) and b), were measured in the presence of 0.66 mg.ml^{-1} BSA from the beginning. When indicated by the arrows, 200 μM undecanesulfonate ($C_{11}SO_3^-$), 1 mM Tris-GDP, and 1 μM CCCP were added. The numbers at traces indicate respiration rates in ng atoms O min^{-1}mg protein^{-1}.

4.1.4   Effect of undecanesulfonate on fatty-acid-induced uncoupling in BAT mitochondria

To demonstrate that undecanesulfonate does not activate UCP1-mediated uncoupling, we further studied its possible potentiation of FA-induced uncoupling. If such a potentiation existed, one had to conclude that undecanesulfonate indeed induced uncoupling mediated by UCP1. However, we show that this is not the case.

We further studied lauric acid-induced uncoupling with or without addition of 200 μM $C_{11}SO_3^-$ (Figure 11). For this assay, citrate and malate were used as substrates, in order to avoid pyruvate cycling [44]. Moreover, at the end of 5 min ongoing carnitine cycle, oligomycin, CAT, and etomoxir were added, in order to exclude interferences by F_O ATPase, FA cycling on the ADP/ATP carrier, and contribution of β-oxidation to respiration, respectively. Without further additions, 2.5 μM lauric acid (Figure 11 a) accelerated respiration quite extensively, whereas 250 nM (Figure 11 b) with less extent. Thus 2.5 μM lauric acid uncoupled to a nearly maximum respiration rate such as observed under subsequent CCCP addition (Figure 11 a). With 250 nM lauric acid, 1 mM GDP was able to inhibit 63% of such accelerated respiration (Figure 11 b), indicating UCP1 participation. When 200 μM $C_{11}SO_3^-$ was added after lauric acid, respiration decreased by 13% and 16% in the case of 2.5 μM and 250 nM lauric acid, respectively, rather than increased. This clearly shows that $C_{11}SO_3^-$ does not contribute by an independent uncoupling effect as does an uncoupler (CCCP), added at the end of these experiments. $C_{11}SO_3^-$ does not potentiate already existing lower extent of uncoupling. This weak inhibitory effect of $C_{11}SO_3^-$ is consistent with its competition with lauric acid, partially preventing its cycling (transinhibition of laurate anion efflux by external $C_{11}SO_3^-$). When 200 μM $C_{11}SO_3^-$ was added prior to lauric acid (Figure 11 a, the right trace), it only accelerated respiration by 20% as reported above. Subsequent addition of 2.5 μM lauric acid led to more than 2-fold increase in respiration due to UCP1-mediated uncoupling as inferred from following GDP inhibition.

Moreover, when GDP was added from the beginning of the experiments during the carnitine cycle, 250 nM lauric acid accelerated respiration only 1.3 times (Figure 11 b) and subsequent addition of 200 μM $C_{11}SO_3^-$ did not increase respiration anymore. However, respiration was rather inhibited by GDP, which blocks the UCP1-mediated uncoupling, as clearly seen from the subsequent CCCP addition, which exhibited a real uncoupling reaching the maximum respiration rate. In conclusion, one can clearly distinguish a rather nonspecific effect of acceleration of respiration caused by $C_{11}SO_3^-$ from the real uncoupling effect of lauric acid. The lack of potentiation of submaximum lauric acid-induced uncoupling by $C_{11}SO_3^-$ shows that $C_{11}SO_3^-$ does not have the capability to induce uncoupling on UCP1 by either mechanims, allosteric, or cycling, or by any other model.
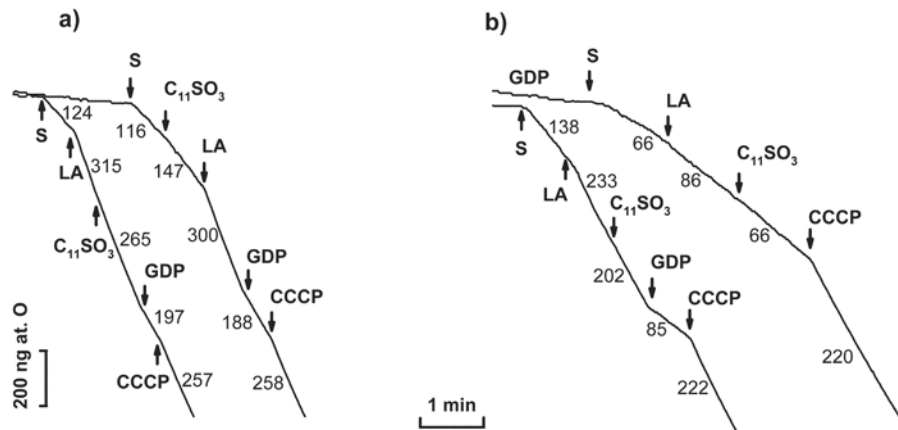
Figure 11 No potentiation by undecanesulfonate of lauric-acid-induced uncoupling of BAT mitochondria

a) 2.5 μM lauric acid
b) 250 nM lauric acid
BAT mitochondria were depleted of endogenous fatty acids using the carnitine cycle ongoing for 5 min as described in Methods (this part of the traces is omitted). After this period, 5 mM Tris-citrate & 5 mM Tris-malate were added together with 1 μg oligomycin per ml, 2.5 μM carboxyatractyloside, and 12.5 μM etomoxir (additions are indicated by "S"). For the right trace in b), also 1 mM Tris-GDP was present from the beginning. As indicated by arrows, lauric acid (LA), 200 μM undecanesulfonate ($C_{11}SO_3^-$), and 1 mM Tris-GDP were added. At the end of each run, 1 μM CCCP was added. Note that undecanesulfonate added after lauric acid (the left trace in (**a**), both traces in (**b**)) did not potentiate the uncoupling effect of either 2.5 μM or 250 nM lauric acid. In turn, the effect of a real uncoupler, CCCP, is clearly demonstrated at the end of each run. The numbers at traces indicate respiration rates in ng atoms O min^{-1}mg protein^{-1}.

Table 1 Effect of undecanesulfonate on BAT and rat heart mitochondria respiration

	Substrates	Ratio V_{C11}/V_{4inh} (1)	Ratio V_{C11}/V_{4inh} (1) with BSA 0.1 mg ml^{-1}	Ratio V_{C11}/V_{4inh} (1) with BSA 0.66 mg ml^{-1}	Ratio V_{C11}/V_{4inh} (1) with BSA 1.0 mg ml^{-1}	$V_{C11}-V_{4inh}$ (nmol O min^{-1} mg protein^{-1})	$V_{C11}-V_{4inh}$ (nmol O min^{-1} mg protein^{-1}) with BSA 0.66 mg ml^{-1}	V_4 (nmol O min^{-1} mg protein^{-1})	V_{4inh} (nmol O min^{-1} mg protein^{-1})	V_{CCCP} (nmol O min^{-1} mg protein^{-1})
BAT mito	Pyruvate and malate	1.24 ± 0.07	1.60 ± 0.07	1.80 ± 0.05	1.90 ± 0.02	19 ± 2	44 ± 10	65 ± 6	66 ± 6	115 ± 7
BAT mito	Citrate and malate	1.2 ± 0.1	1.60 ± 0.03	2.0 ± 0.1	2.40 ± 0.02	12 ± 5	38 ± 3	n.d.	59 ± 5	130 ± 4
Heart mito	Pyruvate and malate	1.23 ± 0.05	n.d.	1.3 ± 0.1	n.d.	11.4 ± 5.4	11.7 ± 2.5	167	40 ± 8	225 ± 37

Carnitine-cycle pretreated BAT mitochondria or rat heart mitochondria respiring with the indicated substrates exhibited "pseudo-state-4" rates "V_4" and "V_{4inh}" in the absence or presence of inhibitors, respectively, as indicated in the 8th and 9th column. Inhibitors were etomoxir (12.5 mM), oligomycin (1 μg/ml), and CAT (2.5 μM) for BAT mitochondria and oligomycin (1 μg/ml) for rat heart mitochondria. Accelerated respiration V_{C11} upon addition of 200 μM undecanesulfonate is expressed either as ratio or a difference to the preceding rates (mostly V_{4inh} or rates after β-oxidation of 5 μM lauric acid without oligomycin in rat heart mitochondria) in the absence or presence of BSA in concentrations as indicated. Uncoupled respiration by 1 μM FCCP is in the last column. Values are means ± SD (n

≥ 3)

4.1.5   *Effect of undecanesulfonate on reconstituted UCP1 in liposomes*

To further test the concept that $C_{11}SO_3^-$ displaces FAs from their binding site on BSA and the released FAs then serve as cycling substrates of UCP1, we have studied the effect of $C_{11}SO_3^-$ addition to liposomes suspended with or without FA-saturated BSA. The addition of $C_{11}SO_3^-$ then behaved as the addition of a small FA aliquot (Figure 12 a), causing acidification of liposome interior (flip-flop acidification). This acidification was insignificant when defatted BSA or no BSA was used (Figure 12 b).
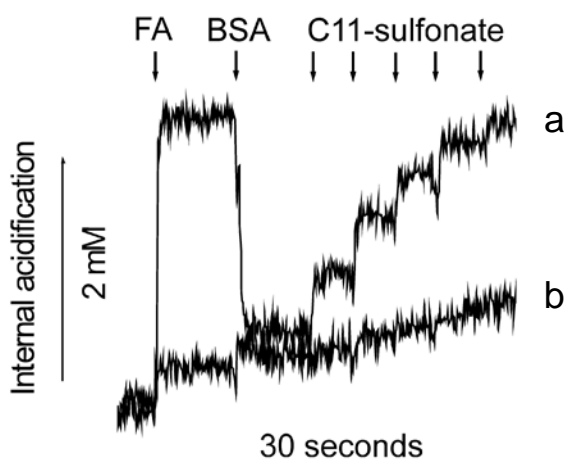
Figure 12 Addition of undecanesulfonate to fatty acid-saturated albumin causes acidification of liposome interior - as does addition of fatty acid itself.

Fluorescent traces indicate flip-flop acidification of liposomal interior due to fatty acid upon the addition of 50 µM lauric acid (100 nmol total, the trace **a**). Subsequent addition of 12.5 µM BSA (25 nmol) resulted in lumen alkalinization but not to the original level, consistent with the removal of membrane-embedded lauric acid. Step-wise additions of 50 µM (100 nmol) aliquots of undecanesulfonate resulted in gradual acidification steps, which were not observed in the absence of lauric acid (the trace **b**).

## 4.2 Functional characterization of mitochondrial UCP2 by EPR studies

Electron paramagnetic resonance (EPR), often called electron spin resonance (ESR), is used for the branch of spectroscopy that studies paramagnetic molecules, that is molecules with unpaired electrons. Biologically important paramagnetic species include free radicals and many transition elements. ESR sensitive reporter groups (spin labels or spin probes) can be also introduced artificially into biological systems, either through chemical modification of the bio-molecule or via spin-labeled substrates or cofactors. Spin labels can provide information on motion, both the motion of the spin label itself and of the molecule or molecular system to which it is bound. It can also provide information on the chemical nature of the environment of the site at which the label is bound because the method is highly sensitive conformational transitions within the viscinity of these reporter groups and therefore allows the evaluation of conformational/structural processes during substrate binding. ESR is of great significance for studies of membrane proteins where many other biophysical methods are relatively handicapped due to the specific characteristics of membrane biology, *e.g.*, ESR is unaffected by light scattering, and it can also be used at high viscosities of the samples. Furthermore, the relatively small size of the spin label usually does not significantly perturb the biological activity of the enzym or protein.

In this study, we used spin-labeled fatty acids, containing a stable nitroxide radical attached at different positions along the chain of fatty acid in order to elucidate, whether UCP2 binds FAs. These spin probes have been successfully used in previous studies and demonstrated the binding with UCP1 [67].

4.2.1 *Fatty acid interaction with UCP2*

The EPR binding studies were commenced with the isolated recombinant UCP2 (*E. coli*-expressed UCP2 refolded from inclusion bodies) and 4-PROXYL-palmitic acid (4-PSL-FA), chosen as the most convenient spin-labeled FA ligand. The reaction mixture regularly contained 142 μM 4-PSL-FA incubated with 35.5 μM UCP2 in ~10 mM $C_{12}E_9$ micelles. The spectrum of a certain spin-labeled fatty acid bound with protein clearly differs from that only in micelles without protein which can be shown by accurate determination of the $2A_{zz}$ parameter. Figure 13 shows the control EPR spectrum without any further additions of competing compound. The spectrum exhibits clearly separated peaks in the low-field and high-field regions respectively, the two peaks labeled in each region indicate the existence of more or less immobilized spin-labeled fatty acid. Correspondence to the h_{+II} peak of the immobilized spin probe, distinct from

the residual h_{+1M} peak of more freely tumbling species suggest that the former could reflect the population bound to the protein and the later in micelles. The bound regions of the spectrum were re-recorded at higher signal gain and aligned over the spectrum for better visualization. The parameters $2A_{zz}$ were, on average, 44.0 ± 0.2 Gauss (n = 3) and 33.2 ± 0.2 Gauss (n = 3) for the immobile and mobile peak, respectively. When the same UCP sample was precipitated with trichloracetic acid, the bound signal disappeared.
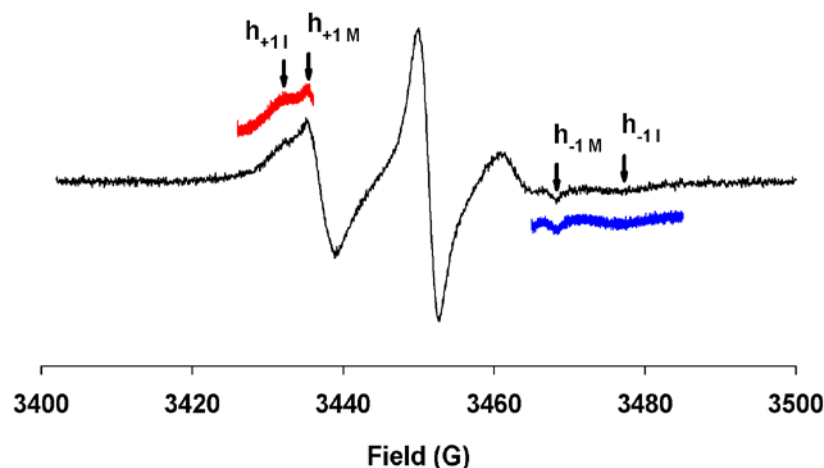
Figure 13 EPR spectrum of 4-PROXYL-palmitic acid bound to UCP2

The spectrum of 142 μM 4-PSL-FA incubated with 35.5 μM UCP2 in ~10 mM $C_{12}E_9$ micelles exhibited two clearly separated h_{+1I} immobile peak distinct from the highly reduced h_{+1M} mobile peak in the low field region as well as h_{-1I} immobile peak distinct from the reduced h_{-1M} mobile peak in the high field region. Parameters $2A_{zz}$ were 44.0 ± 0.2 Gauss (n = 3) and 33.2 ± 0.2 Gauss (n = 3) for the immobile and mobile peak, respectively.

The EPR spectra of 4-PROXYL-palmitic acid in the presence of UCP2 and competing fatty acids are displayed in Figure 14 - 16. When the concentrations of polyunsaturated all-*cis*-8,11,14-eicosatrienoic acid, C20:3(ω-6) (ETA) and arachidonic acid (AA), and palmitic acid were increased, the mobile peaks (h_M) were progressively rising while the immobile peaks (h_I) merged with the baseline signal intensity in both, low and high field regions, thus indicating competition for the FA binding site on UCP2. ETA apparently exhibits a higher affinity than AA, because a half maximum shift of the h_{-1M} peak can be estimated around 50 μM as compared to more than 90 μM for arachidonic acid. These are rough estimates of apparent K_d values for competing FAs.
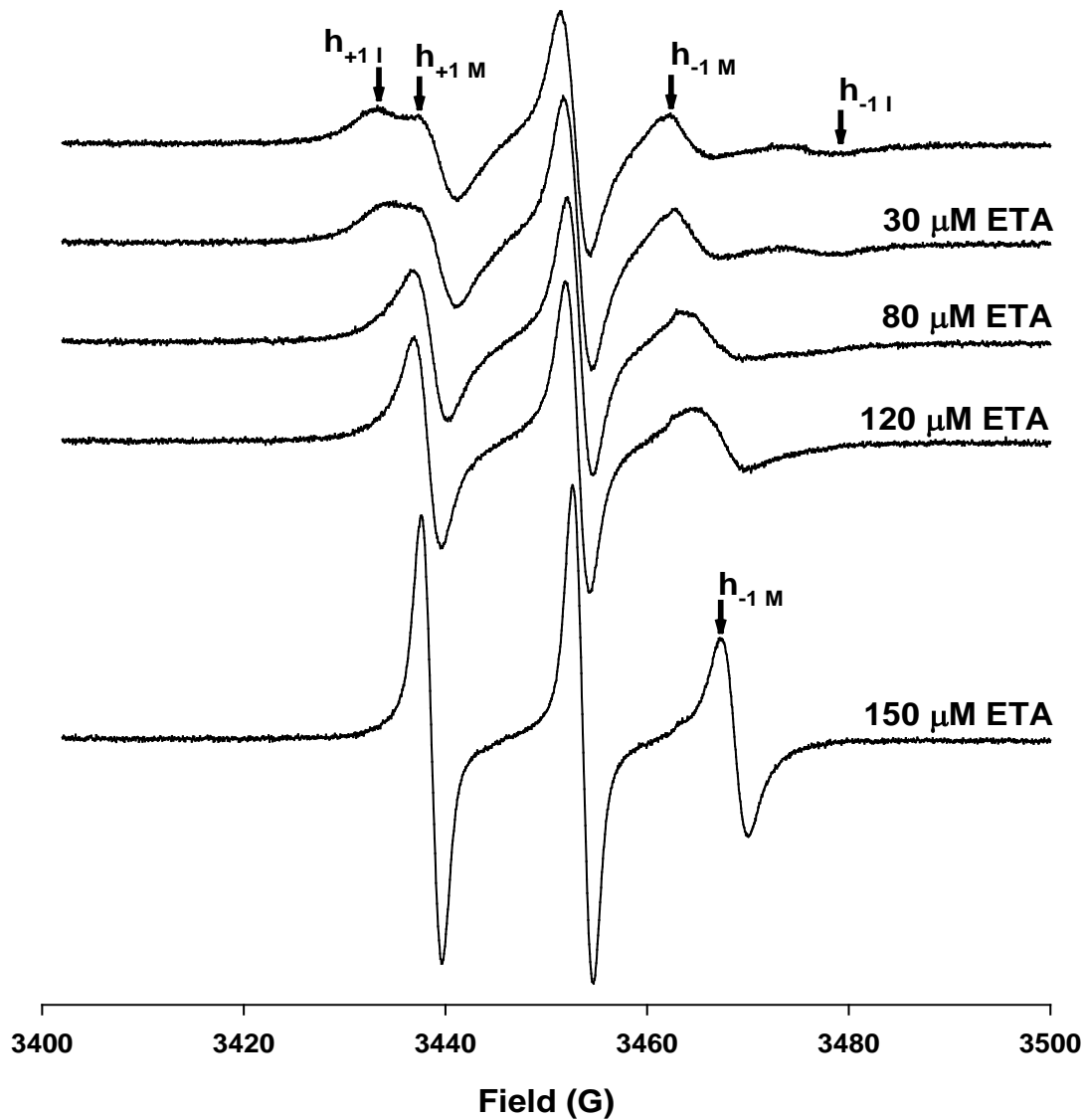
Figure 14 4-PROXYL-palmitic acid displacement from UCP2 binding site in the presence of competing 8,11,14-eicosatrienoic acid (ETA)

Increased concentrations of 8,11,14-eicosatrienoic acid (up to 150 μM), added to the micellar solution of 4-PSL-FA and UCP2 in $C_{12}E_9$, led to a gradual rise of both mobile peaks h_{+1M} and h_{-1M} in the low and high field region of the EPR spectrum, respectively. The half-maximum effect occurred around 50 μM ETA.
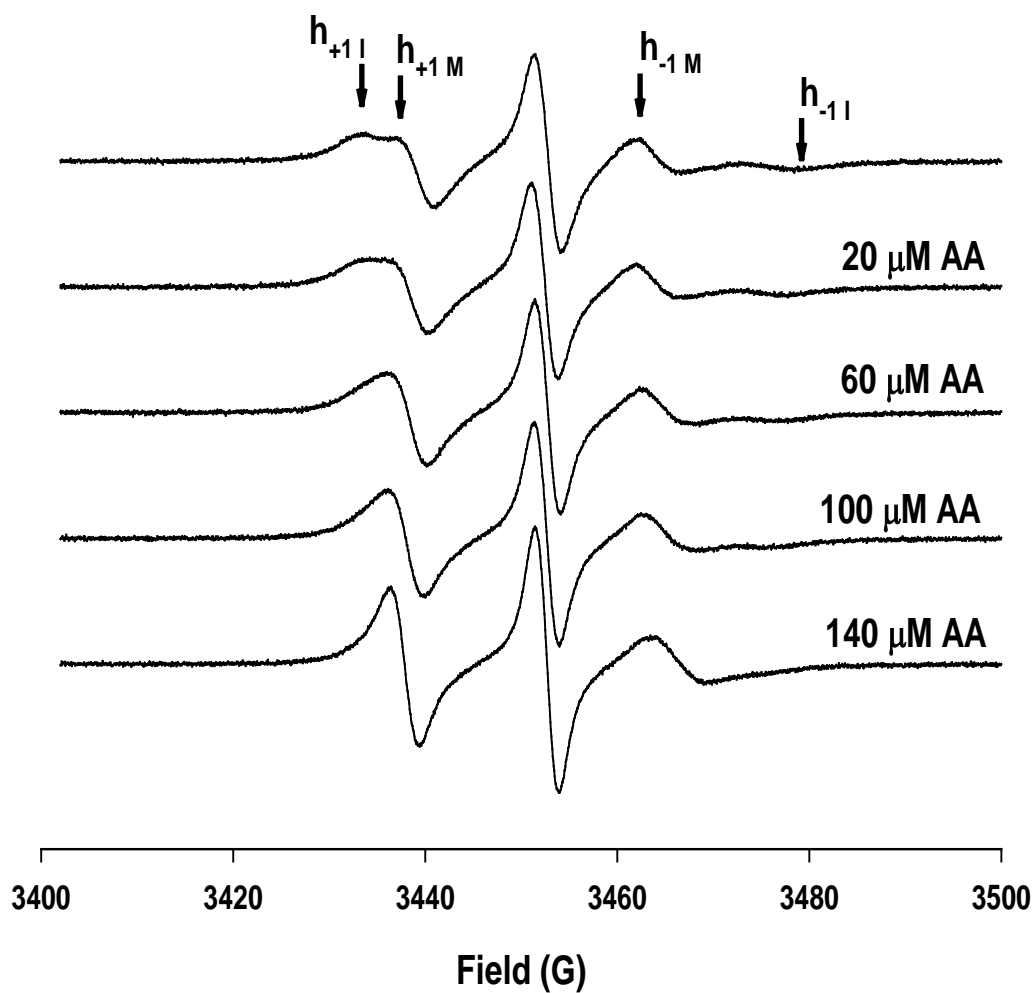
Figure 15 4-PROXYL-palmitic acid displacement from UCP2 binding site in the presence of competing arachidonic acid (AA)

Increased concentrations of arachidonic acid (only to 140 μM is shown), added to the micellar solution of 4-PSL-FA and UCP2 in $C_{12}E_9$, led to a gradual rise of both mobile peaks h_{+1M} and h_{-1M} in the low and high field region of the EPR spectrum, respectively. The half-maximum effect occurred above 90 μM AA.

Figure 16 4-PROXYL-palmitic acid displacement from UCP2 binding site in the presence of competing palmitic acid (PA).

Increased concentrations of palmitic acid (360 μM and 1 mM are shown) added to the micellar solution of 4-PSL-FA and UCP2 in $C_{12}E_9$, led to a rise of both mobile peaks h_{+1M} and h_{-1M} in the low and high field region of the EPR spectrum, respectively.

4.3 Basic bioenergetic parameters of INS-1E cells

4.3.1 *Respirometry of INS-1E cells in standard cultivation medium*
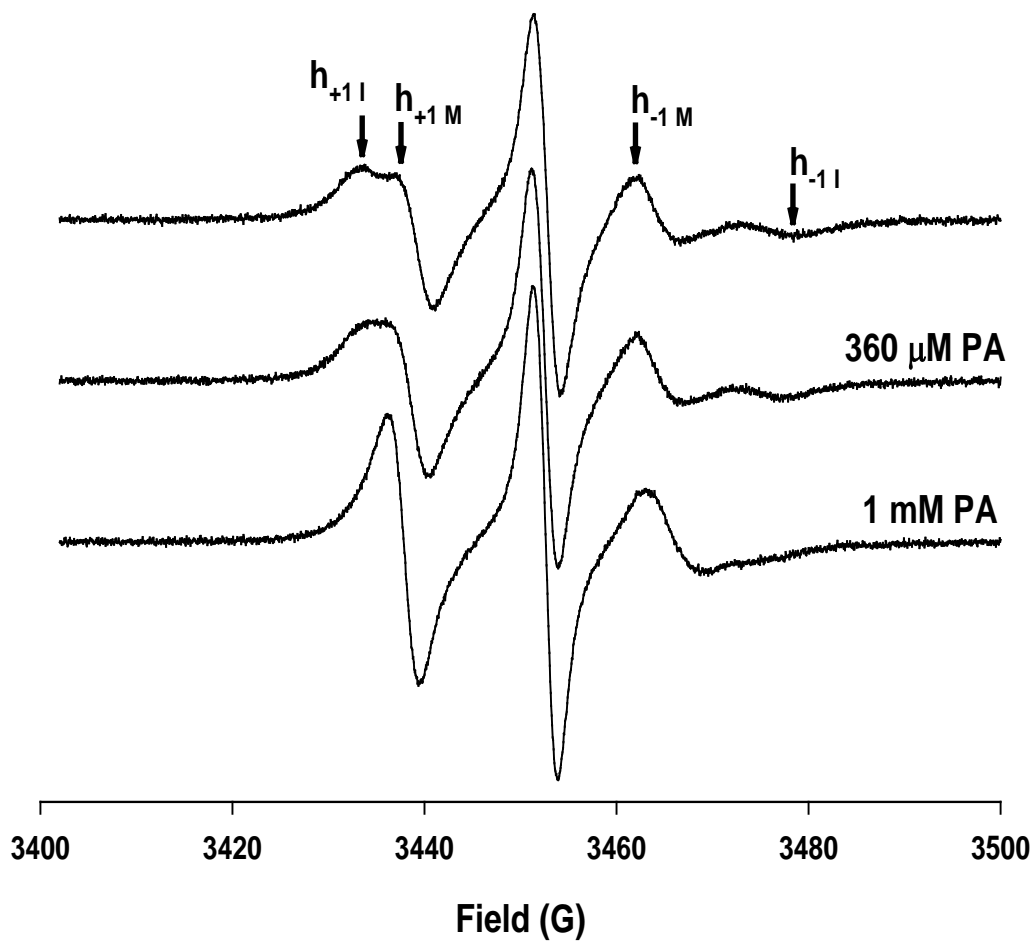
First, respiration of INS-1E cells at steady-state at which they are cultivated was ascertained. The established steady-state respiration in the own cultivation medium reached magnitude of 38 ± 4 pmol $O_2 \cdot s^{-1}$ per 10^6 cells (n=16) see (Figure 17). This respiration represents an endogenous, hence *in situ*, state 3 ($state_i3$), i.e. predominantly phosphorylating respiration. Addition of oligomycin, inhibitor of the H^+ flux via the F_O part of ATP synthase, converted it into a nonphosphorylating $state_i4$, which reached 42% of $state_i3$. Subsequent addition of an uncoupler, carbonyl cyanide p-(trifluoromethoxy)phenylhydrazone (FCCP), concomitantly revealed a maximum respiration capacity of 72 ± 8 pmol $O_2 \cdot s^{-1}$ per 10^6 cells (n=9). Addition of KCN or stigmatellin returned cell respiration to zero, clearly showing that the total cellular respiration originates from mitochondria. Calculated ratio $state_i3/state_i4$ 2.4 ± 0.2 (Table 2, page 62, the second column) is showing a rather highly coupled state of oxidative phosphorylation in INS-1E cells routinely cultivated at 11 mM glucose (amount of glucose in standard RPMI medium).
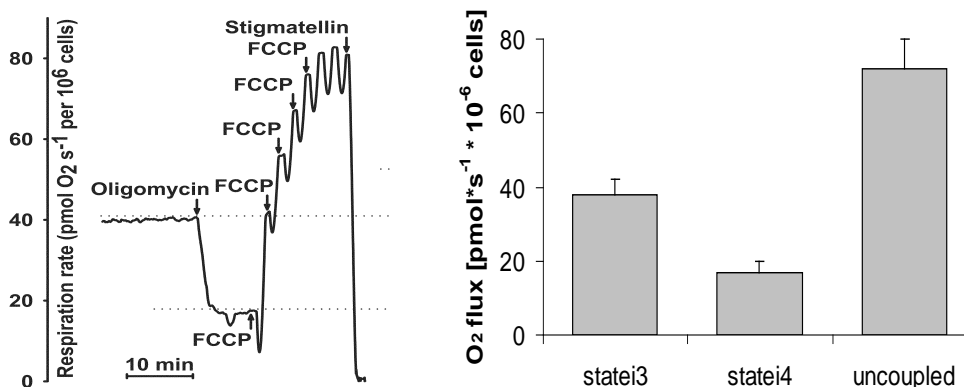
Figure 17 Basic bioenergetic parameters of INS-1E cells.

INS-1E cells cultivated and assayed in RPMI medium containing 11mM glucose were tested for basal ($state_i3$), endogenous ($state_i4$) (100 ng/ml oligomycin), uncoupled (3 μM FCCP) and finally inhibited respiration (0.5 μM stigmatellin)
The left part – record from Oxygraph
The right part – bar graph represents statistic of more than 10 runs, values are means $\pm$ SD

4.3.2 Establishing of glucose depletion of INS-1E cells

Since glucose and other substrates (pyruvate etc.) are routinely present in the cultivation medium, one cannot measure phenomena with an orthodox dependence on glucose. Thus GSIS assayed upon addition of further incremental glucose does not represent the total GSIS, which by definition should be derived towards zero glucose. Likewise insulin flux without any glucose addition does not represent a net basal exocytosis given by spontaneous granule release, but its mix with the already glucose-stimulated part. Additions of 5 to 20 mM glucose (final concentrations 16 to 31 mM) to the cells led only to marginal instant elevation in either respiration or $\Delta\Psi_m$. As demonstrated below, GSIS and its bioenergetic parameters are actually nearly saturated under these conditions.

In order to evaluate specific features of glucose-dependent bioenergetics of INS-1E cells with the regard to orthodox GSIS (related to zero glucose), a procedure of glucose depletion by incubations followed by washing in glucose-free KRBH medium was established. This procedure does not harm the cells as recognized by still high $state_i3/state_i4$ ratio 2.3 ± 0.2 recovered upon subsequent glucose addition. The cells reportedly survive this "starvation period" by β-oxidation of fatty acid stores [288]. We have adjusted time of pre-treatment in glucose-free medium according to the maximum respiration responses to the added glucose (Figure 18). Zero time incubation followed by an instant centrifugation in KRBH medium led to only 32% of maximum glucose-induced respiration jump. 10 min preincubation led already to a half-maximum effect, but we have chosen 60 min incubation in KRBH medium for routine assays, since responses to glucose were constant up to 120 min. Within the whole time course, 60 min incubations also led to maximum $state_i3/state_i4$ ratio after 20 mM glucose addition. The routine glucose-depletion (starvation) led to more than half decrease in respiration, which was restored, when cells were returned to the glucose-containing RPMI medium.
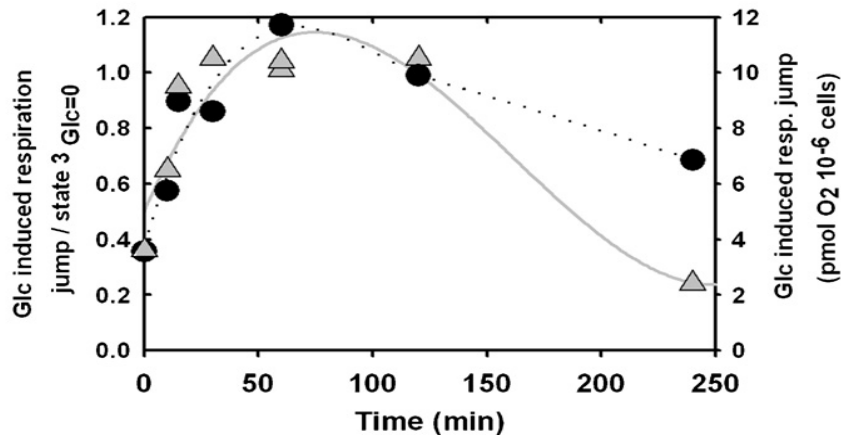
Figure 18 Time course of cell preincubations without glucose for respiratory jumps induced by 20 mM glucose addition related to state$_i$3 without glucose (left axis) or in absolute values (right axis). Data were fit by polynomials.

4.3.3 *Respiration and $\Delta\Psi_m$ measurement of glucose depleted INS-1E cells*

In contrast to the untreated cells, the glucose-depleted INS-1E cells, i.e. pretreated in KRBH medium, and assayed in this medium exhibited an increase in both respiration (Figure 19 a, b – the upper traces) and $\Delta\Psi_m$ (Figure 19 c-f – the upper traces) upon glucose addition. Addition of 20 mM glucose led to the highest elevations of respiration. The elevations were up to five times higher with regards to the additions of 6 mM glucose (Figure 19 b *vs.* a). To ascertain that endogenous succinate alone is not responsible for the observed changes we attempted to add 20 mM glucose after 2 μM rotenone, thus blocking Complex I. There was neither a respiratory, nor a $\Delta\Psi_m$ elevation.

Compared to the 6 mM glucose additions, 20 mM glucose also induced four times higher $\Delta\Psi_m$ jumps (Figure 19 d vs. c) in our arbitrary fluorescence scale when monitored by TMRE (note it is non-linear vs. $\Delta\Psi_m$). Oligomycin addition after glucose, establishing the nonphosphorylating state$_i$4, still raised $\Delta\Psi_m$, but only up to 15 mM glucose. In contrast to the lower values of incremental glucose, the oligomycin addition after 20 mM glucose did not further raise $\Delta\Psi_m$ indicated by TMRE (Figure 19 c, d). A similar pattern for the derived $\Delta\Psi_m$ was observed when JC-1 fluorescent probe was employed and ratio of its emissions at 593 nm to 537 nm was used as an index of increasing $\Delta\Psi_m$ (Figure 19 e, f). However, since this ratio represents a different $\Delta\Psi_m$ scale, it appeared that addition of 20 mM glucose still elevated $\Delta\Psi_m$ indicated by JC-1. Again, the relationship of the emission ratio with regard to $\Delta\Psi_m$ is nonlinear and increments represent values of several mV only.
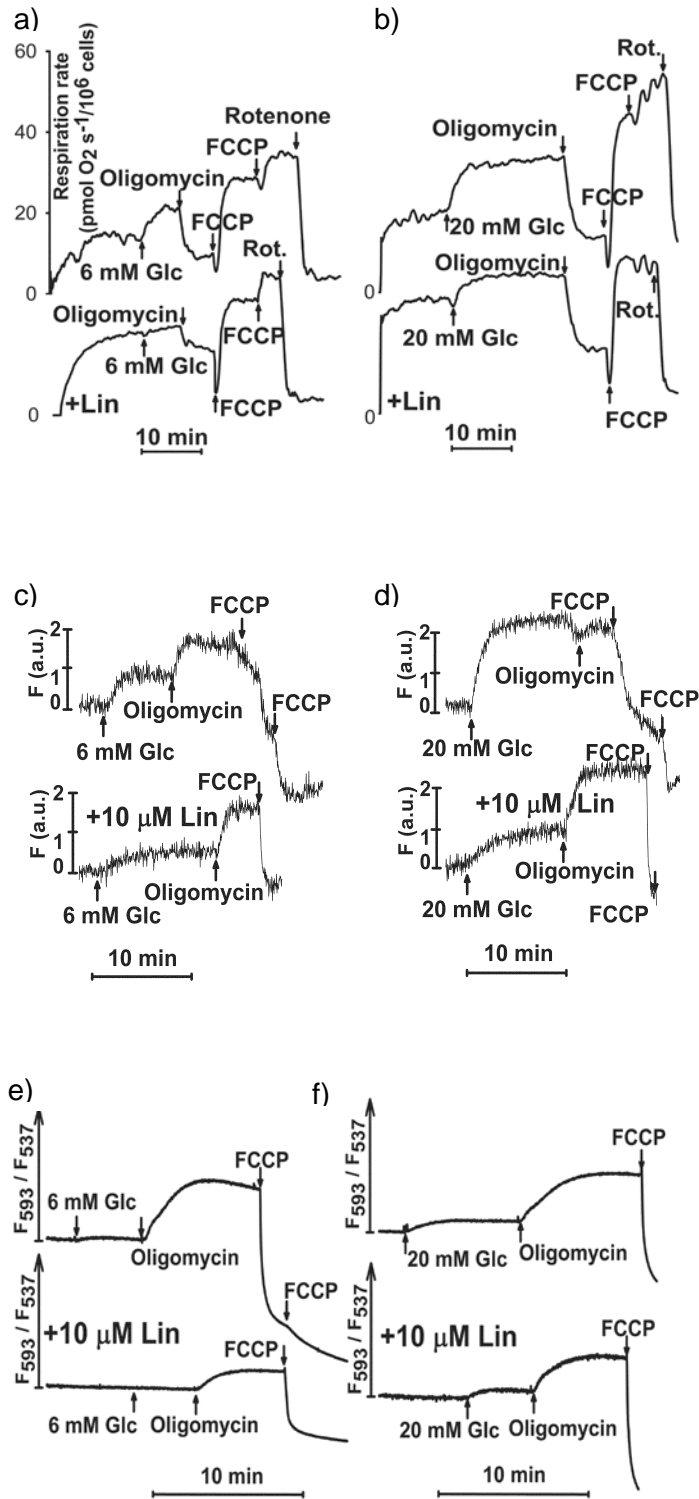
Figure 19 Increase of respiration (**a,b**) and in situ mitochondrial membrane potential as reflected either by TMRE (**c,d**) or JC-1 (**e,f**) upon addition of 6 (**a,c,e**) and 20 (**b,d,f**) mM glucose to glucose-depleted INS-1E cells. The upper trace of each panel represents run without addition of fatty acid, the lower in presence of 10 μM linoleic acid added prior to the initiation of the recording.

4.3.4   Effect of fatty acid on state 3 and state 4 respiration in INS-1E cells

Our further attempts concerned with the reported phenomenon of lipotoxicity. We intended to elucidate its bioenergetic basis, studying the simplest instant effect of free fatty acids on GSIS not involving information signaling or changes in protein expression profile. When 50 - 200 µM linoleic acid was added to INS-1E cells in the RPMI medium containing FCS (leaving only a minor portion of fatty acid free), state$_i$3 respiration increased 1.06-fold, 1.3-fold, and 1.6-fold upon addition of total 50 µM, 100 µM and 200 µM linoleic acid, respectively (Table 2, the fourth column). Similar acceleration of cell respiration was observed in state$_i$4 under these conditions (Table 2, the fifth column).

Table 2 Bioenergetic parameters of INS-1E cells cultivated in RPMI medium.

Linoleic acid total added	State$_i$3/state$_i$4	State$_i$3$_{Lin}$/state$_i$4$_{Lin}$	State$_i$3$_{Lin}$/state$_i$3 respirations	State$_i$4$_{Lin}$/state$_i$4	Uncoupled/state$_i$4
0	2.4±0.2[b]	n/a	n/a	n/a	4.2±0.5[c]
50 µM		2.3±0.2[c]	1.06±0.01[a]	1.12±0.02[c]	
100 µM		2.1±0.1[c]	1.3±0.1[a]	1.20±0.02[c]	
200 µM		2.0±0.1[c]	1.6±0.3[a]	1.6±0.2[c]	

The second and third columns point to the respiratory control ratio in the absence and presence of linoleic acid, respectively. The fourth column reflects fatty acid-induced uncoupling at state$_i$3, the fifth column lists values of fatty acid-induced uncoupling at state$_i$4. The last column shows ratio of maximum (uncoupled) and minimum (state$_i$4 respiration).
Values are means ± SD; [a] n=6, [b] n=14, [c] n=5, [d] n=4.

4.3.5   Fatty acid effect on GSIS

Linoleic acid at 5 and 10 µM reduced the response of respiration increase (Figure 19 a, b – the lower traces) as well as $\Delta\Psi_m$ jumps (Figure 19 c, d, e, and f – the lower traces) upon glucose addition to glucose-depleted INS-1E cells in KRBH medium. This effect may be also expressed as the influence on the state$_i$3/state$_i$4 respiration ratio (Figure 20 a). Glucose-depleted cells exhibited state$_i$3/state$_i$4 ratios on average 1.08 ± 0.01 (n=4). Without fatty acid state$_i$3/state$_i$4 respiration increases after glucose addition from 1.3 to 2.4 for the incremental glucose between 4 and 15 mM and the ratio is kept nearly constant at high incremental glucose between 15 and 25 mM. This reflects increasing magnitude of oxidative phosphorylation from its lower extent (given by state$_i$3/state$_i$4 ratios close to 1.3; note the ratio of 1 means no phosporylation) to its maximum extent above 15 mM. In turn, 10 µM linoleic acid shifted this dependence towards lower ratios, so that maximum state$_i$3/state$_i$4 respiration ratio reached only 1.8 after glucose addition between 15 and 25 mM (Figure 20 a – the lower curve). The effects of linoleic acid were reversible, since they nearly vanished when BSA was added after its addition.

In contrast to no glucose addition, at incremental glucose 10 to 20 mM respiration has been accelerated by 10 μM linoleic acid with a higher extent in state$_i$4, and by much lower extent in state$_i$3, (Figure 20 b). In both cases acceleration decreased with the increasing glucose.
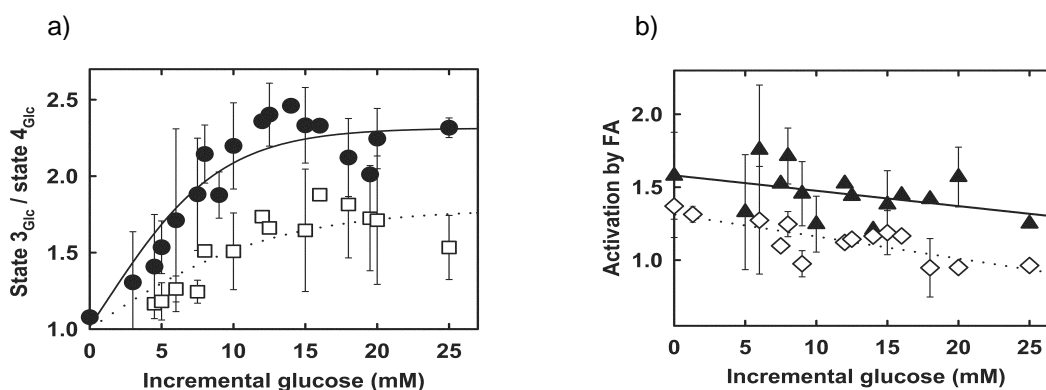
Figure 20 Ratios of state$_i$3/state$_i$4 respiration and fatty acid-induced uncoupling at state$_i$3 and state$_i$4 after glucose addition to glucose-depleted INS-1E cells.

a) Dose–responses on incremental added glucose in the absence (black circles) and presence of 10 μM linoleic acid (white squares) are depicted for ratios of endogenous state$_i$3 vs. endogenous state$_i$4 respiration of INS-1E cells. The state$_i$4 was set by 100 ng/ml oligomycin, added after glucose (or for zero glucose in separate runs before glucose). Data were fit by sigmoids.
b) A mild uncoupling manifested as n-fold acceleration of respiration by 10 μM linoleic acid is shown in response to the incremental glucose added either at endogenous state$_i$3 (white rhombi) and endogenous state$_i$4 (black triangles), set by 100 ng/ml oligomycin. Data were fit by linear regressions.
When S.D.'s are indicated, more than three estimations were made for each quantity.

4.3.6 ATP/ADP ratio

Reduction of respiration and $\Delta\Psi_m$ elevations by a fatty acid reflects partially disrupted glucose-sensing function in INS-1E cells due to mild uncoupling. This is further documented by the reduced ATP/ADP ratio, amounting merely values (n=4) of 1.3 ± 0.6, 1.3 ± 0.3, and 1.7 ± 0.6 at additions of 7 mM, 10 mM, and 20 mM glucose, respectively, to the glucose-depleted INS-1E cells, while values for the ratio not affected by addition of fatty acid were (n=4) of 2.7 ± 0.3, 4.3 ± 0.6, and 6.1 ± 0.7, respectively. 60 min glucose depletion treatment led to ATP/ADP ratio values of 1.2 ± 0.2 (n=4) (slightly lower ratios were obtained when oligomycin was present during the treatment).

4.3.7 Orthodox GSIS assay

In order to demonstrate that the respiration and $\Delta\Psi_m$ elevations proceeded simultaneously,

via ATP/ADP ratio changes, with GSIS in glucose-depleted cells, the amount of insulin release during 15 min after the glucose addition was measured. This assay represents the desired orthodox GSIS assay, since one initiates it at nearly zero glucose. Figure 21 shows the data, demonstrating increasing GSIS with increasing glucose in glucose-depleted INS-1E cells. A derived stimulation index was ~8, being a slightly higher than the index measured by [283]. 10 μM linoleic acid impaired GSIS. Stimulation index decreased from 8 to 6 and the response at 20 mM glucose was reduced twice. Thus the impaired GSIS represents an explicit basic effect of fatty acid.

In turn, GSIS of isolated Langerhans islets cultured at 5 mM glucose amounted ~50 μIU·min^{-1} or 2 ng·min^{-1} per equivalent of 10^6 β-cells in isolated islets, being only a slightly higher than in INS-1E cells.
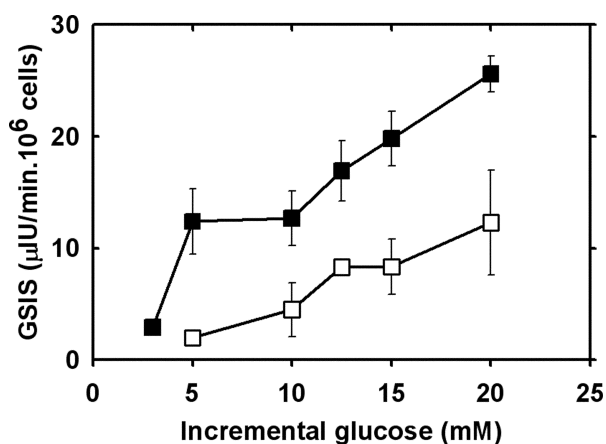
Figure 21 Insulin secretion upon various additions of incremental glucose.

INS-1E cells, depleted of glucose were assayed in the KRBH medium upon various additions of incremental glucose in the absence (■) and presence of 10 μM linoleic acid (□). After 15 min from the glucose addition, the incubations were frozen and assayed for insulin. GSIS was calculated by subtracting background reached in parallel incubations without glucose.

4.3.8 Measurement of respiration of glucose-depleted isolated islets

In order to ascertain whether behavior of INS-1E cells is similar to responses of β-cells in isolated Langerhans islets, islets under the same conditions in KRBH medium (Figure 22 a) or in RPMI medium were assayed (Figure 22 b). Again, when glucose was not depleted, GSIS-linked respiration burst was not observed (Figure 22 b). When islets were depleted of glucose similarly as INS-1E cells, respiration increase induced by 20 mM glucose was observed also in

the islets (Figure 22 a).
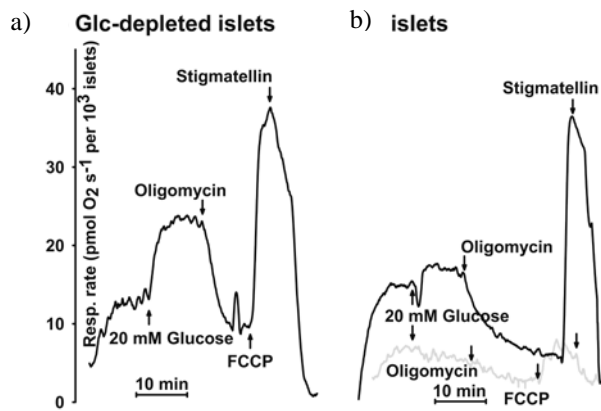
Figure 22 Bioenergetic parameters of isolated Langerhans islets at intact or impaired GSIS.

Islets were cultivated in RPMI with 11mM (**a** and **b** – the lower grey trace) and 5mM (**b** – the upper trace) glucose for 24 h. The sample in (**a**) was depleted of glucose using the identical procedure as described for INS-1E cells and assayed in KRBH medium. The samples in (**b**) were not depleted of glucose and were assayed in RPMI medium containing 5mM glucose (the upper trace) or 11mM glucose (the lower, grey, trace).

4.4   4Pi microscopy of Langerhans islets β-cells

4.4.1   Comparison of mitochondrial network of β-cells from non-diabetic and Goto Kakizaki rat visualized by confocal microscopy

We first tested samples using both 3D and 2D imaging by conventional confocal microscope (Figure 23). Specifically, 3D *iso*-surface plots constructed from the obtained data for control β-cells of Wistar rats (Figure 23 a-d) and diabetic β-cells of Goto Kakizaki rats (Figure 23 e,f) did not show any significant distinction. When viewed by an angle that included the worse z-axis resolution of conventional confocal microscopy, the presumed tubular structure was blurred into apparently fused columns (Figure 23 b,d,f). Also 2D conventional images, selecting random mitochondrial network sections of β-cells of non-diabetic (Figure 23 g) or diabetic Langerhans islets (Figure 23 h), were of a nearly indistinguishable pattern.

4.4.2   Comparison of mitochondrial network of β-cells from non-diabetic and Goto Kakizaki rat visualized by 4Pi microscopy

The optimized procedure for 3D 4Pi imaging of mitochondrial network in lentivirally transfected Langerhans islets with mRoGFP-constructs yielded superior 3D reconstructions of mitochondrial networks within the β-cells of isolated Langerhans islets as displayed by the three ways described (Figure 24 - Figure 27). The 4Pi images allow to distinguish significantly different features of the mitochondrial networks in control and diabetic β-cells. One can clearly see that β-cells of control Langerhans islets show equally dense and highly interconnected mitochondrial networks (Figure 24 a, b; Figure 25 a, b; Figure 27 a, b).

β-cells, which were still displaying the GLUT2 antigen, in Langerhans islets isolated from diabetic Goto Kakizaki rats exhibited in five evaluated islets a more disintegrated network, when compared with non-diabetic islets. Examples with the most disintegrated networks are shown in Figure 24 c, d; Figure 25 c, d, e, f; and Figure 26. This conclusion can be rigorously derived from the fact that when increasing the *iso*-surface threshold in 3D displays (Figure 25 c,d; and Figure 25 e,f, for the second sample), the network is more disintegrated at I_T of 40 (Figure 25 d,f)
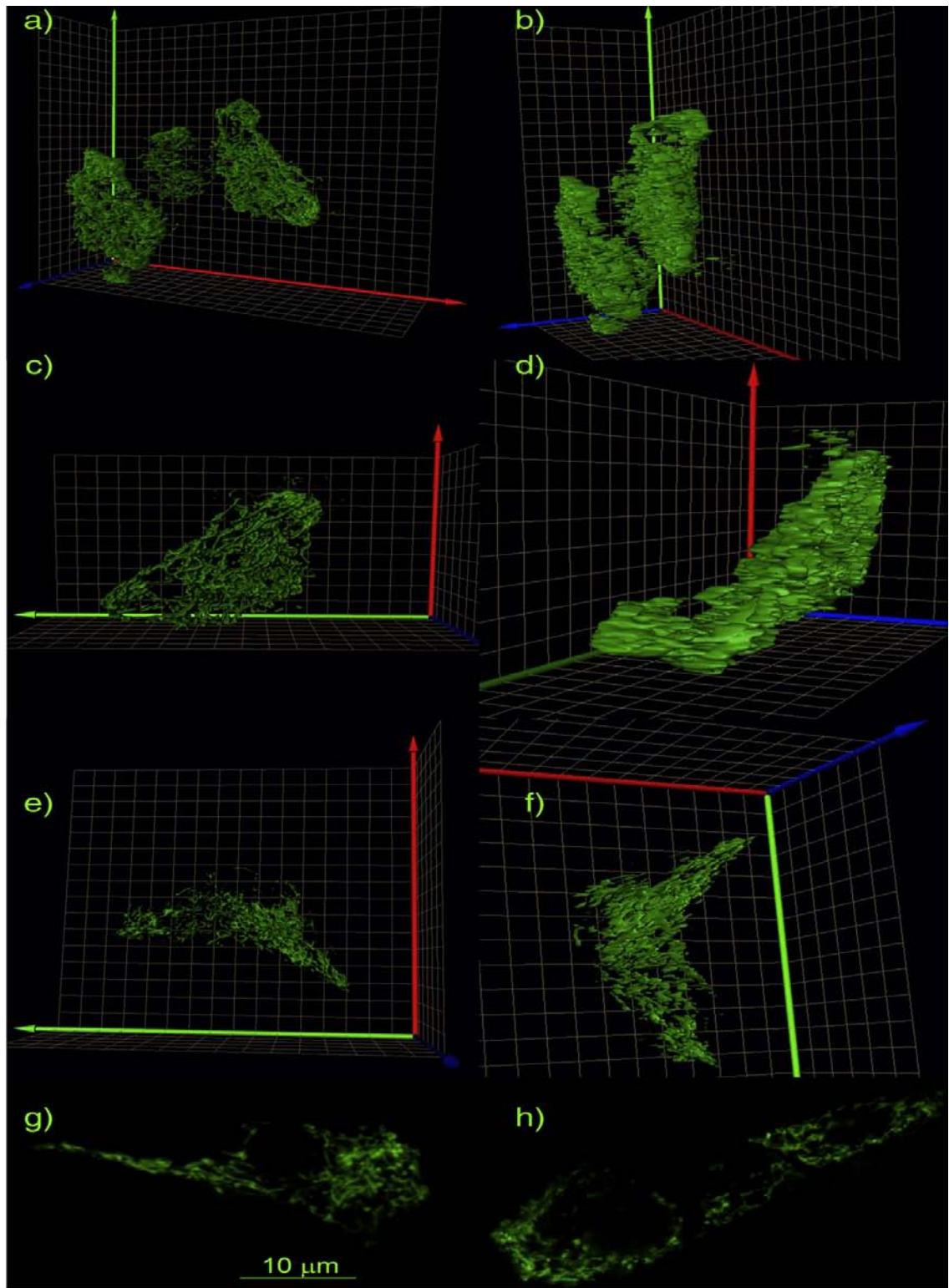
Figure 23 Conventional confocal 3D imaging and 2D imaging of mitochondrial network in mRoGFP-transfected non-diabetic and diabetic β-cells of Langerhans islets.

Data were displayed in iso-surface plots for 3D imaging (**a–f**) of living β-cells, isolated from control (Wistar) rats (**a–d**) and from diabetic Goto Kakizaki rats (**e, f**). A 1 μm 3D grid is shown in the background. Color-coding for axes: green -Y axis; red - X axis; blue - Z axis.
Panels **g**) and **h**): 2D imaging of control (**g**) and diabetic β-cells (**h**).
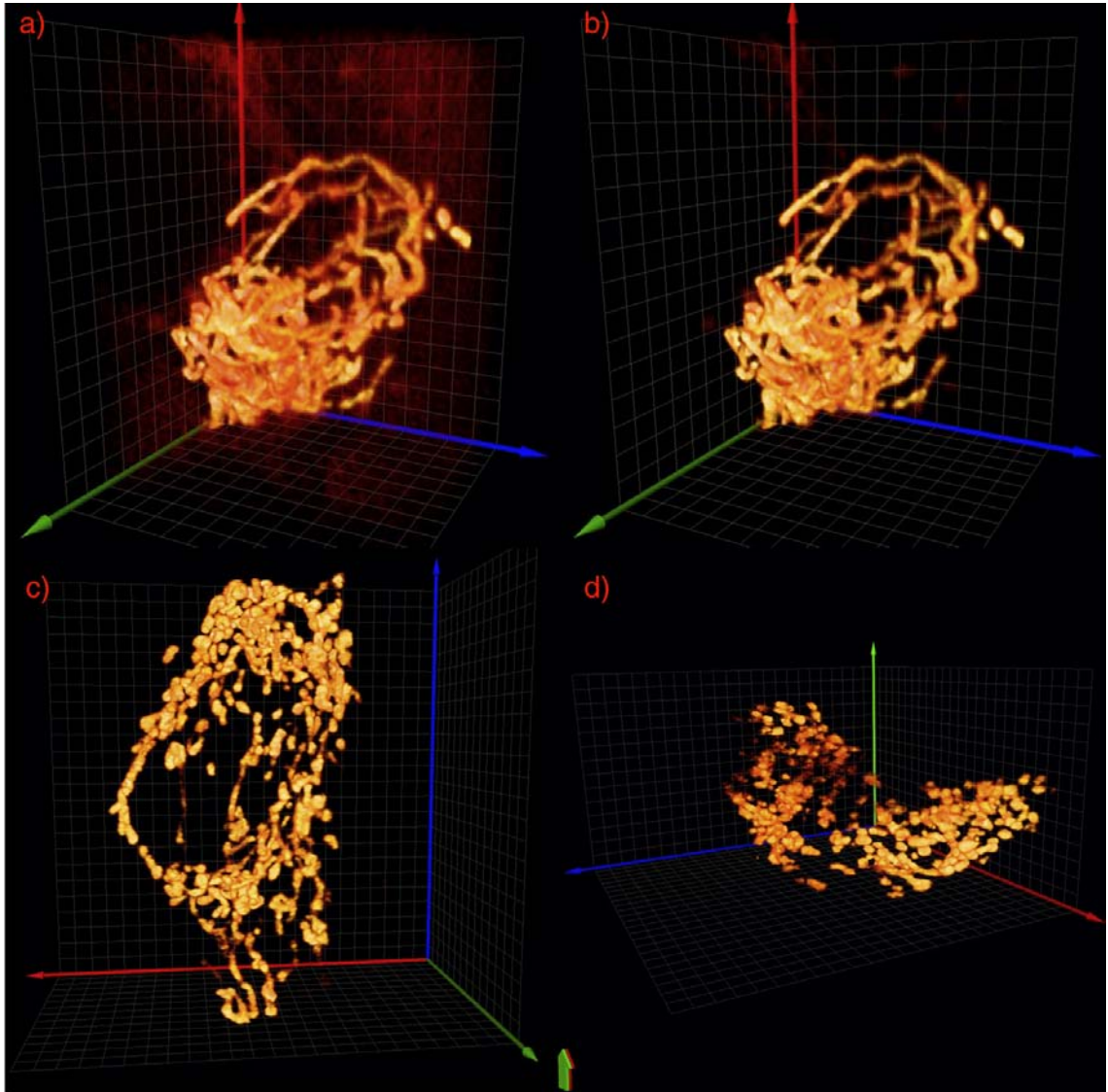
Figure 24 4Pi imaging of mitochondrial network of mRoGFP-transfected β-cells of Langerhans islets isolated from control Wistar rats (**a,b**) and diabetic Goto Kakizaki rats (**c,d**)

Voltex 3D projections. The three-point deconvolved data are shown for a single selected control β-cell of Langerhans islets isolated from non-diabetic Wistar rats (**a**) $I_T=1$, (**b**) $I_T=15$; and for two examples of diabetic β-cells of Langerhans islets isolated from Goto Kakizaki rats (**c,d**), $I_T=15$. A 1 μm 3D grid is shown in the background. Color-coding for axes: green - Z axis; red - X axis; blue - Y axis.
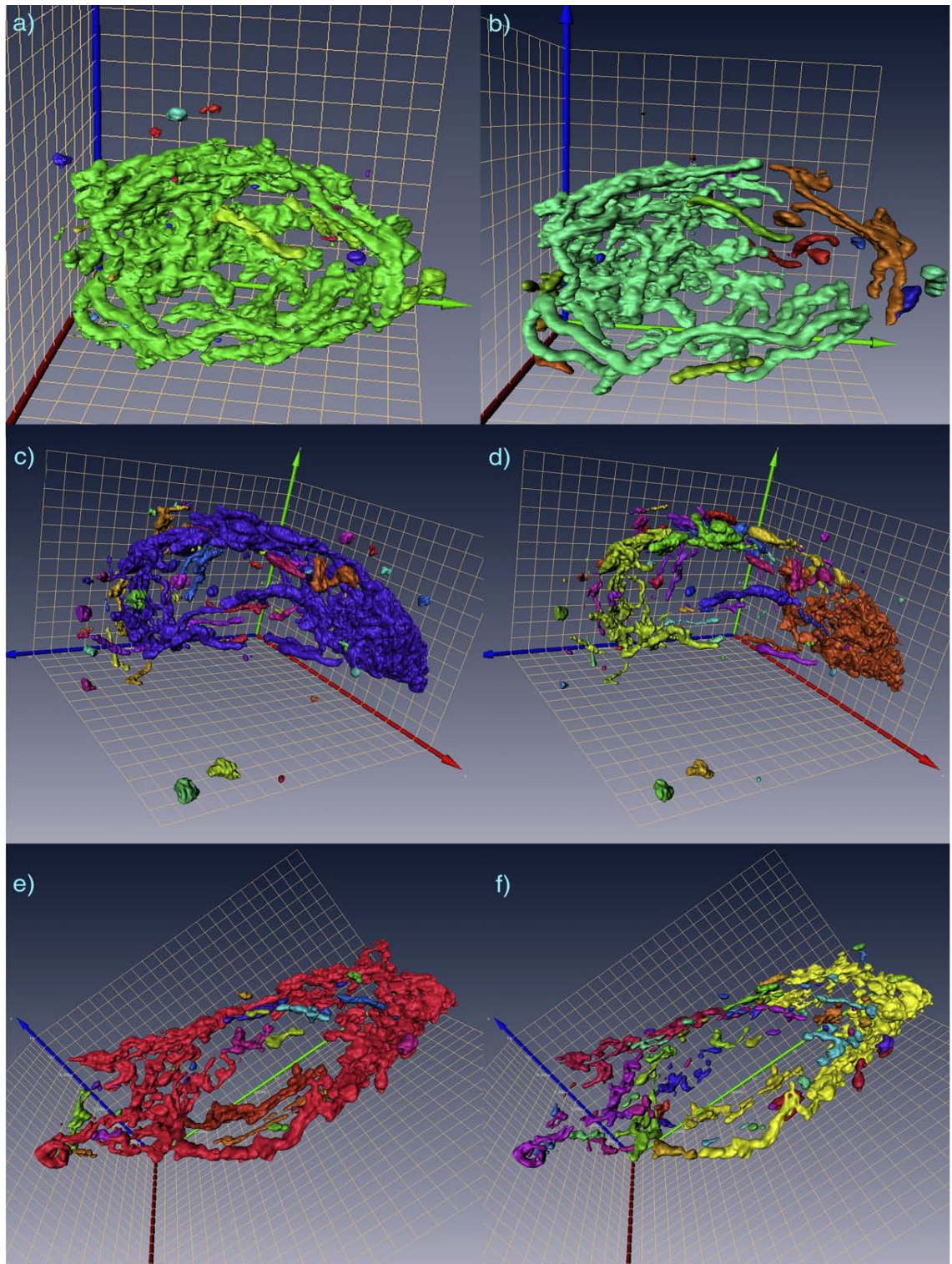
Figure 25 Iso-surface projections for 4Pi imaging of mitochondrial network in β-cells of control (Wistar) and diabetic Goto Kakizaki rats.

Unlike non-diabetic phenotype (I_T=20: panel (**a**); I_T=40: panel (**b**)), the diabetic phenotype in the Goto Kakizaki rats was manifested by higher disintegration apparent at I_T=40 (panels (**d**) and (**f**) showing two different islet samples) in iso-surface projections. Certain disintegration is recognized also at I_T=20 (panels (**c**) and (**e**)), which represents the minimum noise levels subtracted. A 1 μm 3D grid is shown in the background. Color-coding is used to distinct the different objects. Color-coding for axes: green - Z axis; red - X axis; blue - Y axis.
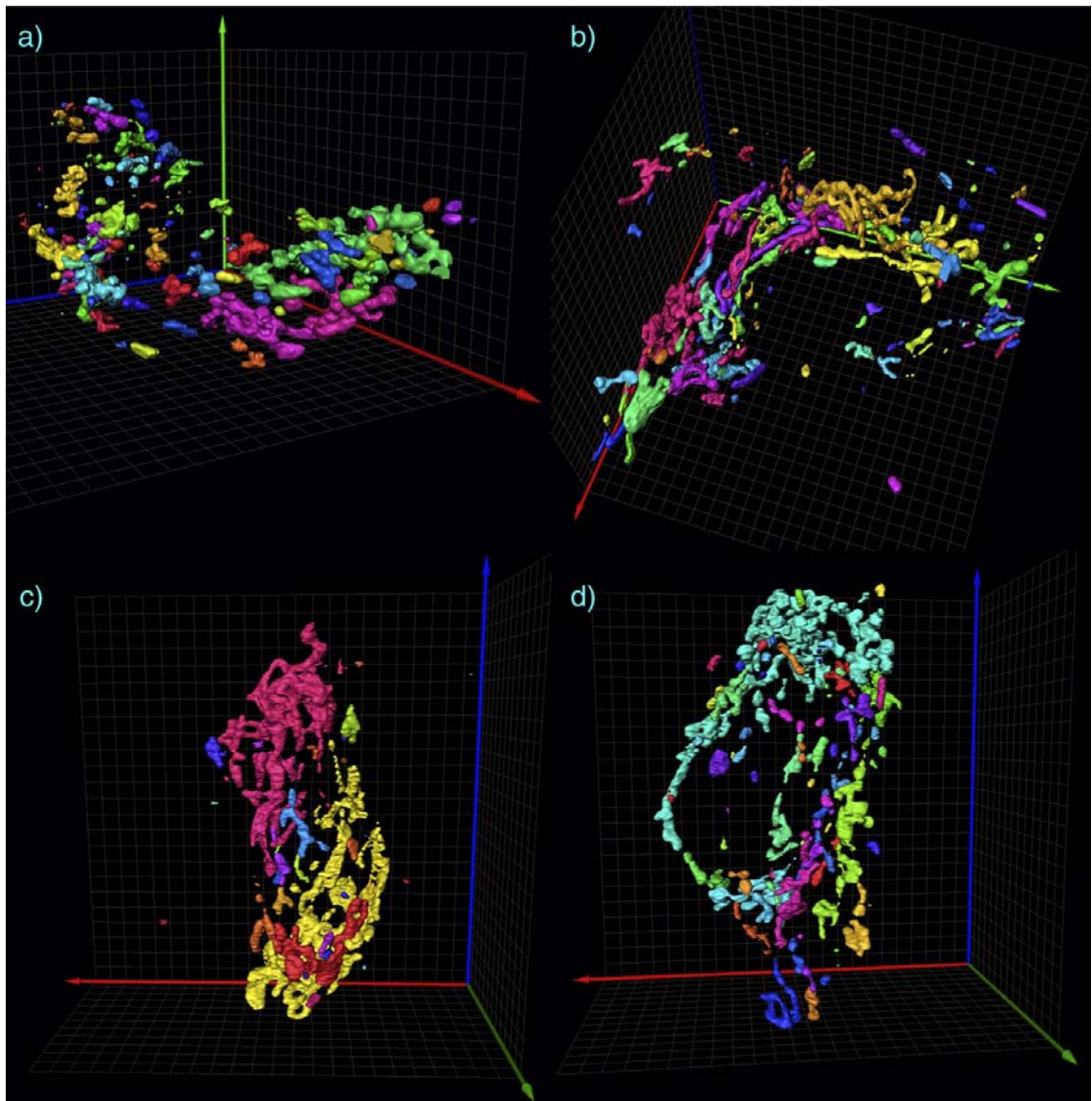
Figure 26 4Pi imaging of mitochondrial network in selected diabetic β-cells of Goto Kakizaki rats.

Diabetic phenotype in the Goto Kakizaki rats is manifested by disintegration of originally highly interconnected mitochondrial reticulum as observed in control β-cells. Iso-surface mode 3D projections with I_T=40 were created with Amira 5.2.2. A 1 μm 3D grid is shown in the background. Color-coding is used to distinct the different objects. Color-coding for axes: green - Z axis; red - X axis; blue - Y axis.
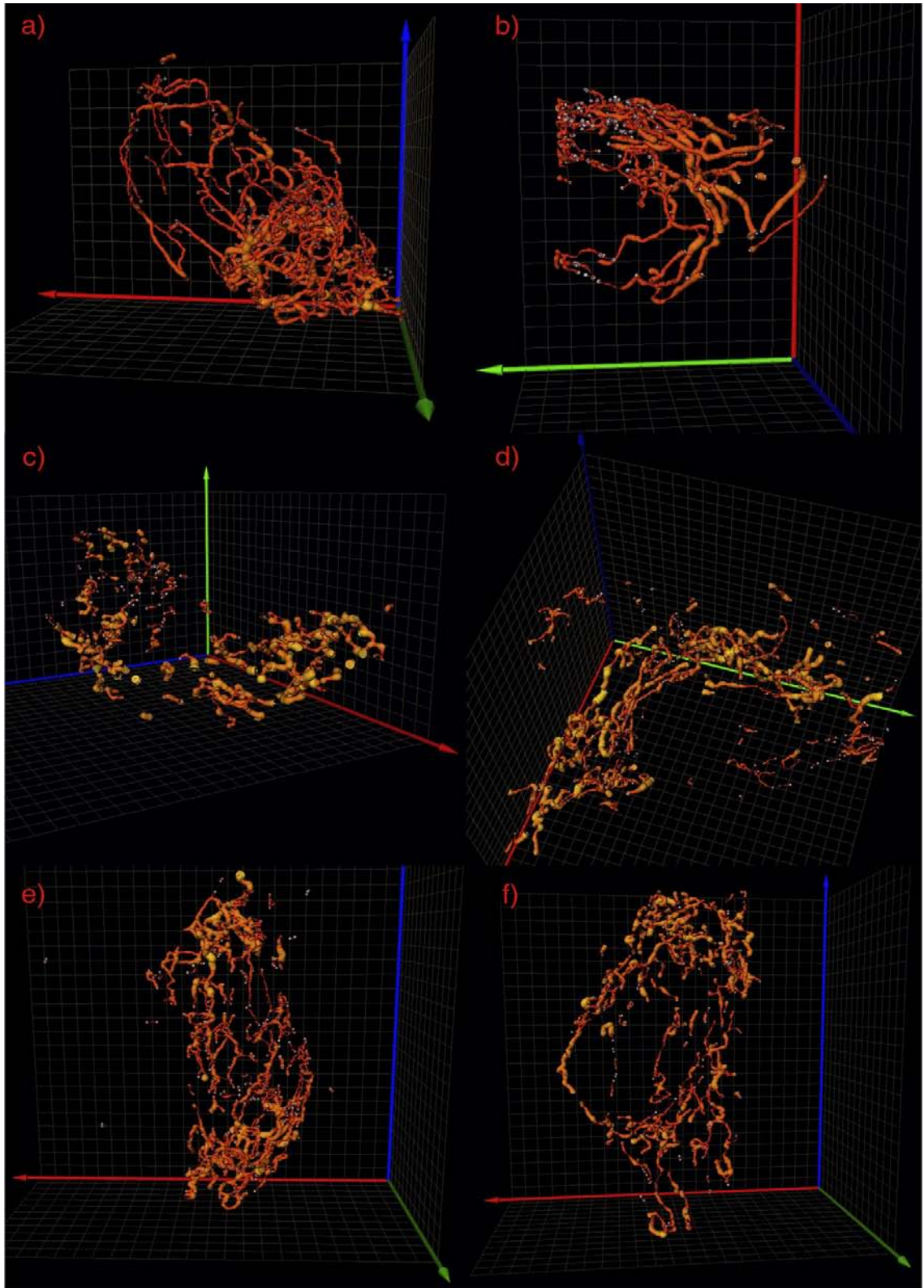
Figure 27 "Autoskeleton" projections of 4Pi imaging of mitochondrial network in β-cells of control (Wistar) and diabetic Goto Kakizaki rats.

Unlike for control β-cells (**a,b**), diabetic phenotype of islet β-cells from the Goto Kakizaki rats (four different diabetic β-cells are represented in panels (**c-f**) is manifested also in "Autoskeleton" projections created with Amira 5.2.2. A 1 μm 3D grid is shown in the background. Color-coding for axes: green - Z axis; red - X axis; blue - Y axis.

4.4.3 *Analysis of volume distribution pattern and signal density distribution pattern*

From the histograms of intensity distribution over 256 signal levels, we estimated that the main noise level is below 10. Histograms for all samples had the same shape and we concluded that it is legitimate to compare samples at the same I_T levels. The three-point deconvolved 4Pi data, i.e. data still including the background noise, typically gave signal from two thirds of the 3D imaged volume. After a proper background subtraction only ~5% of the 3D imaged volume was occupied by the mitochondrial network. The mRoGFP-accessible space, i.e. mitochondrial matrix, can be ascribed to the "complete" volume with subtracted noise, i.e. at I_T levels of 10 and higher; alternatively signals of higher intensities but comprising lower volumes of typically 67% and 40–45% are calculated at I_T levels of 20 and 40, respectively, when compared to 100% calculated on the basis of I_T of 10. Having adjusted signal and optimum I_T levels, we analyzed number and volume size of the objects in the images of mitochondrial reticulum of non-diabetic and diabetic β-cells. Figure 28 shows the distribution of a relative volume for fragments of mitochondrial reticulum at I_T levels of 20 for control and diabetic β-cell networks. The relative volumes of fragments (as percentage of the largest one) describe distinction between control and diabetic β-cell networks very clearly. Non-diabetic mitochondria exhibit volume of the second, third, fourth, etc., fragments relative volume, significantly lower than diabetic ones. This indicates that in non-diabetic cells the mitochondrial network consists of mainly one large mitochondrion with only a few small isolated fragments. In diabetic cells, in contrast, several fragments of intermediate size exist, showing more frequent fragmentation. In extreme cases, the diabetic β-cells exhibited a completely disintegrated mitochondrial reticulum with numerous small spherical and short segment objects (Figure 24 d, 26 a, and 27 c).

4.4.4 *Other parameters of islets β-cells mitochondrial network*

The average tubule diameter of non-diabetic islet β-cell mitochondria taken by the "interference" method (derived from point spread functions) and "ruler" method (measuring distances on original xz stacks) was 230 ± 47 nm (n=50) and 214 ± 16 nm (n=60), respectively, *i.e.* significantly smaller than the values of 270 ± 28 nm and 270 ± 40 nm, respectively, previously reported for INS-1E cells [23]. The tubule (object) diameter in diabetic β-cells was slightly higher, on average 279 ± 48 nm (n=72) and 236 ± 27 nm (n=100) as taken by the the "interference" and "ruler" method, respectively (Table 3). The diameter distributions revealed that in diabetic β-cells a higher portion of diameters of 250 nm and above exists, whereas in controls the most frequent diameters are below 250 nm.

Other major parameters (Table 3), such as the number of branching points and number of "double diameter" segments or bigger "cisternae" located at bifurcations and branching points,

exhibited similar pattern as revealed for mitochondrial network of INS-1E cells [239]. In contrast, non-diabetic islet β-cells contain a higher number of regions where tubules are fused into more bulky cisternae, as well as tubules of about twice the "norma" diameter, and irregular shapes (Figure 24 a,b and 25), when compared to INS-1E cells. Disintegration of the network in diabetic β-cells reduced also the number of these cisternae (Table 3).
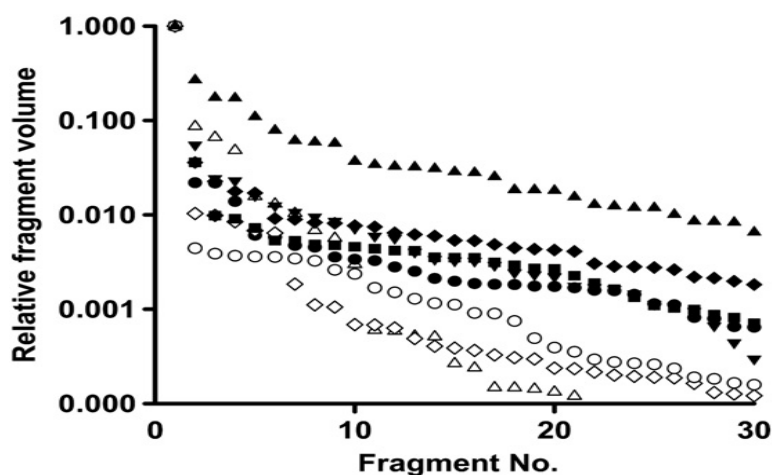
Figure 28 Distribution of relative fragment volume (related to the maximum one) for mitochondrial network of β-cells of Langerhans islets from non-diabetic Wistar and diabetic Goto Kakizaki rats.

The fragmentation analysis of 3D data is shown for three non-diabetic β-cells (open symbols) and five diabetic β-cells (close symbols) for isolated Langerhans islets from Wistar rats and Goto Kakizaki rats, respectively. The volume of the largest mitoreticulum (fragment) present in each cell was set to 1 and the other fragments were related to it as fractions of this unit volume. The relative volume is then plotted against the number of objects of each volume size.

Table 3 Diameters of tubules and other characteristics of mitochondrial networks in primary β-cells of control and diabetic Langerhans islets.

Rat model	Diameter (interferometric method) (nm)	Diameter (ruler method) (nm)	No. of reticula at l_T 20 (l_T 40)	No. of spheres at l_T 20 (l_T 40)	No. of short segments at l_T 20 (l_T 40)	No. of cisternae
Control (Wistar) average	230±47 nm	214±16 nm				
Sample 1	215±46 nm	209±14 nm	1 (1)	9 (10)	6 (5)	40
Sample 2	231±40 nm	217±12 nm	1 (3)	8 (10)	12 (15)	25
Sample 3	240±50 nm	215±13 nm	1 (1)	4 (10)	4 (10)	10
Diabetic – average (Goto Kakizaki)	279±48 nm	236±27 nm				
Sample 1	279±55 nm	233±27 nm	1 (4)	15 (15)	5 (10)	20
Sample 2	298±33 nm	234±23 nm	2 (3)	15 (10)	15 (34)	5
Sample 3	277±38 nm	236±18 nm	1 (0)	25 (25)	37 (71)	3
Sample 4	299±48 nm	239±23 nm	1 (2)	15 (10)	15 (34)	3

Diameters evaluated by the two ways as described in Materials and methods are listed for selected images of Langerhans islet β-cells. There were 13 to 20 estimates and 20 estimates for interferometric and ruler method, respectively. Data of all samples control or diabetic were also averaged ("Average"). "Cisternae" are defined as "double diameter" segments or bigger objects located at bifurcations and branching points.

5   DISCUSSION

5.1   Putative activation of UCP1 protonophoretic activity by alkylsulfonates

Undecanesulfonate and alkylsulfonates generally do not possess chemical properties of classical protonophoric uncouplers, namely being able to diffuse through lipid membranes in both protonated and deprotonated (anionic) forms. Our laboratory has previously shown that UCP1 can catalyze the uniport of $C_{11}SO_3^-$ anion across the membrane [46, 289]. However, due to the strong acidity of sulfonate group ($pK_a \sim 2$), which is highly disociated under physiological conditions at $\sim$ pH 7, undecanesulfonate is able to transport only a small portion of H^+ across the membrane. When $C_{11}SO_3^-$ is added to both BAT and heart mitochondria, it slightly accelerates respiration (Figure 8, page 46; Figure 10, page 48). This effect is, however, UCP1 independent, since it occurs to the same extent in heart mitochondria where UCP1 is not present. Moreover, membrane potential is not altered in BAT under the same conditions (Figure 9, page 47). Since uncoupling is defined by the increasing respiration at decreasing $\Delta\Psi_m$, this nonspecific effect has no nature of a protonophoric uncoupler mechanism. Higher acceleration of respiration in the presence of BSA can be explained by the release of FAs bound on BSA and displaced by $C_{11}SO_3^-$. These instantly released FAs provide themselves as UCP1 cycling substrates, so only in BAT mitochondria this effect is superimposed onto the nonspecific effect (Table 1, page 51; Figure 8, page 46; Figure 9, page 47 and Figure 10, page 48). The nonspecific effect represents another part of the effect, seen in both BAT and heart mitochondria in the absence of BSA.

Moreover, we have demonstrated that under carefully adjusted conditions when the net FA-induced uncoupling is assayed (Figure 11, page 50), the addition of $C_{11}SO_3^-$ may even slightly inhibit the uncoupled respiration. This finding agrees well with the previous work showing mutual competition of FAs and alkylsulfonates in a so-called docking site on UCP1 [1, 46, 290-292] and shows that $C_{11}SO_3^-$ may behave with regard to the FA-induced uncoupling by the qualitatively same way as in UCP1-containing proteoliposomes [46, 50].

Measurements of UCP1 reconstituted into planar lipid bilayers, exhibited the same basal conductance in the absence of FAs as in the absence of UCP1 [293], so one must conclude that FAs are absolutely essential for the uncoupling function of UCP1. These data excluded the relevance of *Model iii*.

Though not explicitly stated, analysis of Rial *et al.* results [59] would exclude *Model ii* as

well as *Model i*. A strong acidity of $C_{11}SO_3^-$ would not at all allow it to act as a local buffer according to the *Model ii* under any physiological conditions. Particularly, it would not be possible, if $C_{11}SO_3^-$ would be required to supply an incomplete H^+ pathway by protons and consequently induce uncoupling mediated by UCP1.

Hence, we conclude that FA cycling, *Model i*, cannot be excluded on the basis of the data presented by Rial *et al.* [59], which are similar to the Figure 8 a, page 46.

5.2   Fatty acid interaction with UCP2

Previous studies of interaction of native hamster BAT mitochondrial UCP1 with 5-DOXYL-stearic acid (5-DSL-FA) [292] or spin-labeled ATP were followed [296]. These early studies have demonstrated competition of hexanesulfonate, undecanesulfonate, and octadecanesulfonate with 5-DSL-FA and indicated an allosteric nature of ATP binding to UCP1 with respect to the FA binding site. Similarly as with UCP1, the intention was to determine, whether fatty acids are substrates for UCP2. Binding of fatty acids to UCP2 is a prerequisite for the fatty acid cycling mechanism of uncoupling as initially proposed by Skulachev for UCP1[45].

The development of the solubilization/reconstution of hUCP2 expressed in *E. coli* allowed us to achieve adequate yields and functionally refolded protein for ESR spectroscopy, therefore allowing the use of this powerful biophysical technique to study this protein. In the present study hUCP2 has been isolated from inclusion bodies by solubilizing it in the non ionic micelles of $C_{12}E_9$ detergent. In order to show that fatty acids are substrate for UCP2, we successfully used spin-labeled fatty acids for binding studies. DOXYL stearic acid and PROXYL palmitic acid were found to be the most useful probes.

The viscous micellar environment causes substantial immobilization of spin-labeled fatty acids in the absence of protein as reflected by peak separations in the order of 30 Gauss. However, in the presence of UCP2, $2A_{zz}$ values of more than 40 Gauss were observed for all spin-labeled fatty acids employed, *i.e.* 4-PROXYL palmitic acid as well as 5- and 7-DOXYL stearic acid with the corresponding maxima and minima as denoted h_{+II} and h_{-II} according to Reboiras and Marsh [297]. 4-PROXYL-palmitic acid bound to UCP2 exhibited a clearly separated h_{+II} immobile peak and highly reduced h_{+1M} mobile peak in the EPR spectrum (Figure 13, page 54), which indicates that spin-labeled fatty acids when bound to UCP2 are immobile. The mobility of the spin label increased with the position along the fatty acid chain as revealed by decreasing 2Azz values from 4-PROXYL over 5-DOXYL to 7-DOXYL and 16-DOXYL which was completely devoid of the immobilized component. Hence, it is the carboxyl group of the fatty acids that mediates binding to UCP2. Even if the micellar system cannot completely simulate UCP2 inserted into the IMM, it is reasonable to assume that this immobilization takes place also with native FAs *in vivo*.

The specificity of the interaction of these spin-labeled fatty acids with UCP2 was investigated by the competition with known activators of UCP2-mediated uncoupling, palmitic, arachidonic, and eicosatrienoic acid. They all led to a decrease of the h_{+II} and h_{-II} peaks, and in the case of the unsaturated fatty acids even at concentrations significantly lower than that of 4-PROXYL-palmitic acid, demonstrating binding to the protein and not just some other

interaction within the micelles. Upon increasing FAs concentration (Figure 14-Figure 16, page 55-57), the restricted motion of the spin probe is gradually released, which is manifested by the rise of the mobile peaks h_{+1M} and h_{-1M} in the low and high field, respectively. This indicates that fatty acids compete with 4-PSL-FA and that the spin probe binds to the natural fatty acid binding site.

Assuming also that UCP2 likewise other UCPs and carriers of the mitochondrial gene family [298] possess similar structure as resolved for the mitochondrial ADP/ATP carrier, one can speculate that either FAs bind to a central cavity into which carboxyatractyloside (CAT) binds to the ADP/ATP carrier [299] or to one of six α-helices forming the walls of the cavity.

5.3 Bioenergetic parameters of insulinoma INS-1E cells in relation to GSIS

To study the bioenergetics of β-cells in intact islets is not an easy task. Isolation of islets is a long-lasting procedure and relatively large quantity of islets is needed for the assays. Moreover, pancreatic islets postnatally develop an abundant glomerular-like microcirculation system, which ensures that no portion of an islet is more than one cell away from arterial blood [300, 301]. This arrangement optimizes the condition for supply of oxygen and nutrients to the islet cells, their metabolic sensing, and the distribution of secreted hormones to target organs in order to maintain glucose homeostasis. After the isolation of Langerhans islets, the influx of substrates and oxygen into the core of islet is possible only by diffusion. Another problem is a large heterogeneity of Langerhans islets. Both problems might be overcome by trypsinization of islets and separation of a pure β-cells fraction from the cell mixture. However, it has been shown that behavior of β-cells prepared by this way is different from the behavior of β-cells within intact islet [302]. That is why we used INS-1E cells, a promising model of β-cells developed at the University of Geneva [283], for studies of glucose-sensing function and its changes under various conditions. Bioenergetics of these cells had not been previously investigated in detail.

We have confirmed that INS-1E cells as well as pancreatic β-cells sense glucose through oxidative phosphorylation linked to glycolysis and that the key coupling factor in GSIS is increasing oxidative phosphorylation, which likely elevates cytosolic ATP/ADP ratio. Subsequent activation of plasma membrane ATP-sensitive K^+ channels and Ca^{2+} channels results in exocytosis of insulin-containing granules. We have shown that insulinoma INS-1E cells elevate ATP synthesis from nearly zero at zero glucose to maximum levels at glucose >15 mM, just within the physiological glucose range (5 – 8 mM) and its expansion to hyperglycaemic range up to 20 mM. We have found that the entire span of their ATP synthesis from zero to maximum is reflected by hyperbolically increasing state$_i$3/state$_i$4 ratio of their respiration with increasing glucose concentration. We have also confirmed that the total cell ATP/ADP ratio significantly elevates under these conditions, similarly as in islets [303]. Finally, our finding that linoleic acid caused mitochondrial uncoupling with concomitant lowering of the total cell ATP/ADP ratio and impairment of GSIS may provide an explanation for one of the lipotoxic effects of fatty acids on pancreatic β-cells [304], not involving information signaling or changes in protein expression profile.

We have shown that both, respiration as well as electric component of proton motive

force $\Delta\Psi_m$, significantly increase upon glucose addition to glucose-depleted INS-1E cells. This phenomenon may be explained by a substrate overflow at maximum ATP synthesis. Substrates for the respiratory chain are derived from pyruvate as the main glycolytic output. Evidence for $\Delta\Psi_m$ increase during GSIS was provided by two distinct fluorescent probes, JC-1 and TMRE. Since two different principles determine their sensing of $\Delta\Psi_m$, our evidence is based on two independent approaches. In glucose-depleted INS-1E cells, substrate fluxes into the mitochondrial matrix originate from a steady-state cytosolic and matrix metabolism. Major influx concerns with the carnitine cycle import of fatty acid equivalents into the matrix for β-oxidation. These cells respire reportedly due to their fatty acid storages and thus surviving glucose-starvation period [288, 305, 306]. We have simulated with them an intermediate state$_i$3 by the addition of lower incremental glucose (such as 4 – 6 mM). In this state, ratio of state$_i$3/state$_i$4 respiration, reflecting the intensity of ATP synthesis, does not reach maximum levels - values only around 1.3 were found (Figure 20 a). Note that starved glucose-depleted cells attained even lower values of 1.08. Therefore, with 4 – 6 mM glucose neither respiration is maximal, since the maximum load to the mitochondrial respiratory chain is not yet attained. In starved glucose-depleted cells, mitochondria are only slightly coupled due to residual ongoing fatty acid oxidation. Uncombusted free fatty acids may in addition bring a concomitant slight uncoupling, lowering state$_i$3/state$_i$4 ratio even further. Nevertheless, ongoing respiration maintains a substantial $\Delta\Psi_m$ (or Δp) even under these conditions. Resulting $\Delta\Psi_m$ corresponds to the initial levels, from which our experiments were started, when initiating the $\Delta\Psi_m$ jumps by glucose additions. The addition of 4 – 6 mM glucose led to a further $\Delta\Psi_m$ increase, but again not to the maximum. This could be recognized from a possibility of further $\Delta\Psi_m$ raise upon oligomycin addition (setting state$_i$4). Thus, $\Delta\Psi_m$ is evidently higher at state$_i$4 than at state$_i$3. Even with 4 – 6 mM glucose, the observed intermediate respiration and the corresponding intermediate electron flow and H^+ pumping by the respiratory chain originate from the established lower substrate availability. This allows only an intermediate level of ATP synthesis driven by the intermediate H^+ backflux via the F_O part of ATP synthase. As a consequence, the resulting Δp and $\Delta\Psi_m$ are intermediate as well. Indeed, a half-maximum constant (AC_{50}) for transition of state$_i$3/state$_i$4 ratio from 1 to its maximum (2.5) lies at 7 – 10 mM glucose (Figure 20 a, page 63).

Upon the high incremental glucose addition (15 – 25 mM) rather a high Δp was established. Simultaneously, the ongoing maximum ATP synthesis was indicated by the saturated state$_i$3/state$_i$4 ratio (Figure 20 a) and the highest total cell ATP/ADP ratio. Thus high Δp exists in spite of the highest maximum ATP synthesis, which is driven by maximum H^+ backflow across the F_O part of ATP synthase, thus decreasing Δp and $\Delta\Psi_m$. Evidently, $\Delta\Psi_m$

actually increases (Figure 19 c-f, page 61) in this hypermetabolic state, reflecting the fact that the capacity of respiratory chain for H^+ pumping, hence for Δp creation, exceeds even the maximum attained capacity of the ATP synthase for the H^+ backflow.

The existence of ATP synthesis was shown by responses to oligomycin added after glucose. Oligomycin by inhibiting the F_O part of ATP synthase sets the nonphosphorylating state$_i$4, reflected by lower respiration than at state$_i$3. Therefore, the hyperbolically increasing state$_i$3/state$_i$4 ratio with glucose concentration indicates the hyperbolically increasing ATP synthesis (Figure 20 a, page 63). As we demonstrated, within the 3 – 20 mM glucose range, the whole span of raising oxidative phosphorylation is manifested. A question arises whether the above described hypermetabolic state corresponds to an actual *in vivo* situation. To answer that question, one would expect that a sudden burst from a ~ 5mM to a high glucose concentration in plasma will occur at least under conditions when a meal is provided after fasting and may indeed resemble our simulations. In conclusion, a specific oxidative phosphorylation machinery of β-cell mitochondria which enables such an ATP synthesis rise within the physiological glucose range, represents the main principle of their glucose sensing function.

The $\Delta\Psi_m$ increase during GSIS represents a paradox when compared to the usual $\Delta\Psi_m$ drop at transitions into the state 3 in isolated mitochondria [94]. When ADP is added to isolated nonphosphorylating mitochondria switching them from a classic state 2 (state 4) to the phosphorylating state 3, the $\Delta\Psi_m$ decreases. Nevertheless, there is no real paradox, and the increase in both respiration and $\Delta\Psi_m$ indicates that in zero (very low) glucose, the oxidative phosphorylation remains in a very low active state where the lack of energy substrates does not permit to generate a large $\Delta\Psi_m$ so that also respiratory rate remains low. The addition of glucose restores this $\Delta\Psi_m$ and activates the oxidative phosphorylation machinery, which leads to ATP synthesis and a steady-state $\Delta\Psi_m$ value higher than that observed in the absence of substrate.

Also regulation of metabolic fluxes by $\Delta\Psi_m$ and ΔpH may contribute to GSIS. For example, at anaplerotic role of glutamate, a higher $\Delta\Psi_m$ is established. The glutamate/aspartate carrier (Aralal isoform in β-cells) transporting glutamate is driven by $\Delta\Psi_m$. At anaplerosis the Aralal-mediated consumption of $\Delta\Psi_m$ ceases, hence $\Delta\Psi_m$ alone increases [160, 307]. Another type of observations, which may be also relevant to *in vivo* conditions, described an oscillatory pattern observed upon GSIS [305, 308]. The oscillatory isoform of muscle type phosphofructokinase was found [309] as well as coordinate oscillations in cytosolic free Ca^{2+} and the ATP/ADP ratio in glucose-stimulated mouse β-cells [310]. Oscillations in insulin secretion or O_2 consumption were observed in single mouse islets [311] and perifused rat islets [312]. Large-amplitude oscillations were found to occur in response to stimulation by glucose in single HIT-T-15 cells and were blocked by an uncoupler and proceeded even in the absence

of Ca^{2+}, but their amplitude was much higher with Ca^{2+} [313]. In agreement with our conclusions, Heart *et al.* [305] interpreted the observed respiration increase as a simultaneous ATP usage and increased mitochondrial substrate supply, which precedes and leads to closure of K_{ATP} channels which in turn increases cytosolic free Ca^{2+}. *In vitro*, a pulse of glucose causes a transient overflow of pyruvate in cell and together with a cataplerotic role of glutamate it makes the malate-aspartate shuttle highly active [160, 307]. The Aralal participating in this shuttle now consumes $\Delta\Psi_m$ in the same way as does the ADP/ATP carrier.

Being only a fraction among the effects of fatty acid to insulin producing and responding cells [304], the phenomenon of acute lipotoxicity was illustrated in our work in the simplest mode, originating from a weak uncoupling by linoleic acid, which was disrupting INS-1E cell glucose-sensing function. The instant uncoupling of mitochondria caused by a free fatty acid is the earliest effect, independent of information signaling or changes in protein expression profile. Uncoupling manifested itself as increasing respiration at slightly dropping $\Delta\Psi_m$. It reduced the otherwise high total cell ATP/ADP ratio. The linoleic acid-induced uncoupling exhibited the same strength in both state$_i$3 as well as state$_i$4 when cells were assayed in their cultivation media and were not depleted of glucose (Table 2, page 62). With the glucose-depleted INS-1E cells in KRBH medium the same strength in state$_i$3 versus state$_i$4 was found before the glucose addition or after additions of lower incremental glucose concentrations (Figure 20 b, page 63). However, after 10 – 20 mM glucose addition, much lower extent of uncoupling due to fatty acid was apparent in state$_i$3, whereas a higher uncoupling, meaning higher respiration acceleration and $\Delta\Psi_m$ decrease, both induced by the fatty acid, was kept state$_i$4. The inability of linoleic acid to further increase respiration stems from the fact that the established hypermetabolic state reached its maximum substrate input which cannot be further increased.

Moreover, we have confirmed that such a mild uncoupling mediated by fatty acid disrupted the glucose-sensing function of INS-1E cells. Correlations between elevated fatty acid levels and disturbed GSIS were previously well characterized [188, 314]. A mild uncoupling caused by fatty acids and integrated over a large period of time (days, months) would thus add to the other more complex mechanisms of lipotoxicity [304, 315].

5.4   4Pi microscopy of pancreatic islet β-cells

Using 4Pi microscopy for the 3D imaging of mitochondrial matrix-addressed RoGFP, we could observe that also *in vivo* cells within the tissue such as pancreatic islet β-cells form strongly interconnected mitochondrial reticulum consisting of mainly a single large mitochondrion or a few (up to five) largely interconnected reticula. Similar pattern was shown previously for INS-1E cells (see [239]). Therefore, it is plausible that the networks frequently observed in cultured cells cannot be an artifact of cell cultivation. An advantage of a continuous mitochondrial network may be seen in the coordinated membrane potential changes throughout the whole reticulum and in an accessibility of the entire network for the transcription and expression products of mitochondrial DNA. Recently, it has also been suggested that mitochondrial networking protects β-cells from nutrient-induced apoptosis [316]. In turn, using the diabetic Goto Kakizaki rats and their remaining β-cells in Langerhans islets as a T2DM model, we could demonstrate that this single mitochondrion tends to become more disintegrated under pathological conditions. These islets usually contain far less insulin-positive β-cells and instead are protruded by fibroblasts and other cell types [276, 277]. Although we have observed here only a single pathogenesis, the generalized principle of morphological diagnostics involving the mitochondrial network may be based upon altered mitochondrial dynamics and morphology under a variety of pathological conditions. This raises the question, why for β-cells of Goto Kakizaki rats their pro-fission mitochondrial dynamics prevails. A possible explanation is that this is the result of previously reported lower mtDNA contents (indicated by the lower 12S rRNA and cyt b mRNA) in islets of adult Goto Kakizaki rats [278]. One might speculate that the increased mitophagy could explain such a lower mtDNA content. Since, it has been suggested that mitochondrial degradation, including mtDNA degradation, proceeds specifically in small objects disintegrated from the main mitochondrial reticulum [317], our current finding of numerous disintegrated small objects in diabetic Goto Kakizaki rats well confirms this view. Also, a significantly smaller mitochondrial volume and an increased number of mitochondria per unit tissue volume have been reported in β-cells of Goto Kakizaki rats [278], which perfectly match our observations.

Goto Kakizaki rats were also reported to possess an impaired glucose-stimulated insulin secretion that originates also from insufficient coupling of mitochondria and insufficient levels of ATP synthesis upon glucose entry into β-cells [276, 277]. This might be an accelerating pathogenic factor playing a role also in the altered (disintegrated) mitochondrial network morphology. Indeed, 4Pi microscopic images for INS-1E cells cultivated at 5 mM glucose [239], i.e. with insufficient autocrine insulin, contain similar features as diabetic β-cells of Goto

Kakizaki rats. These features are represented namely by a more fragmented state (Table 3, page 73).

It must be pointed out that conventional confocal microscopy has been unable to distinguish between patterns of non-diabetic and diabetic mitochondrial networks when used in 2D or 3D mode (Figure 23, page 67). Similarly, even though electron microscopy (EM) routinely achieves a resolution <10 nm, EM has difficulties revealing the extended and connected mitochondrial networks. Classic EM staining procedures disrupt the mitochondrial network. Even with the recent advent of cryo-EM methods for sample preservation, it is a time consuming procedure to assemble a 3D image from a series of electron microscopic or tomographic images which is still prone to artifacts or severely limited in sample thickness. Nevertheless, successful reconstruction of mitochondrial network in Langerhans islet β-cells shows rather disintegrated pattern of such network [318]. The discrepancy between these results and our 4Pi data and conventional confocal microscopic images in numerous reports is not well understood. In spite of this, both EM tomography and conventional EM of β-cells either from INS-1E cells or isolated islets indicated similar mitochondrial tubule diameter (minimum of tubular sections) as determined by 4Pi microscopy. Conventional EM, providing sections of mitochondrial tubules, the well-known solitary kidney-shaped mitochondria images, has already been employed for ultramorphological diagnostics related to T2DM. It has been reported that pancreatic β-cells of human islets isolated from diabetic donors exhibit mitochondria with a higher volume than mitochondria from islets of healthy donors [319]. Additionally, mitochondria of diabetic heart possess thicker mitochondrial reticulum than in control hearts [320].

6   CONCLUSIONS

1. In this work I demonstrate that undecanesulfonate is not an allosteric activator of UCP1. I show that the previously reported undecanesulfonate-dependent activation of UCP1 was based on nonspecific effects independent of UCP1. Therefore, my data are consistent with the fatty acid cycling hypothesis.

2. A competition of palmitic acid, eicosatrienoic acid, and arachidonic acid with spin labeled fatty acid within a putative fatty acid binding site of UCP2 was observed. This finding together with the observation of EPR spectra of highly immobilized probes exclusively in the presence of recombinant UCP2 suggest the existence of a fatty acid binding site on UCP2.

3. Increased ATP/ADP ratio resulting from enhanced glycolysis and oxidative phosphorylation represents a plausible mechanism controlling the glucose-stimulated insulin secretion in pancreatic β-cells. My work showed a simultaneous increase of respiration and electric component of proton motive force $\Delta\Psi_m$ upon glucose addition to glucose depleted INS-1E cells. Endogenous state 3/state 4 respiratory ratio hyperbolically increased with glucose approaching the maximum oxidative phosphorylation rate at maximal GSIS. Presence of fatty acid diminished respiration increase, $\Delta\Psi_m$ jump, and magnitude of insulin release, and reduced state 3/state 4 dependencies on glucose, which was caused by mitochondrial uncoupling.

4. Similarly to INS-1E cells, mitochondria in β-cells within Langerhans islet form a single dense mitochondrion or a few largely interconnected reticula. In contrast to control β-cells, diabetic β-cells from Goto Kakizaki rats exhibited a more disintegrated mitochondrial network. This fact might play role in pathology of type-2 diabetes mellitus and disintegration might stem from the increased mitophagy.

7 REFERENCES

1. Jezek P, Engstova H, Zackova M, Vercesi AE, Costa AD, Arruda P, *et al.* Fatty acid cycling mechanism and mitochondrial uncoupling proteins. *Biochim Biophys Acta* 1998 Jun 10; **1365** (1-2)**:** 319-327.
2. Klingenberg M, Huang SG. Structure and function of the uncoupling protein from brown adipose tissue. *Biochim Biophys Acta* 1999 Jan 8; **1415** (2)**:** 271-296.
3. Hanak P, Jezek P. Mitochondrial uncoupling proteins and phylogenesis--UCP4 as the ancestral uncoupling protein. *FEBS Lett* 2001 Apr 27; **495** (3)**:** 137-141.
4. Jezek P, Urbankova E. Specific sequence of motifs of mitochondrial uncoupling proteins. *IUBMB Life* 2000 Jan; **49** (1)**:** 63-70.
5. Klingenspor M, Fromme T, Hughes DA, Jr., Manzke L, Polymeropoulos E, Riemann T, *et al.* An ancient look at UCP1. *Biochim Biophys Acta* 2008 Jul-Aug; **1777** (7-8)**:** 637-641.
6. Ledesma A, de Lacoba MG, Rial E. The mitochondrial uncoupling proteins. *Genome Biol* 2002; **3** (12)**:** REVIEWS3015.
7. Jezek P, Zackova M, Kosarova J, Rodrigues ET, Madeira VM, Vicente JA. Occurrence of plant-uncoupling mitochondrial protein (PUMP) in diverse organs and tissues of several plants. *J Bioenerg Biomembr* 2000 Dec; **32** (6)**:** 549-561.
8. Krauss S, Zhang CY, Lowell BB. The mitochondrial uncoupling-protein homologues. *Nat Rev Mol Cell Biol* 2005 Mar; **6** (3)**:** 248-261.
9. Ricquier D, Bouillaud F. The uncoupling protein homologues: UCP1, UCP2, UCP3, StUCP and AtUCP. *Biochem J* 2000 Jan 15; **345 Pt 2:** 161-179.
10. Heaton GM, Wagenvoord RJ, Kemp A, Jr., Nicholls DG. Brown-adipose-tissue mitochondria: photoaffinity labelling of the regulatory site of energy dissipation. *Eur J Biochem* 1978 Jan 16; **82** (2)**:** 515-521.
11. Ricquier D, Thibault J, Bouillaud F, Kuster Y. Molecular approach to thermogenesis in brown adipose tissue. Cell-free translation of mRNA and characterization of the mitochondrial uncoupling protein. *J Biol Chem* 1983 Jun 10; **258** (11)**:** 6675-6677.
12. Nicholls DG. Brown adipose tissue mitochondria. *Biochim Biophys Acta* 1979 Jul 3; **549** (1)**:** 1-29.
13. Nicholls DG, Locke RM. Thermogenic mechanisms in brown fat. *Physiol Rev* 1984 Jan; **64** (1)**:** 1-64.
14. Klaus S, Casteilla L, Bouillaud F, Ricquier D. The uncoupling protein UCP: a membraneous mitochondrial ion carrier exclusively expressed in brown adipose tissue. *Int J Biochem* 1991; **23** (9)**:** 791-801.
15. Klingenberg M. Dialectics in carrier research: the ADP/ATP carrier and the uncoupling protein. *J Bioenerg Biomembr* 1993 Oct; **25** (5)**:** 447-457.
16. Ricquier D, Bouillaud F. The mitochondrial uncoupling protein: structural and genetic studies. *Prog Nucleic Acid Res Mol Biol* 1997; **56:** 83-108.
17. Rothwell NJ, Stock MJ. A role for brown adipose tissue in diet-induced thermogenesis. *Nature* 1979 Sep 6; **281** (5726)**:** 31-35.
18. Smith RE, Horwitz BA. Brown fat and thermogenesis. *Physiol Rev* 1969 Apr; **49** (2)**:** 330-425.
19. Shibata H, Perusse F, Bukowiecki LJ. The role of insulin in nonshivering thermogenesis. *Can J Physiol Pharmacol* 1987 Feb; **65** (2)**:** 152-158.
20. Levine JA, Eberhardt NL, Jensen MD. Role of nonexercise activity thermogenesis in resistance to fat gain in humans. *Science* 1999 Jan 8; **283** (5399)**:** 212-214.
21. Carneheim C, Nedergaard J, Cannon B. Beta-adrenergic stimulation of lipoprotein lipase in rat brown adipose tissue during acclimation to cold. *Am J Physiol* 1984 Apr;

246 (4 Pt 1)**:** E327-333.

22. Bouillaud F, Ricquier D, Mory G, Thibault J. Increased level of mRNA for the uncoupling protein in brown adipose tissue of rats during thermogenesis induced by cold exposure or norepinephrine infusion. *J Biol Chem* 1984 Sep 25; **259** (18)**:** 11583-11586.

23. Jacobsson A, Nedergaard J, Cannon B. alpha- and beta-adrenergic control of thermogenin mRNA expression in brown adipose tissue. *Biosci Rep* 1986 Jul; **6** (7)**:** 621-631.

24. Seydoux J, Girardier L. Control of brown fat thermogenesis by the sympathetic nervous system. *Experientia Suppl* 1978; **32:** 153-167.

25. Desautels M, Zaror-Behrens G, Himms-Hagen J. Increased purine nucleotide binding, altered polypeptide composition, and thermogenesis in brown adipose tissue mitochondria of cold-acclimated rats. *Can J Biochem* 1978 Jun; **56** (6)**:** 378-383.

26. Roca P, Rodriguez AM, Oliver P, Bonet ML, Quevedo S, Pico C*, et al.* Brown adipose tissue response to cafeteria diet-feeding involves induction of the UCP2 gene and is impaired in female rats as compared to males. *Pflugers Arch* 1999 Oct; **438** (5)**:** 628-634.

27. Heaton JM. The distribution of brown adipose tissue in the human. *J Anat* 1972 May; **112** (Pt 1)**:** 35-39.

28. Foster DO, Frydman ML. Nonshivering thermogenesis in the rat. II. Measurements of blood flow with microspheres point to brown adipose tissue as the dominant site of the calorigenesis induced by noradrenaline. *Can J Physiol Pharmacol* 1978 Feb; **56** (1)**:** 110-122.

29. Carroll AM, Haines LR, Pearson TW, Fallon PG, Walsh CM, Brennan CM*, et al.* Identification of a functioning mitochondrial uncoupling protein 1 in thymus. *J Biol Chem* 2005 Apr 22; **280** (16)**:** 15534-15543.

30. Adams AE, Carroll AM, Fallon PG, Porter RK. Mitochondrial uncoupling protein 1 expression in thymocytes. *Biochim Biophys Acta* 2008 Jul-Aug; **1777** (7-8)**:** 772-776.

31. Adams AE, Hanrahan O, Nolan DN, Voorheis HP, Fallon P, Porter RK. Images of mitochondrial UCP 1 in mouse thymocytes using confocal microscopy. *Biochim Biophys Acta* 2008 Feb; **1777** (2)**:** 115-117.

32. Frontini A, Rousset S, Cassard-Doulcier AM, Zingaretti C, Ricquier D, Cinti S. Thymus uncoupling protein 1 is exclusive to typical brown adipocytes and is not found in thymocytes. *J Histochem Cytochem* 2007 Feb; **55** (2)**:** 183-189.

33. Carroll AM, Haines LR, Pearson TW, Brennan C, Breen EP, Porter RK. Immunodetection of UCP1 in rat thymocytes. *Biochem Soc Trans* 2004 Dec; **32** (Pt 6)**:** 1066-1067.

34. Mori S, Yoshizuka N, Takizawa M, Takema Y, Murase T, Tokimitsu I*, et al.* Expression of uncoupling proteins in human skin and skin-derived cells. *J Invest Dermatol* 2008 Aug; **128** (8)**:** 1894-1900.

35. Jastroch M, Buckingham JA, Helwig M, Klingenspor M, Brand MD. Functional characterisation of UCP1 in the common carp: uncoupling activity in liver mitochondria and cold-induced expression in the brain. *J Comp Physiol B* 2007 Oct; **177** (7)**:** 743-752.

36. Sale MM, Hsu FC, Palmer ND, Gordon CJ, Keene KL, Borgerink HM*, et al.* The uncoupling protein 1 gene, UCP1, is expressed in mammalian islet cells and associated with acute insulin response to glucose in African American families from the IRAS Family Study. *BMC Endocr Disord* 2007; **7:** 1.

37. Ricquier D, Nechad M, Mory G. Ultrastructural and biochemical characterization of human brown adipose tissue in pheochromocytoma. *J Clin Endocrinol Metab* 1982 Apr; **54** (4)**:** 803-807.

38. Lin CS, Klingenberg M. Characteristics of the isolated purine nucleotide binding protein from brown fat mitochondria. *Biochemistry* 1982 Jun 8; **21** (12)**:** 2950-2956.

39. Jezek P, Garlid KD. Mammalian mitochondrial uncoupling proteins. *Int J Biochem Cell Biol* 1998 Nov; **30** (11)**:** 1163-1168.

40. Klingenberg M. Mechanism and evolution of the uncoupling protein of brown adipose tissue. *Trends Biochem Sci* 1990 Mar; **15** (3)**:** 108-112.

41. el Moualij B, Duyckaerts C, Lamotte-Brasseur J, Sluse FE. Phylogenetic classification of the mitochondrial carrier family of Saccharomyces cerevisiae. *Yeast* 1997 May; **13** (6)**:** 573-581.

42. Jezek P, Garlid KD. New substrates and competitive inhibitors of the Cl- translocating pathway of the uncoupling protein of brown adipose tissue mitochondria. *J Biol Chem* 1990 Nov 5; **265** (31)**:** 19303-19311.

43. Jezek P, Orosz DE, Garlid KD. Reconstitution of the uncoupling protein of brown adipose tissue mitochondria. Demonstration of GDP-sensitive halide anion uniport. *J Biol Chem* 1990 Nov 5; **265** (31)**:** 19296-19302.

44. Jezek P, Borecky J. Mitochondrial uncoupling protein may participate in futile cycling of pyruvate and other monocarboxylates. *Am J Physiol* 1998 Aug; **275** (2 Pt 1)**:** C496-504.

45. Skulachev VP. Fatty acid circuit as a physiological mechanism of uncoupling of oxidative phosphorylation. *FEBS Lett* 1991 Dec 9; **294** (3)**:** 158-162.

46. Garlid KD, Orosz DE, Modriansky M, Vassanelli S, Jezek P. On the mechanism of fatty acid-induced proton transport by mitochondrial uncoupling protein. *J Biol Chem* 1996 Feb 2; **271** (5)**:** 2615-2620.

47. Winkler E, Klingenberg M. Effect of fatty acids on H+ transport activity of the reconstituted uncoupling protein. *J Biol Chem* 1994 Jan 28; **269** (4)**:** 2508-2515.

48. Wojtczak L, Wieckowski MR, Schonfeld P. Protonophoric activity of fatty acid analogs and derivatives in the inner mitochondrial membrane: a further argument for the fatty acid cycling model. *Arch Biochem Biophys* 1998 Sep 1; **357** (1)**:** 76-84.

49. Bernardi P, Penzo D, Wojtczak L. Mitochondrial energy dissipation by fatty acids. Mechanisms and implications for cell death. *Vitam Horm* 2002; **65:** 97-126.

50. Jezek P, Orosz DE, Modriansky M, Garlid KD. Transport of anions and protons by the mitochondrial uncoupling protein and its regulation by nucleotides and fatty acids. A new look at old hypotheses. *J Biol Chem* 1994 Oct 21; **269** (42)**:** 26184-26190.

51. Garlid KD. Opening mitochondrial K(ATP) in the heart--what happens, and what does not happen. *Basic Res Cardiol* 2000 Aug; **95** (4)**:** 275-279.

52. Jaburek M, Varecha M, Gimeno RE, Dembski M, Jezek P, Zhang M*, et al.* Transport function and regulation of mitochondrial uncoupling proteins 2 and 3. *J Biol Chem* 1999 Sep 10; **274** (37)**:** 26003-26007.

53. Urbankova E, Hanak P, Skobisova E, Ruzicka M, Jezek P. Substitutional mutations in the uncoupling protein-specific sequences of mitochondrial uncoupling protein UCP1 lead to the reduction of fatty acid-induced H+ uniport. *Int J Biochem Cell Biol* 2003 Feb; **35** (2)**:** 212-220.

54. Beck V, Jaburek M, Demina T, Rupprecht A, Porter RK, Jezek P*, et al.* Polyunsaturated fatty acids activate human uncoupling proteins 1 and 2 in planar lipid bilayers. *FASEB J* 2007 Apr; **21** (4)**:** 1137-1144.

55. Beck V, Jaburek M, Breen EP, Porter RK, Jezek P, Pohl EE. A new automated technique for the reconstitution of hydrophobic proteins into planar bilayer membranes. Studies of human recombinant uncoupling protein 1. *Biochim Biophys Acta* 2006 May-Jun; **1757** (5-6)**:** 474-479.

56. Nedergaard J, Cannon B. The 'novel' 'uncoupling' proteins UCP2 and UCP3: what do they really do? Pros and cons for suggested functions. *Exp Physiol* 2003 Jan; **88** (1)**:** 65-84.

57. Klingenberg M, Echtay KS. Uncoupling proteins: the issues from a biochemist point of view. *Biochim Biophys Acta* 2001 Mar 1; **1504** (1)**:** 128-143.

58. Nicholls DG, Rial E. Measurement of proton leakage across mitochondrial inner membranes and its relation to protonmotive force. *Methods Enzymol* 1989; **174:** 85-94.

59. Rial E, Aguirregoitia E, Jimenez-Jimenez J, Ledesma A. Alkylsulfonates activate the uncoupling protein UCP1: implications for the transport mechanism. *Biochim Biophys*

Acta 2004 Feb 15; **1608** (2-3)**:** 122-130.

60. Gonzalez-Barroso MM, Fleury C, Bouillaud F, Nicholls DG, Rial E. The uncoupling protein UCP1 does not increase the proton conductance of the inner mitochondrial membrane by functioning as a fatty acid anion transporter. *J Biol Chem* 1998 Jun 19; **273** (25)**:** 15528-15532.

61. Jezek P, Houstek J, Drahota Z. Alkaline pH, membrane potential, and magnesium cations are negative modulators of purine nucleotide inhibition of H+ and Cl- transport through the uncoupling protein of brown adipose tissue mitochondria. *J Bioenerg Biomembr* 1988 Oct; **20** (5)**:** 603-622.

62. Klingenberg M. Nucleotide binding to uncoupling protein. Mechanism of control by protonation. *Biochemistry* 1988 Jan 26; **27** (2)**:** 781-791.

63. Huang SG, Klingenberg M. Fluorescent nucleotide derivatives as specific probes for the uncoupling protein: thermodynamics and kinetics of binding and the control by pH. *Biochemistry* 1995 Jan 10; **34** (1)**:** 349-360.

64. Huang SG, Klingenberg M. Two-stage nucleotide binding mechanism and its implications to H+ transport inhibition of the uncoupling protein from brown adipose tissue mitochondria. *Biochemistry* 1996 Jun 18; **35** (24)**:** 7846-7854.

65. Huang SG, Lin QS, Klingenberg M. Slow-phase kinetics of nucleotide binding to the uncoupling protein from brown adipose tissue mitochondria. *J Biol Chem* 1998 Jan 9; **273** (2)**:** 859-864.

66. Winkler E, Klingenberg M. An improved procedure for reconstitution of the uncoupling protein and in-depth analysis of H+/OH- transport. *Eur J Biochem* 1992 Jul 1; **207** (1)**:** 135-145.

67. Jezek P, Bauer M, Trommer WE. EPR spectroscopy of 5-DOXYL-stearic acid bound to the mitochondrial uncoupling protein reveals its competitive displacement by alkylsulfonates in the channel and allosteric displacement by ATP. *FEBS Lett* 1995 Mar 20; **361** (2-3)**:** 303-307.

68. LaNoue KF, Strzelecki T, Strzelecka D, Koch C. Regulation of the uncoupling protein in brown adipose tissue. *J Biol Chem* 1986 Jan 5; **261** (1)**:** 298-305.

69. Cannon B, Sundin U, Romert L. Palmitoyl coenzyme A: a possible physiological regulator of nucleotide binding to brown adipose tissue mitochondria. *FEBS Lett* 1977 Feb 15; **74** (1)**:** 43-46.

70. Lean ME. Brown adipose tissue in humans. *Proc Nutr Soc* 1989 Jul; **48** (2)**:** 243-256.

71. Himms-Hagen J. Brown adipose tissue thermogenesis and obesity. *Prog Lipid Res* 1989; **28** (2)**:** 67-115.

72. Kozak LP, Britton JH, Kozak UC, Wells JM. The mitochondrial uncoupling protein gene. Correlation of exon structure to transmembrane domains. *J Biol Chem* 1988 Sep 5; **263** (25)**:** 12274-12277.

73. Cassard AM, Bouillaud F, Mattei MG, Hentz E, Raimbault S, Thomas M*, et al.* Human uncoupling protein gene: structure, comparison with rat gene, and assignment to the long arm of chromosome 4. *J Cell Biochem* 1990 Jul; **43** (3)**:** 255-264.

74. Boss O, Samec S, Paoloni-Giacobino A, Rossier C, Dulloo A, Seydoux J*, et al.* Uncoupling protein-3: a new member of the mitochondrial carrier family with tissue-specific expression. *FEBS Lett* 1997 May 12; **408** (1)**:** 39-42.

75. Vidal-Puig A, Solanes G, Grujic D, Flier JS, Lowell BB. UCP3: an uncoupling protein homologue expressed preferentially and abundantly in skeletal muscle and brown adipose tissue. *Biochem Biophys Res Commun* 1997 Jun 9; **235** (1)**:** 79-82.

76. Mao W, Yu XX, Zhong A, Li W, Brush J, Sherwood SW*, et al.* UCP4, a novel brain-specific mitochondrial protein that reduces membrane potential in mammalian cells. *FEBS Lett* 1999 Jan 29; **443** (3)**:** 326-330.

77. Sanchis D, Fleury C, Chomiki N, Goubern M, Huang Q, Neverova M*, et al.* BMCP1, a novel mitochondrial carrier with high expression in the central nervous system of humans and rodents, and respiration uncoupling activity in recombinant yeast. *J Biol Chem* 1998 Dec 18; **273** (51)**:** 34611-34615.

78. Dalgaard LT, Pedersen O. Uncoupling proteins: functional characteristics and role in the pathogenesis of obesity and Type II diabetes. *Diabetologia* 2001 Aug; **44** (8)**:** 946-965.

79. Hoerter J, Gonzalez-Barroso MD, Couplan E, Mateo P, Gelly C, Cassard-Doulcier AM*, et al.* Mitochondrial uncoupling protein 1 expressed in the heart of transgenic mice protects against ischemic-reperfusion damage. *Circulation* 2004 Aug 3; **110** (5)**:** 528-533.

80. Arsenijevic D, Onuma H, Pecqueur C, Raimbault S, Manning BS, Miroux B*, et al.* Disruption of the uncoupling protein-2 gene in mice reveals a role in immunity and reactive oxygen species production. *Nat Genet* 2000 Dec; **26** (4)**:** 435-439.

81. Brand MD, Esteves TC. Physiological functions of the mitochondrial uncoupling proteins UCP2 and UCP3. *Cell Metab* 2005 Aug; **2** (2)**:** 85-93.

82. Casteilla L, Rigoulet M, Penicaud L. Mitochondrial ROS metabolism: modulation by uncoupling proteins. *IUBMB Life* 2001 Sep-Nov; **52** (3-5)**:** 181-188.

83. Echtay KS, Roussel D, St-Pierre J, Jekabsons MB, Cadenas S, Stuart JA*, et al.* Superoxide activates mitochondrial uncoupling proteins. *Nature* 2002 Jan 3; **415** (6867)**:** 96-99.

84. Kowaltowski AJ, Costa AD, Vercesi AE. Activation of the potato plant uncoupling mitochondrial protein inhibits reactive oxygen species generation by the respiratory chain. *FEBS Lett* 1998 Mar 27; **425** (2)**:** 213-216.

85. Pastore D, Fratianni A, Di Pede S, Passarella S. Effects of fatty acids, nucleotides and reactive oxygen species on durum wheat mitochondria. *FEBS Lett* 2000 Mar 17; **470** (1)**:** 88-92.

86. Fleury C, Neverova M, Collins S, Raimbault S, Champigny O, Levi-Meyrueis C*, et al.* Uncoupling protein-2: a novel gene linked to obesity and hyperinsulinemia. *Nat Genet* 1997 Mar; **15** (3)**:** 269-272.

87. Gimeno RE, Dembski M, Weng X, Deng N, Shyjan AW, Gimeno CJ*, et al.* Cloning and characterization of an uncoupling protein homolog: a potential molecular mediator of human thermogenesis. *Diabetes* 1997 May; **46** (5)**:** 900-906.

88. Pecqueur C, Alves-Guerra MC, Gelly C, Levi-Meyrueis C, Couplan E, Collins S*, et al.* Uncoupling protein 2, in vivo distribution, induction upon oxidative stress, and evidence for translational regulation. *J Biol Chem* 2001 Mar 23; **276** (12)**:** 8705-8712.

89. Jaburek M, Miyamoto S, Di Mascio P, Garlid KD, Jezek P. Hydroperoxy fatty acid cycling mediated by mitochondrial uncoupling protein UCP2. *J Biol Chem* 2004 Dec 17; **279** (51)**:** 53097-53102.

90. Brand MD, Affourtit C, Esteves TC, Green K, Lambert AJ, Miwa S*, et al.* Mitochondrial superoxide: production, biological effects, and activation of uncoupling proteins. *Free Radic Biol Med* 2004 Sep 15; **37** (6)**:** 755-767.

91. Jezek P, Hlavata L. Mitochondria in homeostasis of reactive oxygen species in cell, tissues, and organism. *Int J Biochem Cell Biol* 2005 Dec; **37** (12)**:** 2478-2503.

92. Murphy MP, Echtay KS, Blaikie FH, Asin-Cayuela J, Cocheme HM, Green K*, et al.* Superoxide activates uncoupling proteins by generating carbon-centered radicals and initiating lipid peroxidation: studies using a mitochondria-targeted spin trap derived from alpha-phenyl-N-tert-butylnitrone. *J Biol Chem* 2003 Dec 5; **278** (49)**:** 48534-48545.

93. Cannon B, Shabalina IG, Kramarova TV, Petrovic N, Nedergaard J. Uncoupling proteins: a role in protection against reactive oxygen species--or not? *Biochim Biophys Acta* 2006 May-Jun; **1757** (5-6)**:** 449-458.

94. Jezek P, Zackova M, Ruzicka M, Skobisova E, Jaburek M. Mitochondrial uncoupling proteins--facts and fantasies. *Physiol Res* 2004; **53 Suppl 1:** S199-211.

95. Alan L, Smolkova K, Kronusova E, Santorova J, Jezek P. Absolute levels of transcripts for mitochondrial uncoupling proteins UCP2, UCP3, UCP4, and UCP5 show different patterns in rat and mice tissues. *J Bioenerg Biomembr* 2009 Feb; **41** (1)**:** 71-78.

96. Korshunov SS, Skulachev VP, Starkov AA. High protonic potential actuates a

mechanism of production of reactive oxygen species in mitochondria. *FEBS Lett* 1997 Oct 13; **416** (1)**:** 15-18.

97. Korshunov SS, Korkina OV, Ruuge EK, Skulachev VP, Starkov AA. Fatty acids as natural uncouplers preventing generation of O2.- and H2O2 by mitochondria in the resting state. *FEBS Lett* 1998 Sep 18; **435** (2-3)**:** 215-218.

98. Dlaskova A, Hlavata L, Jezek J, Jezek P. Mitochondrial Complex I superoxide production is attenuated by uncoupling. *Int J Biochem Cell Biol* 2008; **40** (10)**:** 2098-2109.

99. Dlaskova A, Hlavata L, Jezek P. Oxidative stress caused by blocking of mitochondrial complex I H(+) pumping as a link in aging/disease vicious cycle. *Int J Biochem Cell Biol* 2008; **40** (9)**:** 1792-1805.

100. Plecita-Hlavata L, Jezek J, Jezek P. Pro-oxidant mitochondrial matrix-targeted ubiquinone MitoQ10 acts as anti-oxidant at retarded electron transport or proton pumping within Complex I. *Int J Biochem Cell Biol* 2009 Aug-Sep; **41** (8-9)**:** 1697-1707.

101. Echtay KS, Esteves TC, Pakay JL, Jekabsons MB, Lambert AJ, Portero-Otin M*, et al.* A signalling role for 4-hydroxy-2-nonenal in regulation of mitochondrial uncoupling. *EMBO J* 2003 Aug 15; **22** (16)**:** 4103-4110.

102. Zackova M, Skobisova E, Urbankova E, Jezek P. Activating omega-6 polyunsaturated fatty acids and inhibitory purine nucleotides are high affinity ligands for novel mitochondrial uncoupling proteins UCP2 and UCP3. *J Biol Chem* 2003 Jun 6; **278** (23)**:** 20761-20769.

103. Jaburek M, Garlid KD. Reconstitution of recombinant uncoupling proteins: UCP1, -2, and -3 have similar affinities for ATP and are unaffected by coenzyme Q10. *J Biol Chem* 2003 Jul 11; **278** (28)**:** 25825-25831.

104. Hagen T, Zhang CY, Vianna CR, Lowell BB. Uncoupling proteins 1 and 3 are regulated differently. *Biochemistry* 2000 May 16; **39** (19)**:** 5845-5851.

105. Fisler JS, Warden CH. Uncoupling proteins, dietary fat and the metabolic syndrome. *Nutr Metab (Lond)* 2006; **3:** 38.

106. Mattiasson G, Sullivan PG. The emerging functions of UCP2 in health, disease, and therapeutics. *Antioxid Redox Signal* 2006 Jan-Feb; **8** (1-2)**:** 1-38.

107. Zhang CY, Baffy G, Perret P, Krauss S, Peroni O, Grujic D*, et al.* Uncoupling protein-2 negatively regulates insulin secretion and is a major link between obesity, beta cell dysfunction, and type 2 diabetes. *Cell* 2001 Jun 15; **105** (6)**:** 745-755.

108. Joseph JW, Koshkin V, Saleh MC, Sivitz WI, Zhang CY, Lowell BB*, et al.* Free fatty acid-induced beta-cell defects are dependent on uncoupling protein 2 expression. *J Biol Chem* 2004 Dec 3; **279** (49)**:** 51049-51056.

109. Trenker M, Malli R, Fertschai I, Levak-Frank S, Graier WF. Uncoupling proteins 2 and 3 are fundamental for mitochondrial Ca2+ uniport. *Nat Cell Biol* 2007 Apr; **9** (4)**:** 445-452.

110. Wu Z, Zhang J, Zhao B. Superoxide anion regulates the mitochondrial free Ca2+ through uncoupling proteins. *Antioxid Redox Signal* 2009 Aug; **11** (8)**:** 1805-1818.

111. Brookes PS, Parker N, Buckingham JA, Vidal-Puig A, Halestrap AP, Gunter TE*, et al.* UCPs--unlikely calcium porters. *Nat Cell Biol* 2008 Nov; **10** (11)**:** 1235-1237; author reply 1237-1240.

112. Rousset S, Emre Y, Join-Lambert O, Hurtaud C, Ricquier D, Cassard-Doulcier AM. The uncoupling protein 2 modulates the cytokine balance in innate immunity. *Cytokine* 2006 Aug; **35** (3-4)**:** 135-142.

113. Arsenijevic D, Garcia I, Vesin C, Vesin D, Arsenijevic Y, Seydoux J*, et al.* Differential roles of tumor necrosis factor-alpha and interferon-gamma in mouse hypermetabolic and anorectic responses induced by LPS. *Eur Cytokine Netw* 2000 Dec; **11** (4)**:** 662-668.

114. Emre Y, Hurtaud C, Nubel T, Criscuolo F, Ricquier D, Cassard-Doulcier AM. Mitochondria contribute to LPS-induced MAPK activation via uncoupling protein UCP2 in macrophages. *Biochem J* 2007 Mar 1; **402** (2)**:** 271-278.

115. Kizaki T, Suzuki K, Hitomi Y, Taniguchi N, Saitoh D, Watanabe K, *et al.* Uncoupling protein 2 plays an important role in nitric oxide production of lipopolysaccharide-stimulated macrophages. *Proc Natl Acad Sci U S A* 2002 Jul 9; **99** (14)**:** 9392-9397.

116. Blanc J, Alves-Guerra MC, Esposito B, Rousset S, Gourdy P, Ricquier D, *et al.* Protective role of uncoupling protein 2 in atherosclerosis. *Circulation* 2003 Jan 28; **107** (3)**:** 388-390.

117. Ryu JW, Hong KH, Maeng JH, Kim JB, Ko J, Park JY, *et al.* Overexpression of uncoupling protein 2 in THP1 monocytes inhibits beta2 integrin-mediated firm adhesion and transendothelial migration. *Arterioscler Thromb Vasc Biol* 2004 May; **24** (5)**:** 864-870.

118. Mattiasson G, Shamloo M, Gido G, Mathi K, Tomasevic G, Yi S, *et al.* Uncoupling protein-2 prevents neuronal death and diminishes brain dysfunction after stroke and brain trauma. *Nat Med* 2003 Aug; **9** (8)**:** 1062-1068.

119. Chan CB, MacDonald PE, Saleh MC, Johns DC, Marban E, Wheeler MB. Overexpression of uncoupling protein 2 inhibits glucose-stimulated insulin secretion from rat islets. *Diabetes* 1999 Jul; **48** (7)**:** 1482-1486.

120. Wang MY, Shimabukuro M, Lee Y, Trinh KY, Chen JL, Newgard CB, *et al.* Adenovirus-mediated overexpression of uncoupling protein-2 in pancreatic islets of Zucker diabetic rats increases oxidative activity and improves beta-cell function. *Diabetes* 1999 May; **48** (5)**:** 1020-1025.

121. Joseph JW, Koshkin V, Zhang CY, Wang J, Lowell BB, Chan CB, *et al.* Uncoupling protein 2 knockout mice have enhanced insulin secretory capacity after a high-fat diet. *Diabetes* 2002 Nov; **51** (11)**:** 3211-3219.

122. De Souza CT, Araujo EP, Stoppiglia LF, Pauli JR, Ropelle E, Rocco SA, *et al.* Inhibition of UCP2 expression reverses diet-induced diabetes mellitus by effects on both insulin secretion and action. *FASEB J* 2007 Apr; **21** (4)**:** 1153-1163.

123. Sesti G, Cardellini M, Marini MA, Frontoni S, D'Adamo M, Del Guerra S, *et al.* A common polymorphism in the promoter of UCP2 contributes to the variation in insulin secretion in glucose-tolerant subjects. *Diabetes* 2003 May; **52** (5)**:** 1280-1283.

124. Sasahara M, Nishi M, Kawashima H, Ueda K, Sakagashira S, Furuta H, *et al.* Uncoupling protein 2 promoter polymorphism -866G/A affects its expression in beta-cells and modulates clinical profiles of Japanese type 2 diabetic patients. *Diabetes* 2004 Feb; **53** (2)**:** 482-485.

125. Reis AF, Dubois-Laforgue D, Bellanne-Chantelot C, Timsit J, Velho G. A polymorphism in the promoter of UCP2 gene modulates lipid levels in patients with type 2 diabetes. *Mol Genet Metab* 2004 Aug; **82** (4)**:** 339-344.

126. D'Adamo M, Perego L, Cardellini M, Marini MA, Frontoni S, Andreozzi F, *et al.* The -866A/A genotype in the promoter of the human uncoupling protein 2 gene is associated with insulin resistance and increased risk of type 2 diabetes. *Diabetes* 2004 Jul; **53** (7)**:** 1905-1910.

127. Krempler F, Esterbauer H, Weitgasser R, Ebenbichler C, Patsch JR, Miller K, *et al.* A functional polymorphism in the promoter of UCP2 enhances obesity risk but reduces type 2 diabetes risk in obese middle-aged humans. *Diabetes* 2002 Nov; **51** (11)**:** 3331-3335.

128. Marti A, Corbalan MS, Forga L, Martinez-Gonzalez MA, Martinez JA. Higher obesity risk associated with the exon-8 insertion of the UCP2 gene in a Spanish case-control study. *Nutrition* 2004 Jun; **20** (6)**:** 498-501.

129. Cho YM, Ritchie MD, Moore JH, Park JY, Lee KU, Shin HD, *et al.* Multifactor-dimensionality reduction shows a two-locus interaction associated with Type 2 diabetes mellitus. *Diabetologia* 2004 Mar; **47** (3)**:** 549-554.

130. Zimmet P, Alberti KG, Shaw J. Global and societal implications of the diabetes epidemic. *Nature* 2001 Dec 13; **414** (6865)**:** 782-787.

131. Kahn CR. Banting Lecture. Insulin action, diabetogenes, and the cause of type II diabetes. *Diabetes* 1994 Aug; **43** (8)**:** 1066-1084.

132. Pick A, Clark J, Kubstrup C, Levisetti M, Pugh W, Bonner-Weir S*, et al.* Role of apoptosis in failure of beta-cell mass compensation for insulin resistance and beta-cell defects in the male Zucker diabetic fatty rat. *Diabetes* 1998 Mar; **47** (3)**:** 358-364.

133. Milburn JL, Jr., Hirose H, Lee YH, Nagasawa Y, Ogawa A, Ohneda M*, et al.* Pancreatic beta-cells in obesity. Evidence for induction of functional, morphologic, and metabolic abnormalities by increased long chain fatty acids. *J Biol Chem* 1995 Jan 20; **270** (3)**:** 1295-1299.

134. Weir GC, Laybutt DR, Kaneto H, Bonner-Weir S, Sharma A. Beta-cell adaptation and decompensation during the progression of diabetes. *Diabetes* 2001 Feb; **50 Suppl 1:** S154-159.

135. Wu L, Nicholson W, Knobel SM, Steffner RJ, May JM, Piston DW*, et al.* Oxidative stress is a mediator of glucose toxicity in insulin-secreting pancreatic islet cell lines. *J Biol Chem* 2004 Mar 26; **279** (13)**:** 12126-12134.

136. Perseghin G, Ghosh S, Gerow K, Shulman GI. Metabolic defects in lean nondiabetic offspring of NIDDM parents: a cross-sectional study. *Diabetes* 1997 Jun; **46** (6)**:** 1001-1009.

137. Bluher M, Kratzsch J, Paschke R. Plasma levels of tumor necrosis factor-alpha, angiotensin II, growth hormone, and IGF-I are not elevated in insulin-resistant obese individuals with impaired glucose tolerance. *Diabetes Care* 2001 Feb; **24** (2)**:** 328-334.

138. Brehm A, Thomaseth K, Bernroider E, Nowotny P, Waldhausl W, Pacini G*, et al.* The role of endocrine counterregulation for estimating insulin sensitivity from intravenous glucose tolerance tests. *J Clin Endocrinol Metab* 2006 Jun; **91** (6)**:** 2272-2278.

139. Moller N, Jorgensen JO. Effects of growth hormone on glucose, lipid, and protein metabolism in human subjects. *Endocr Rev* 2009 Apr; **30** (2)**:** 152-177.

140. Jiang G, Zhang BB. Glucagon and regulation of glucose metabolism. *Am J Physiol Endocrinol Metab* 2003 Apr; **284** (4)**:** E671-678.

141. Cabrera O, Berman DM, Kenyon NS, Ricordi C, Berggren PO, Caicedo A. The unique cytoarchitecture of human pancreatic islets has implications for islet cell function. *Proc Natl Acad Sci U S A* 2006 Feb 14; **103** (7)**:** 2334-2339.

142. Kanno T, Gopel SO, Rorsman P, Wakui M. Cellular function in multicellular system for hormone-secretion: electrophysiological aspect of studies on alpha-, beta- and delta-cells of the pancreatic islet. *Neurosci Res* 2002 Feb; **42** (2)**:** 79-90.

143. Barg S. Mechanisms of exocytosis in insulin-secreting B-cells and glucagon-secreting A-cells. *Pharmacol Toxicol* 2003 Jan; **92** (1)**:** 3-13.

144. Wollheim CB. Beta-cell mitochondria in the regulation of insulin secretion: a new culprit in type II diabetes. *Diabetologia* 2000 Mar; **43** (3)**:** 265-277.

145. Ahren B. Autonomic regulation of islet hormone secretion--implications for health and disease. *Diabetologia* 2000 Apr; **43** (4)**:** 393-410.

146. Sharp GW. Mechanisms of inhibition of insulin release. *Am J Physiol* 1996 Dec; **271** (6 Pt 1)**:** C1781-1799.

147. Bell GI, Polonsky KS. Diabetes mellitus and genetically programmed defects in beta-cell function. *Nature* 2001 Dec 13; **414** (6865)**:** 788-791.

148. Maechler P, Kennedy ED, Pozzan T, Wollheim CB. Mitochondrial activation directly triggers the exocytosis of insulin in permeabilized pancreatic beta-cells. *EMBO J* 1997 Jul 1; **16** (13)**:** 3833-3841.

149. Wollheim CB, Maechler P. Beta-cell mitochondria and insulin secretion: messenger role of nucleotides and metabolites. *Diabetes* 2002 Feb; **51 Suppl 1:** S37-42.

150. Thorens B, Deriaz N, Bosco D, DeVos A, Pipeleers D, Schuit F*, et al.* Protein kinase A-dependent phosphorylation of GLUT2 in pancreatic beta cells. *J Biol Chem* 1996 Apr 5; **271** (14)**:** 8075-8081.

151. Scheepers A, Joost HG, Schurmann A. The glucose transporter families SGLT and GLUT: molecular basis of normal and aberrant function. *JPEN J Parenter Enteral Nutr* 2004 Sep-Oct; **28** (5)**:** 364-371.

152. Newgard CB, McGarry JD. Metabolic coupling factors in pancreatic beta-cell signal

transduction. *Annu Rev Biochem* 1995; **64:** 689-719.

153. Matschinsky FM. Banting Lecture 1995. A lesson in metabolic regulation inspired by the glucokinase glucose sensor paradigm. *Diabetes* 1996 Feb; **45** (2)**:** 223-241.

154. MacDonald MJ. High content of mitochondrial glycerol-3-phosphate dehydrogenase in pancreatic islets and its inhibition by diazoxide. *J Biol Chem* 1981 Aug 25; **256** (16)**:** 8287-8290.

155. Eto K, Tsubamoto Y, Terauchi Y, Sugiyama T, Kishimoto T, Takahashi N*, et al.* Role of NADH shuttle system in glucose-induced activation of mitochondrial metabolism and insulin secretion. *Science* 1999 Feb 12; **283** (5404)**:** 981-985.

156. Schuit F, De Vos A, Farfari S, Moens K, Pipeleers D, Brun T*, et al.* Metabolic fate of glucose in purified islet cells. Glucose-regulated anaplerosis in beta cells. *J Biol Chem* 1997 Jul 25; **272** (30)**:** 18572-18579.

157. Sekine N, Cirulli V, Regazzi R, Brown LJ, Gine E, Tamarit-Rodriguez J*, et al.* Low lactate dehydrogenase and high mitochondrial glycerol phosphate dehydrogenase in pancreatic beta-cells. Potential role in nutrient sensing. *J Biol Chem* 1994 Feb 18; **269** (7)**:** 4895-4902.

158. Ishihara H, Wang H, Drewes LR, Wollheim CB. Overexpression of monocarboxylate transporter and lactate dehydrogenase alters insulin secretory responses to pyruvate and lactate in beta cells. *J Clin Invest* 1999 Dec; **104** (11)**:** 1621-1629.

159. Zhao C, Wilson MC, Schuit F, Halestrap AP, Rutter GA. Expression and distribution of lactate/monocarboxylate transporter isoforms in pancreatic islets and the exocrine pancreas. *Diabetes* 2001 Feb; **50** (2)**:** 361-366.

160. Maechler P, Carobbio S, Rubi B. In beta-cells, mitochondria integrate and generate metabolic signals controlling insulin secretion. *Int J Biochem Cell Biol* 2006; **38** (5-6)**:** 696-709.

161. Ashcroft SJ. The beta-cell K(ATP) channel. *J Membr Biol* 2000 Aug 1; **176** (3)**:** 187-206.

162. Rutter GA. Nutrient-secretion coupling in the pancreatic islet beta-cell: recent advances. *Mol Aspects Med* 2001 Dec; **22** (6)**:** 247-284.

163. Cook DL, Hales CN. Intracellular ATP directly blocks K+ channels in pancreatic B-cells. *Nature* 1984 Sep 20-26; **311** (5983)**:** 271-273.

164. Rorsman P, Trube G. Glucose dependent K+-channels in pancreatic beta-cells are regulated by intracellular ATP. *Pflugers Arch* 1985 Dec; **405** (4)**:** 305-309.

165. Erecinska M, Bryla J, Michalik M, Meglasson MD, Nelson D. Energy metabolism in islets of Langerhans. *Biochim Biophys Acta* 1992 Aug 7; **1101** (3)**:** 273-295.

166. Ronner P, Naumann CM, Friel E. Effects of glucose and amino acids on free ADP in betaHC9 insulin-secreting cells. *Diabetes* 2001 Feb; **50** (2)**:** 291-300.

167. Ainscow EK, Rutter GA. Glucose-stimulated oscillations in free cytosolic ATP concentration imaged in single islet beta-cells: evidence for a Ca2+-dependent mechanism. *Diabetes* 2002 Feb; **51 Suppl 1:** S162-170.

168. Ainscow EK, Rutter GA. Mitochondrial priming modifies Ca2+ oscillations and insulin secretion in pancreatic islets. *Biochem J* 2001 Jan 15; **353** (Pt 2)**:** 175-180.

169. Ghosh A, Ronner P, Cheong E, Khalid P, Matschinsky FM. The role of ATP and free ADP in metabolic coupling during fuel-stimulated insulin release from islet beta-cells in the isolated perfused rat pancreas. *J Biol Chem* 1991 Dec 5; **266** (34)**:** 22887-22892.

170. Fridlyand LE, Ma L, Philipson LH. Adenine nucleotide regulation in pancreatic beta-cells: modeling of ATP/ADP-Ca2+ interactions. *Am J Physiol Endocrinol Metab* 2005 Nov; **289** (5)**:** E839-848.

171. Ashcroft SJ, Ashcroft FM. Properties and functions of ATP-sensitive K-channels. *Cell Signal* 1990; **2** (3)**:** 197-214.

172. Straub SG, Sharp GW. Glucose-stimulated signaling pathways in biphasic insulin secretion. *Diabetes Metab Res Rev* 2002 Nov-Dec; **18** (6)**:** 451-463.

173. Joseph JW, Jensen MV, Ilkayeva O, Palmieri F, Alarcon C, Rhodes CJ*, et al.* The mitochondrial citrate/isocitrate carrier plays a regulatory role in glucose-stimulated

insulin secretion. *J Biol Chem* 2006 Nov 24; **281** (47)**:** 35624-35632.

174. Wiederkehr A, Park KS, Dupont O, Demaurex N, Pozzan T, Cline GW*, et al.* Matrix alkalinization: a novel mitochondrial signal for sustained pancreatic beta-cell activation. *EMBO J* 2009 Feb 18; **28** (4)**:** 417-428.

175. Hoy M, Maechler P, Efanov AM, Wollheim CB, Berggren PO, Gromada J. Increase in cellular glutamate levels stimulates exocytosis in pancreatic beta-cells. *FEBS Lett* 2002 Nov 6; **531** (2)**:** 199-203.

176. Kibbey RG, Pongratz RL, Romanelli AJ, Wollheim CB, Cline GW, Shulman GI. Mitochondrial GTP regulates glucose-stimulated insulin secretion. *Cell Metab* 2007 Apr; **5** (4)**:** 253-264.

177. Zhou YP, Grill VE. Long-term exposure of rat pancreatic islets to fatty acids inhibits glucose-induced insulin secretion and biosynthesis through a glucose fatty acid cycle. *J Clin Invest* 1994 Feb; **93** (2)**:** 870-876.

178. Cnop M, Hannaert JC, Hoorens A, Eizirik DL, Pipeleers DG. Inverse relationship between cytotoxicity of free fatty acids in pancreatic islet cells and cellular triglyceride accumulation. *Diabetes* 2001 Aug; **50** (8)**:** 1771-1777.

179. Lupi R, Dotta F, Marselli L, Del Guerra S, Masini M, Santangelo C*, et al.* Prolonged exposure to free fatty acids has cytostatic and pro-apoptotic effects on human pancreatic islets: evidence that beta-cell death is caspase mediated, partially dependent on ceramide pathway, and Bcl-2 regulated. *Diabetes* 2002 May; **51** (5)**:** 1437-1442.

180. Unger RH. The physiology of cellular liporegulation. *Annu Rev Physiol* 2003; **65:** 333-347.

181. Harmon JS, Gleason CE, Tanaka Y, Poitout V, Robertson RP. Antecedent hyperglycemia, not hyperlipidemia, is associated with increased islet triacylglycerol content and decreased insulin gene mRNA level in Zucker diabetic fatty rats. *Diabetes* 2001 Nov; **50** (11)**:** 2481-2486.

182. Briaud I, Kelpe CL, Johnson LM, Tran PO, Poitout V. Differential effects of hyperlipidemia on insulin secretion in islets of langerhans from hyperglycemic versus normoglycemic rats. *Diabetes* 2002 Mar; **51** (3)**:** 662-668.

183. Poitout V, Amyot J, Semache M, Zarrouki B, Hagman D, Fontes G. Glucolipotoxicity of the pancreatic beta cell. *Biochim Biophys Acta* Mar; **1801** (3)**:** 289-298.

184. Sako Y, Grill VE. A 48-hour lipid infusion in the rat time-dependently inhibits glucose-induced insulin secretion and B cell oxidation through a process likely coupled to fatty acid oxidation. *Endocrinology* 1990 Oct; **127** (4)**:** 1580-1589.

185. Stein DT, Stevenson BE, Chester MW, Basit M, Daniels MB, Turley SD*, et al.* The insulinotropic potency of fatty acids is influenced profoundly by their chain length and degree of saturation. *J Clin Invest* 1997 Jul 15; **100** (2)**:** 398-403.

186. Henquin JC. Triggering and amplifying pathways of regulation of insulin secretion by glucose. *Diabetes* 2000 Nov; **49** (11)**:** 1751-1760.

187. Lameloise N, Muzzin P, Prentki M, Assimacopoulos-Jeannet F. Uncoupling protein 2: a possible link between fatty acid excess and impaired glucose-induced insulin secretion? *Diabetes* 2001 Apr; **50** (4)**:** 803-809.

188. Carlsson C, Borg LA, Welsh N. Sodium palmitate induces partial mitochondrial uncoupling and reactive oxygen species in rat pancreatic islets in vitro. *Endocrinology* 1999 Aug; **140** (8)**:** 3422-3428.

189. Poitout V, Hagman D, Stein R, Artner I, Robertson RP, Harmon JS. Regulation of the insulin gene by glucose and fatty acids. *J Nutr* 2006 Apr; **136** (4)**:** 873-876.

190. McGarry JD, Brown NF. The mitochondrial carnitine palmitoyltransferase system. From concept to molecular analysis. *Eur J Biochem* 1997 Feb 15; **244** (1)**:** 1-14.

191. Nolan CJ, Madiraju MS, Delghingaro-Augusto V, Peyot ML, Prentki M. Fatty acid signaling in the beta-cell and insulin secretion. *Diabetes* 2006 Dec; **55 Suppl 2:** S16-23.

192. Tushuizen ME, Bunck MC, Pouwels PJ, Bontemps S, van Waesberghe JH, Schindhelm RK*, et al.* Pancreatic fat content and beta-cell function in men with and without type 2 diabetes. *Diabetes Care* 2007 Nov; **30** (11)**:** 2916-2921.

193. Larsson O, Deeney JT, Branstrom R, Berggren PO, Corkey BE. Activation of the ATP-sensitive K+ channel by long chain acyl-CoA. A role in modulation of pancreatic beta-cell glucose sensitivity. *J Biol Chem* 1996 May 3; **271** (18)**:** 10623-10626.

194. Kliewer SA, Forman BM, Blumberg B, Ong ES, Borgmeyer U, Mangelsdorf DJ, *et al.* Differential expression and activation of a family of murine peroxisome proliferator-activated receptors. *Proc Natl Acad Sci U S A* 1994 Jul 19; **91** (15)**:** 7355-7359.

195. Ito E, Ozawa S, Takahashi K, Tanaka T, Katsuta H, Yamaguchi S, *et al.* PPAR-gamma overexpression selectively suppresses insulin secretory capacity in isolated pancreatic islets through induction of UCP-2 protein. *Biochem Biophys Res Commun* 2004 Nov 12; **324** (2)**:** 810-814.

196. Tordjman K, Standley KN, Bernal-Mizrachi C, Leone TC, Coleman T, Kelly DP, *et al.* PPARalpha suppresses insulin secretion and induces UCP2 in insulinoma cells. *J Lipid Res* 2002 Jun; **43** (6)**:** 936-943.

197. Zhou YT, Shimabukuro M, Wang MY, Lee Y, Higa M, Milburn JL, *et al.* Role of peroxisome proliferator-activated receptor alpha in disease of pancreatic beta cells. *Proc Natl Acad Sci U S A* 1998 Jul 21; **95** (15)**:** 8898-8903.

198. Patane G, Anello M, Piro S, Vigneri R, Purrello F, Rabuazzo AM. Role of ATP production and uncoupling protein-2 in the insulin secretory defect induced by chronic exposure to high glucose or free fatty acids and effects of peroxisome proliferator-activated receptor-gamma inhibition. *Diabetes* 2002 Sep; **51** (9)**:** 2749-2756.

199. Medvedev AV, Robidoux J, Bai X, Cao W, Floering LM, Daniel KW, *et al.* Regulation of the uncoupling protein-2 gene in INS-1 beta-cells by oleic acid. *J Biol Chem* 2002 Nov 8; **277** (45)**:** 42639-42644.

200. Medvedev AV, Snedden SK, Raimbault S, Ricquier D, Collins S. Transcriptional regulation of the mouse uncoupling protein-2 gene. Double E-box motif is required for peroxisome proliferator-activated receptor-gamma-dependent activation. *J Biol Chem* 2001 Apr 6; **276** (14)**:** 10817-10823.

201. Ghiselli A, Laurenti O, De Mattia G, Maiani G, Ferro-Luzzi A. Salicylate hydroxylation as an early marker of in vivo oxidative stress in diabetic patients. *Free Radic Biol Med* 1992 Dec; **13** (6)**:** 621-626.

202. Gopaul NK, Anggard EE, Mallet AI, Betteridge DJ, Wolff SP, Nourooz-Zadeh J. Plasma 8-epi-PGF2 alpha levels are elevated in individuals with non-insulin dependent diabetes mellitus. *FEBS Lett* 1995 Jul 17; **368** (2)**:** 225-229.

203. Rehman A, Nourooz-Zadeh J, Moller W, Tritschler H, Pereira P, Halliwell B. Increased oxidative damage to all DNA bases in patients with type II diabetes mellitus. *FEBS Lett* 1999 Apr 1; **448** (1)**:** 120-122.

204. Shin CS, Moon BS, Park KS, Kim SY, Park SJ, Chung MH, *et al.* Serum 8-hydroxy-guanine levels are increased in diabetic patients. *Diabetes Care* 2001 Apr; **24** (4)**:** 733-737.

205. Sakuraba H, Mizukami H, Yagihashi N, Wada R, Hanyu C, Yagihashi S. Reduced beta-cell mass and expression of oxidative stress-related DNA damage in the islet of Japanese Type II diabetic patients. *Diabetologia* 2002 Jan; **45** (1)**:** 85-96.

206. Murakami K, Kondo T, Ohtsuka Y, Fujiwara Y, Shimada M, Kawakami Y. Impairment of glutathione metabolism in erythrocytes from patients with diabetes mellitus. *Metabolism* 1989 Aug; **38** (8)**:** 753-758.

207. Paolisso G, Giugliano D, Pizza G, Gambardella A, Tesauro P, Varricchio M, *et al.* Glutathione infusion potentiates glucose-induced insulin secretion in aged patients with impaired glucose tolerance. *Diabetes Care* 1992 Jan; **15** (1)**:** 1-7.

208. Baynes JW. Role of oxidative stress in development of complications in diabetes. *Diabetes* 1991 Apr; **40** (4)**:** 405-412.

209. Nishikawa T, Edelstein D, Du XL, Yamagishi S, Matsumura T, Kaneda Y, *et al.* Normalizing mitochondrial superoxide production blocks three pathways of hyperglycaemic damage. *Nature* 2000 Apr 13; **404** (6779)**:** 787-790.

210. Hunt JV, Dean RT, Wolff SP. Hydroxyl radical production and autoxidative

glycosylation. Glucose autoxidation as the cause of protein damage in the experimental glycation model of diabetes mellitus and ageing. *Biochem J* 1988 Nov 15; **256** (1)**:** 205-212.

211. Oliveira HR, Verlengia R, Carvalho CR, Britto LR, Curi R, Carpinelli AR. Pancreatic beta-cells express phagocyte-like NAD(P)H oxidase. *Diabetes* 2003 Jun; **52** (6)**:** 1457-1463.

212. Grankvist K, Marklund SL, Taljedal IB. CuZn-superoxide dismutase, Mn-superoxide dismutase, catalase and glutathione peroxidase in pancreatic islets and other tissues in the mouse. *Biochem J* 1981 Nov 1; **199** (2)**:** 393-398.

213. Tiedge M, Lortz S, Munday R, Lenzen S. Complementary action of antioxidant enzymes in the protection of bioengineered insulin-producing RINm5F cells against the toxicity of reactive oxygen species. *Diabetes* 1998 Oct; **47** (10)**:** 1578-1585.

214. Gurgul E, Lortz S, Tiedge M, Jorns A, Lenzen S. Mitochondrial catalase overexpression protects insulin-producing cells against toxicity of reactive oxygen species and proinflammatory cytokines. *Diabetes* 2004 Sep; **53** (9)**:** 2271-2280.

215. Tiedge M, Lortz S, Drinkgern J, Lenzen S. Relation between antioxidant enzyme gene expression and antioxidative defense status of insulin-producing cells. *Diabetes* 1997 Nov; **46** (11)**:** 1733-1742.

216. Archer SL, Wu XC, Thebaud B, Moudgil R, Hashimoto K, Michelakis ED. O2 sensing in the human ductus arteriosus: redox-sensitive K+ channels are regulated by mitochondria-derived hydrogen peroxide. *Biol Chem* 2004 Mar-Apr; **385** (3-4)**:** 205-216.

217. Kraft R, Grimm C, Grosse K, Hoffmann A, Sauerbruch S, Kettenmann H*, et al.* Hydrogen peroxide and ADP-ribose induce TRPM2-mediated calcium influx and cation currents in microglia. *Am J Physiol Cell Physiol* 2004 Jan; **286** (1)**:** C129-137.

218. Krauss S, Zhang CY, Scorrano L, Dalgaard LT, St-Pierre J, Grey ST*, et al.* Superoxide-mediated activation of uncoupling protein 2 causes pancreatic beta cell dysfunction. *J Clin Invest* 2003 Dec; **112** (12)**:** 1831-1842.

219. Duchen MR. Mitochondria in health and disease: perspectives on a new mitochondrial biology. *Mol Aspects Med* 2004 Aug; **25** (4)**:** 365-451.

220. Galluzzi L, Maiuri MC, Vitale I, Zischka H, Castedo M, Zitvogel L*, et al.* Cell death modalities: classification and pathophysiological implications. *Cell Death Differ* 2007 Jul; **14** (7)**:** 1237-1243.

221. Ballinger SW. Mitochondrial dysfunction in cardiovascular disease. *Free Radic Biol Med* 2005 May 15; **38** (10)**:** 1278-1295.

222. Lin MT, Beal MF. Mitochondrial dysfunction and oxidative stress in neurodegenerative diseases. *Nature* 2006 Oct 19; **443** (7113)**:** 787-795.

223. Alirol E, Martinou JC. Mitochondria and cancer: is there a morphological connection? *Oncogene* 2006 Aug 7; **25** (34)**:** 4706-4716.

224. Maiese K, Chong ZZ, Shang YC. Mechanistic insights into diabetes mellitus and oxidative stress. *Curr Med Chem* 2007; **14** (16)**:** 1729-1738.

225. Muller FL, Lustgarten MS, Jang Y, Richardson A, Van Remmen H. Trends in oxidative aging theories. *Free Radic Biol Med* 2007 Aug 15; **43** (4)**:** 477-503.

226. Hackenbrock CR. Ultrastructural bases for metabolically linked mechanical activity in mitochondria. I. Reversible ultrastructural changes with change in metabolic steady state in isolated liver mitochondria. *J Cell Biol* 1966 Aug; **30** (2)**:** 269-297.

227. Mannella CA. Structure and dynamics of the mitochondrial inner membrane cristae. *Biochim Biophys Acta* 2006 May-Jun; **1763** (5-6)**:** 542-548.

228. Knott AB, Perkins G, Schwarzenbacher R, Bossy-Wetzel E. Mitochondrial fragmentation in neurodegeneration. *Nat Rev Neurosci* 2008 Jul; **9** (7)**:** 505-518.

229. Szabadkai G, Simoni AM, Bianchi K, De Stefani D, Leo S, Wieckowski MR*, et al.* Mitochondrial dynamics and Ca2+ signaling. *Biochim Biophys Acta* 2006 May-Jun; **1763** (5-6)**:** 442-449.

230. Youle RJ, Karbowski M. Mitochondrial fission in apoptosis. *Nat Rev Mol Cell Biol*

2005 Aug; **6** (8)**:** 657-663.

231. Hoppins S, Lackner L, Nunnari J. The machines that divide and fuse mitochondria. *Annu Rev Biochem* 2007; **76:** 751-780.

232. Rossignol R, Gilkerson R, Aggeler R, Yamagata K, Remington SJ, Capaldi RA. Energy substrate modulates mitochondrial structure and oxidative capacity in cancer cells. *Cancer Res* 2004 Feb 1; **64** (3)**:** 985-993.

233. Benard G, Bellance N, James D, Parrone P, Fernandez H, Letellier T*, et al.* Mitochondrial bioenergetics and structural network organization. *J Cell Sci* 2007 Mar 1; **120** (Pt 5)**:** 838-848.

234. Koopman WJ, Verkaart S, Visch HJ, van der Westhuizen FH, Murphy MP, van den Heuvel LW*, et al.* Inhibition of complex I of the electron transport chain causes O2-. - mediated mitochondrial outgrowth. *Am J Physiol Cell Physiol* 2005 Jun; **288** (6)**:** C1440-1450.

235. Yu T, Robotham JL, Yoon Y. Increased production of reactive oxygen species in hyperglycemic conditions requires dynamic change of mitochondrial morphology. *Proc Natl Acad Sci U S A* 2006 Feb 21; **103** (8)**:** 2653-2658.

236. Detmer SA, Chan DC. Functions and dysfunctions of mitochondrial dynamics. *Nat Rev Mol Cell Biol* 2007 Nov; **8** (11)**:** 870-879.

237. Egner A, Jakobs S, Hell SW. Fast 100-nm resolution three-dimensional microscope reveals structural plasticity of mitochondria in live yeast. *Proc Natl Acad Sci U S A* 2002 Mar 19; **99** (6)**:** 3370-3375.

238. Medda R, Jakobs S, Hell SW, Bewersdorf J. 4Pi microscopy of quantum dot-labeled cellular structures. *J Struct Biol* 2006 Dec; **156** (3)**:** 517-523.

239. Plecita-Hlavata L, Lessard M, Santorova J, Bewersdorf J, Jezek P. Mitochondrial oxidative phosphorylation and energetic status are reflected by morphology of mitochondrial network in INS-1E and HEP-G2 cells viewed by 4Pi microscopy. *Biochim Biophys Acta* 2008 Jul-Aug; **1777** (7-8)**:** 834-846.

240. Barsoum MJ, Yuan H, Gerencser AA, Liot G, Kushnareva Y, Graber S*, et al.* Nitric oxide-induced mitochondrial fission is regulated by dynamin-related GTPases in neurons. *EMBO J* 2006 Aug 23; **25** (16)**:** 3900-3911.

241. De Vos KJ, Allan VJ, Grierson AJ, Sheetz MP. Mitochondrial function and actin regulate dynamin-related protein 1-dependent mitochondrial fission. *Curr Biol* 2005 Apr 12; **15** (7)**:** 678-683.

242. Ishihara N, Fujita Y, Oka T, Mihara K. Regulation of mitochondrial morphology through proteolytic cleavage of OPA1. *EMBO J* 2006 Jul 12; **25** (13)**:** 2966-2977.

243. Malka F, Guillery O, Cifuentes-Diaz C, Guillou E, Belenguer P, Lombes A*, et al.* Separate fusion of outer and inner mitochondrial membranes. *EMBO Rep* 2005 Sep; **6** (9)**:** 853-859.

244. Lyamzaev KG, Izyumov DS, Avetisyan AV, Yang F, Pletjushkina OY, Chernyak BV. Inhibition of mitochondrial bioenergetics: the effects on structure of mitochondria in the cell and on apoptosis. *Acta Biochim Pol* 2004; **51** (2)**:** 553-562.

245. Pletjushkina OY, Lyamzaev KG, Popova EN, Nepryakhina OK, Ivanova OY, Domnina LV*, et al.* Effect of oxidative stress on dynamics of mitochondrial reticulum. *Biochim Biophys Acta* 2006 May-Jun; **1757** (5-6)**:** 518-524.

246. Aronis A, Melendez JA, Golan O, Shilo S, Dicter N, Tirosh O. Potentiation of Fas-mediated apoptosis by attenuated production of mitochondria-derived reactive oxygen species. *Cell Death Differ* 2003 Mar; **10** (3)**:** 335-344.

247. Dispersyn G, Nuydens R, Connors R, Borgers M, Geerts H. Bcl-2 protects against FCCP-induced apoptosis and mitochondrial membrane potential depolarization in PC12 cells. *Biochim Biophys Acta* 1999 Aug 5; **1428** (2-3)**:** 357-371.

248. Kuruvilla S, Qualls CW, Jr., Tyler RD, Witherspoon SM, Benavides GR, Yoon LW*, et al.* Effects of minimally toxic levels of carbonyl cyanide P-(trifluoromethoxy) phenylhydrazone (FCCP), elucidated through differential gene expression with biochemical and morphological correlations. *Toxicol Sci* 2003 Jun; **73** (2)**:** 348-361.

249. Desquiret V, Loiseau D, Jacques C, Douay O, Malthiery Y, Ritz P, *et al.* Dinitrophenol-induced mitochondrial uncoupling in vivo triggers respiratory adaptation in HepG2 cells. *Biochim Biophys Acta* 2006 Jan; **1757** (1)**:** 21-30.

250. Bahlmann K, Jakobs S, Hell SW. 4Pi-confocal microscopy of live cells. *Ultramicroscopy* 2001 Apr; **87** (3)**:** 155-164.

251. Lang MC, Engelhardt J, Hell SW. 4Pi microscopy with linear fluorescence excitation. *Opt Lett* 2007 Feb 1; **32** (3)**:** 259-261.

252. Jakobs S. High resolution imaging of live mitochondria. *Biochim Biophys Acta* 2006 May-Jun; **1763** (5-6)**:** 561-575.

253. Gugel H, Bewersdorf J, Jakobs S, Engelhardt J, Storz R, Hell SW. Cooperative 4Pi excitation and detection yields sevenfold sharper optical sections in live-cell microscopy. *Biophys J* 2004 Dec; **87** (6)**:** 4146-4152.

254. Hell SW, Wichmann J. Breaking the diffraction resolution limit by stimulated emission: stimulated-emission-depletion fluorescence microscopy. *Opt Lett* 1994 Jun 1; **19** (11)**:** 780-782.

255. Hell SW. Far-field optical nanoscopy. *Science* 2007 May 25; **316** (5828)**:** 1153-1158.

256. Hein B, Willig KI, Hell SW. Stimulated emission depletion (STED) nanoscopy of a fluorescent protein-labeled organelle inside a living cell. *Proc Natl Acad Sci U S A* 2008 Sep 23; **105** (38)**:** 14271-14276.

257. Schmidt R, Wurm CA, Jakobs S, Engelhardt J, Egner A, Hell SW. Spherical nanosized focal spot unravels the interior of cells. *Nat Methods* 2008 Jun; **5** (6)**:** 539-544.

258. Schmidt R, Wurm CA, Punge A, Egner A, Jakobs S, Hell SW. Mitochondrial cristae revealed with focused light. *Nano Lett* 2009 Jun; **9** (6)**:** 2508-2510.

259. Hess ST, Girirajan TP, Mason MD. Ultra-high resolution imaging by fluorescence photoactivation localization microscopy. *Biophys J* 2006 Dec 1; **91** (11)**:** 4258-4272.

260. Betzig E, Patterson GH, Sougrat R, Lindwasser OW, Olenych S, Bonifacino JS, *et al.* Imaging intracellular fluorescent proteins at nanometer resolution. *Science* 2006 Sep 15; **313** (5793)**:** 1642-1645.

261. Rust MJ, Bates M, Zhuang X. Sub-diffraction-limit imaging by stochastic optical reconstruction microscopy (STORM). *Nat Methods* 2006 Oct; **3** (10)**:** 793-795.

262. Shroff H, Galbraith CG, Galbraith JA, White H, Gillette J, Olenych S, *et al.* Dual-color superresolution imaging of genetically expressed probes within individual adhesion complexes. *Proc Natl Acad Sci U S A* 2007 Dec 18; **104** (51)**:** 20308-20313.

263. Fernandez-Suarez M, Ting AY. Fluorescent probes for super-resolution imaging in living cells. *Nat Rev Mol Cell Biol* 2008 Dec; **9** (12)**:** 929-943.

264. Huang B, Wang W, Bates M, Zhuang X. Three-dimensional super-resolution imaging by stochastic optical reconstruction microscopy. *Science* 2008 Feb 8; **319** (5864)**:** 810-813.

265. Juette MF, Gould TJ, Lessard MD, Mlodzianoski MJ, Nagpure BS, Bennett BT, *et al.* Three-dimensional sub-100 nm resolution fluorescence microscopy of thick samples. *Nat Methods* 2008 Jun; **5** (6)**:** 527-529.

266. Pavani SR, Thompson MA, Biteen JS, Lord SJ, Liu N, Twieg RJ, *et al.* Three-dimensional, single-molecule fluorescence imaging beyond the diffraction limit by using a double-helix point spread function. *Proc Natl Acad Sci U S A* 2009 Mar 3; **106** (9)**:** 2995-2999.

267. Campfield LA, Smith FJ, Guisez Y, Devos R, Burn P. Recombinant mouse OB protein: evidence for a peripheral signal linking adiposity and central neural networks. *Science* 1995 Jul 28; **269** (5223)**:** 546-549.

268. Halaas JL, Gajiwala KS, Maffei M, Cohen SL, Chait BT, Rabinowitz D, *et al.* Weight-reducing effects of the plasma protein encoded by the obese gene. *Science* 1995 Jul 28; **269** (5223)**:** 543-546.

269. Pelleymounter MA, Cullen MJ, Baker MB, Hecht R, Winters D, Boone T, *et al.* Effects of the obese gene product on body weight regulation in ob/ob mice. *Science* 1995 Jul 28; **269** (5223)**:** 540-543.

270. Phillips MS, Liu Q, Hammond HA, Dugan V, Hey PJ, Caskey CJ, *et al.* Leptin receptor missense mutation in the fatty Zucker rat. *Nat Genet* 1996 May; **13** (1)**:** 18-19.

271. Iida M, Murakami T, Ishida K, Mizuno A, Kuwajima M, Shima K. Substitution at codon 269 (glutamine --> proline) of the leptin receptor (OB-R) cDNA is the only mutation found in the Zucker fatty (fa/fa) rat. *Biochem Biophys Res Commun* 1996 Jul 16; **224** (2)**:** 597-604.

272. Lee Y, Hirose H, Zhou YT, Esser V, McGarry JD, Unger RH. Increased lipogenic capacity of the islets of obese rats: a role in the pathogenesis of NIDDM. *Diabetes* 1997 Mar; **46** (3)**:** 408-413.

273. Suzuki K, Yen-Chung H, Toyota T, Goto Y, Hirata Y, Okada K. The significance of nerve sugar levels for the peripheral nerve impairment of spontaneously diabetic GK (Goto-Kakizaki) rats. *Diabetes Res* 1990 May; **14** (1)**:** 21-25.

274. Yagihashi S, Goto Y, Kakizaki M, Kaseda N. Thickening of glomerular basement membrane in spontaneously diabetic rats. *Diabetologia* 1978 Oct; **15** (4)**:** 309-312.

275. Phillips AO, Baboolal K, Riley S, Grone H, Janssen U, Steadman R, *et al.* Association of prolonged hyperglycemia with glomerular hypertrophy and renal basement membrane thickening in the Goto Kakizaki model of non-insulin-dependent diabetes mellitus. *Am J Kidney Dis* 2001 Feb; **37** (2)**:** 400-410.

276. Ostenson CG, Efendic S. Islet gene expression and function in type 2 diabetes; studies in the Goto-Kakizaki rat and humans. *Diabetes Obes Metab* 2007 Nov; **9 Suppl 2:** 180-186.

277. Mizukami H, Wada R, Koyama M, Takeo T, Suga S, Wakui M, *et al.* Augmented beta cell loss and mitochondrial abnormalities in sucrose-fed GK rats. *Virchows Arch* 2008 Apr; **452** (4)**:** 383-392.

278. Serradas P, Giroix MH, Saulnier C, Gangnerau MN, Borg LA, Welsh M, *et al.* Mitochondrial deoxyribonucleic acid content is specifically decreased in adult, but not fetal, pancreatic islets of the Goto-Kakizaki rat, a genetic model of noninsulin-dependent diabetes. *Endocrinology* 1995 Dec; **136** (12)**:** 5623-5631.

279. Shen W, Hao J, Tian C, Ren J, Yang L, Li X, *et al.* A combination of nutriments improves mitochondrial biogenesis and function in skeletal muscle of type 2 diabetic Goto-Kakizaki rats. *PLoS One* 2008; **3** (6)**:** e2328.

280. Cannon B, Lindberg O. Mitochondria from brown adipose tissue: isolation and properties. *Methods Enzymol* 1979; **55:** 65-78.

281. LaNoue KF, Koch CD, Meditz RB. Mechanism of action of norepinephrine in hamster brown adipocytes. *J Biol Chem* 1982 Nov 25; **257** (22)**:** 13740-13748.

282. Lowry OH, Rosebrough NJ, Farr AL, Randall RJ. Protein measurement with the Folin phenol reagent. *J Biol Chem* 1951 Nov; **193** (1)**:** 265-275.

283. Merglen A, Theander S, Rubi B, Chaffard G, Wollheim CB, Maechler P. Glucose sensitivity and metabolism-secretion coupling studied during two-year continuous culture in INS-1E insulinoma cells. *Endocrinology* 2004 Feb; **145** (2)**:** 667-678.

284. Saudek F, Cihalova E, Karasova L, Kobylka P, Lomsky R. Increased glucagon-stimulated insulin secretion of cryopreserved rat islets transplanted into nude mice. *J Mol Med* 1999 Jan; **77** (1)**:** 107-110.

285. Cossarizza A, Ceccarelli D, Masini A. Functional heterogeneity of an isolated mitochondrial population revealed by cytofluorometric analysis at the single organelle level. *Exp Cell Res* 1996 Jan 10; **222** (1)**:** 84-94.

286. Nicholls DG, Lindberg O. Brown-adipose-tissue mitochondria. The influence of albumin and nucleotides on passive ion permeabilities. *Eur J Biochem* 1973 Sep 3; **37** (3)**:** 523-530.

287. Nedergaard J, Cannon B. Sulfonates are low-affinity ligands for the GDP-binding site of brown-fat mitochondria. *Biochim Biophys Acta* 1994 May 18; **1185** (3)**:** 311-317.

288. Civelek VN, Deeney JT, Kubik K, Schultz V, Tornheim K, Corkey BE. Temporal sequence of metabolic and ionic events in glucose-stimulated clonal pancreatic beta-cells (HIT). *Biochem J* 1996 May 1; **315 (Pt 3):** 1015-1019.

289. Jaburek M, Varecha M, Jezek P, Garlid KD. Alkylsulfonates as probes of uncoupling protein transport mechanism. Ion pair transport demonstrates that direct H(+) translocation by UCP1 is not necessary for uncoupling. *J Biol Chem* 2001 Aug 24; **276** (34)**:** 31897-31905.

290. Garlid KD, Jaburek M, Jezek P. The mechanism of proton transport mediated by mitochondrial uncoupling proteins. *FEBS Lett* 1998 Oct 30; **438** (1-2)**:** 10-14.

291. Garlid KD, Jaburek M, Jezek P, Varecha M. How do uncoupling proteins uncouple? *Biochim Biophys Acta* 2000 Aug 15; **1459** (2-3)**:** 383-389.

292. Jezek P, Freisleben HJ. Fatty acid binding site of the mitochondrial uncoupling protein. Demonstration of its existence by EPR spectroscopy of 5-DOXYL-stearic acid. *FEBS Lett* 1994 Apr 18; **343** (1)**:** 22-26.

293. Urbankova E, Voltchenko A, Pohl P, Jezek P, Pohl EE. Transport kinetics of uncoupling proteins. Analysis of UCP1 reconstituted in planar lipid bilayers. *J Biol Chem* 2003 Aug 29; **278** (35)**:** 32497-32500.

294. Shabalina IG, Jacobsson A, Cannon B, Nedergaard J. Native UCP1 displays simple competitive kinetics between the regulators purine nucleotides and fatty acids. *J Biol Chem* 2004 Sep 10; **279** (37)**:** 38236-38248.

295. Cannon B, Nedergaard J. Brown adipose tissue: function and physiological significance. *Physiol Rev* 2004 Jan; **84** (1)**:** 277-359.

296. Jakobs P, Braun A, Jezek P, Trommer WE. Binding of ATP to uncoupling protein of brown fat mitochondria as studied by means of spin-labeled ATP derivatives. *FEBS Lett* 1991 Jun 24; **284** (2)**:** 195-198.

297. Reboiras MD, Marsh D. EPR studies on the influence of chain length on the segmental motion of spin-labeled fatty acids in dimyristoylphosphatidylcholine bilayers. *Biochim Biophys Acta* 1991 Apr 2; **1063** (2)**:** 259-264.

298. Jezek P, Jezek J. Sequence anatomy of mitochondrial anion carriers. *FEBS Lett* 2003 Jan 16; **534** (1-3)**:** 15-25.

299. Pebay-Peyroula E, Dahout-Gonzalez C, Kahn R, Trezeguet V, Lauquin GJ, Brandolin G. Structure of mitochondrial ADP/ATP carrier in complex with carboxyatractyloside. *Nature* 2003 Nov 6; **426** (6962)**:** 39-44.

300. Virtanen I, Banerjee M, Palgi J, Korsgren O, Lukinius A, Thornell LE*, et al.* Blood vessels of human islets of Langerhans are surrounded by a double basement membrane. *Diabetologia* 2008 Jul; **51** (7)**:** 1181-1191.

301. Bonner-Weir S. Morphological evidence for pancreatic polarity of beta-cell within islets of Langerhans. *Diabetes* 1988 May; **37** (5)**:** 616-621.

302. Bennett BD, Jetton TL, Ying G, Magnuson MA, Piston DW. Quantitative subcellular imaging of glucose metabolism within intact pancreatic islets. *J Biol Chem* 1996 Feb 16; **271** (7)**:** 3647-3651.

303. Armann B, Hanson MS, Hatch E, Steffen A, Fernandez LA. Quantification of basal and stimulated ROS levels as predictors of islet potency and function. *Am J Transplant* 2007 Jan; **7** (1)**:** 38-47.

304. Qatanani M, Lazar MA. Mechanisms of obesity-associated insulin resistance: many choices on the menu. *Genes Dev* 2007 Jun 15; **21** (12)**:** 1443-1455.

305. Heart E, Corkey RF, Wikstrom JD, Shirihai OS, Corkey BE. Glucose-dependent increase in mitochondrial membrane potential, but not cytoplasmic calcium, correlates with insulin secretion in single islet cells. *Am J Physiol Endocrinol Metab* 2006 Jan; **290** (1)**:** E143-E148.

306. Segall L, Lameloise N, Assimacopoulos-Jeannet F, Roche E, Corkey P, Thumelin S*, et al.* Lipid rather than glucose metabolism is implicated in altered insulin secretion caused by oleate in INS-1 cells. *Am J Physiol* 1999 Sep; **277** (3 Pt 1)**:** E521-528.

307. Wiederkehr A, Wollheim CB. Minireview: implication of mitochondria in insulin secretion and action. *Endocrinology* 2006 Jun; **147** (6)**:** 2643-2649.

308. Deeney JT, Kohler M, Kubik K, Brown G, Schultz V, Tornheim K*, et al.* Glucose-induced metabolic oscillations parallel those of Ca(2+) and insulin release in clonal

insulin-secreting cells. A multiwell approach to oscillatory cell behavior. *J Biol Chem* 2001 Oct 5; **276** (40)**:** 36946-36950.

309.   Yaney GC, Schultz V, Cunningham BA, Dunaway GA, Corkey BE, Tornheim K. Phosphofructokinase isozymes in pancreatic islets and clonal beta-cells (INS-1). *Diabetes* 1995 Nov; **44** (11)**:** 1285-1289.

310.   Nilsson T, Schultz V, Berggren PO, Corkey BE, Tornheim K. Temporal patterns of changes in ATP/ADP ratio, glucose 6-phosphate and cytoplasmic free Ca2+ in glucose-stimulated pancreatic beta-cells. *Biochem J* 1996 Feb 15; **314 (Pt 1):** 91-94.

311.   Jung SK, Gorski W, Aspinwall CA, Kauri LM, Kennedy RT. Oxygen microsensor and its application to single cells and mouse pancreatic islets. *Anal Chem* 1999 Sep 1; **71** (17)**:** 3642-3649.

312.   Bergstrom RW, Fujimoto WY, Teller DC, de Haen C. Oscillatory insulin secretion in perifused isolated rat islets. *Am J Physiol* 1989 Oct; **257** (4 Pt 1)**:** E479-485.

313.   Porterfield DM, Corkey RF, Sanger RH, Tornheim K, Smith PJ, Corkey BE. Oxygen consumption oscillates in single clonal pancreatic beta-cells (HIT). *Diabetes* 2000 Sep; **49** (9)**:** 1511-1516.

314.   Koshkin V, Wang X, Scherer PE, Chan CB, Wheeler MB. Mitochondrial functional state in clonal pancreatic beta-cells exposed to free fatty acids. *J Biol Chem* 2003 May 30; **278** (22)**:** 19709-19715.

315.   Wajchenberg BL. beta-cell failure in diabetes and preservation by clinical treatment. *Endocr Rev* 2007 Apr; **28** (2)**:** 187-218.

316.   Molina AJ, Wikstrom JD, Stiles L, Las G, Mohamed H, Elorza A*, et al.* Mitochondrial networking protects beta-cells from nutrient-induced apoptosis. *Diabetes* 2009 Oct; **58** (10)**:** 2303-2315.

317.   Twig G, Elorza A, Molina AJ, Mohamed H, Wikstrom JD, Walzer G*, et al.* Fission and selective fusion govern mitochondrial segregation and elimination by autophagy. *EMBO J* 2008 Jan 23; **27** (2)**:** 433-446.

318.   Noske AB, Costin AJ, Morgan GP, Marsh BJ. Expedited approaches to whole cell electron tomography and organelle mark-up in situ in high-pressure frozen pancreatic islets. *J Struct Biol* 2008 Mar; **161** (3)**:** 298-313.

319.   Anello M, Lupi R, Spampinato D, Piro S, Masini M, Boggi U*, et al.* Functional and morphological alterations of mitochondria in pancreatic beta cells from type 2 diabetic patients. *Diabetologia* 2005 Feb; **48** (2)**:** 282-289.

320.   Shen X, Zheng S, Thongboonkerd V, Xu M, Pierce WM, Jr., Klein JB*, et al.* Cardiac mitochondrial damage and biogenesis in a chronic model of type 1 diabetes. *Am J Physiol Endocrinol Metab* 2004 Nov; **287** (5)**:** E896-905.